University of California

Los Angeles

NMR study of triangular lattice antiferromagnet $Ba_3CoSb_2O_9$

A dissertation for the degree Doctor of Philosophy in Physics

By

Tong Zhou

University of California, Los Angeles

Department of Physics & Astronomy

2014

ABSTRACT OF THE DISSERTATION

NMR study of triangular lattice antiferromagnet Ba3CoSb2O9

By

Tong Zhou

University of California, Los Angeles, 2014

Professor Stuart Brown, Chair

Triangular lattice antiferromagnet has been an intensely studied topic in condensed matter physics for decades, and there are a sea of relevant theory papers, researching every detail of the triangular lattice system with antiferromagnetic interaction. In contrast, the experimental work has been largely limited by the difficulty in synthesizing high quality materials with triangular lattice. The $Ba_3CoSb_2O_9$ compound thus has its own significance because it possesses a spin-1/2 triangular plane that is almost isotropic, which makes it a good research subject to experimentally verify many theoretical predictions. The fact that this compound has a saturation field of roughly 30T makes it possible for the exploration of the whole H-T phase diagram. The magnetization measurements on this compound revealed the existence of an up-up-down phase, which is of primary interest for the study of triangular lattice

antiferromagnet, and the thermodynamics data sketched the H-T phase diagrams for both B//ab and B//c directions. However, these measurements were based on bulk properties and are not enough to determine the details of spin configuration. The nuclear magnetic resonance (NMR) experiment has the advantage as a local probe technique, and it can help discover the spin orientation by detecting the interaction of nuclear spins with nearby electron spins.

Our NMR experiment was conducted in UCLA for low field (<12T) measurements and in NHMFL for high field (13T<B<31T). We started with the paramagnetic state measurements to sort out different NMR lines, decide the orientation of the sample, and measure the basic NMR parameters. Then we took NMR spectra in the magnetic state under various external fields for both directions. The analysis of the field dependence spectra were combine with the theoretical predictions to check the consistency, and thus we can decide the correct phases in the magnetic state, as well as the field evolution of the spin configurations. The spin lattice relaxation rate measurements were used to decide the phase boundary, and help to reproduce the phase diagram by the thermodynamics measurements.

The dissertation of Tong Zhou is approved.

Richard Kaner

Yaroslav Tserkovnyak

Stuart Brown, Committee Chair

University of California, Los Angeles

2014

Table of Contents

List of Figures

Curriculum Vitae

Name of the Author: Tong Zhou

Education

PhD candidate, Physics, UCLA	**Anticipated December 2014**
MS, Physics, University of California, Los Angeles	**January 2012**
BS, Physics, Zhejiang University,	**June 2009**

Chapter One

Introduction of the Heisenberg Model and the triangular lattice antiferromagnet

The Heisenberg Model for a spin system can be described by the Hamiltonian

$$\mathrm{H} = -\frac{1}{2}\sum_{ij} J_{ij}\boldsymbol{S_i}\cdot\boldsymbol{S_j}$$

In this equation, J_{ij} is the exchange energy between two spins, and $J_{ij} = J_{ji}$ is symmetric. The 1/2 corrects double counting. $\boldsymbol{S_i}$ and $\boldsymbol{S_i}$ are the spin operators.

1.1 The ferromagnetic ground state

If any J_{ij} is non-negative ($J_{ij} \geq 0$), then the ground state happens when all the spins are aligned to the same direction, which we define as the z-direction. The proof is shown below.

We first define the total spin operator $\mathbf{S} = \sum_{\boldsymbol{i}} \boldsymbol{S_i}$, and similarly $S^z = \sum_i S_i^z$. Then we realize S is compatible with H, because

$$[S^z, \mathrm{H}] = \left[S^z, -\frac{1}{2}\sum_{ij} J_{ij}\boldsymbol{S_i}\cdot\boldsymbol{S_j}\right] = \left[S^z, -\frac{1}{2}\sum_{ij} J_{ij}(S_i^x S_j^x + S_i^y S_j^y + S_i^z S_j^z)\right]$$

$$= -\frac{1}{2}\sum_{ijk} J_{ij}\left[S_k^z, S_i^x S_j^x + S_i^y S_j^y + S_i^z S_j^z\right]$$

$$= -\frac{1}{2}\sum_{ijk} J_{ij}\big(S_i^x\left[S_k^z, S_j^x\right] + [S_k^z, S_i^x]S_j^x + S_i^y\left[S_k^z, S_j^y\right] + \left[S_k^z, S_i^y\right]S_j^y$$

$$+ 0\big)$$

$$= -\frac{1}{2}\sum_{ijk} J_{ij}\big(S_i^x\delta_{kj}iS_j^y + \delta_{ki}iS_i^y S_j^x + S_i^y\delta_{kj}(-i)S_j^x$$

$$+ \delta_{ki}(-i)S_i^x S_j^y\big) = 0$$

Similarly, we can prove $[S^x, \mathrm{H}] = 0, and\ [S^y, \mathrm{H}] = 0$, so S is indeed compatible with H, and we can find the simultaneous eigenstates of H, S^2, and S_z.

We can denote the state with all spins aligned with z-direction as $\psi = |\mathrm{S}, \mathrm{S}\rangle_1 |\mathrm{S}, \mathrm{S}\rangle_2 \ldots |\mathrm{S}, \mathrm{S}\rangle_N$. Here since all spins are taking their maximum z-components, the eigenvalues for all S_i^z $(i = 1,2, \ldots N)$ are just S, which is the total spin.

To show that ψ is an eigenstates of H, we first rewrite H as

$$\mathrm{H} = -\frac{1}{2}\sum_{ij} J_{ij}\boldsymbol{S_i}\cdot\boldsymbol{S_j} = -\frac{1}{2}\sum_{ij} J_{ij}\left(S_i^x S_j^x + S_i^y S_j^y + S_i^z S_j^z\right)$$

$$= -\frac{1}{2}\sum_{ij} J_{ij}\left(\frac{S_i^+ + S_i^-}{2}\,\frac{S_j^+ + S_j^-}{2i} + \frac{S_i^+ - S_i^-}{2i}\,\frac{S_j^+ - S_j^-}{2} + S_i^z S_j^z\right)$$

$$= -\frac{1}{2}\sum_{ij} J_{ij}\left(\frac{S_i^+ S_j^- + S_i^- S_j^+}{2} + S_i^z S_j^z\right)$$

Then $\mathrm{H}|\psi\rangle = -\frac{1}{2}\sum_{ij} J_{ij}\left(\frac{1}{2}S_i^+ S_j^-|\psi\rangle + \frac{1}{2}S_i^- S_j^+|\psi\rangle + S_i^z S_j^z|\psi\rangle\right).|\psi\rangle$ is the

fully polarized state so it cannot be further increased. Thus $S_i^+ S_j^- |\psi\rangle = S_i^- S_j^+ |\psi\rangle = 0$, and $S_i^z S_j^z |\psi\rangle = S^2 |\psi\rangle$. $H|\psi\rangle = -\frac{1}{2} S^2 \sum_{ij} J_{ij} |\psi\rangle$, and the expectation value is $-\frac{1}{2} S^2 \sum_{ij} J_{ij}$

Now let us consider an arbitrary state $|\varphi\rangle = |S, m_1\rangle |S, m_2\rangle \ldots |S, m_N\rangle$, which is generally not an eigenstates of H. The expectation value is straightforward to calculate, $\langle\varphi|H|\varphi\rangle = -\frac{1}{2}\sum_{ij} J_{ij} \left(\frac{1}{2} \langle\varphi| S_i^+ S_j^- |\varphi\rangle + \frac{1}{2} \langle\varphi| S_i^- S_j^+ |\varphi\rangle + \langle\varphi| S_i^z S_j^z |\varphi\rangle \right) = -\frac{1}{2}\sum_{ij} J_{ij} \left(0 + 0 + m_i m_j\right) = -\frac{1}{2}\sum_{ij} J_{ij}\, m_i m_j$

If all $J_{ij} \geq 0$, then for any I, j, we have $J_{ij} S^2 \geq J_{ij} m_i m_j$, and therefore $-\frac{1}{2} S^2 \sum_{ij} J_{ij} \leq -\frac{1}{2}\sum_{ij} J_{ij}\, m_i m_j$. Note that $|\varphi\rangle$ is arbitrary, which means the fully polarized state $|\psi\rangle$ has the lowest energy level and is the ground state of the so-called fully ferromagnetic Heisenberg model.

1.2 Heisenberg Antiferromagnetic Model and Marshall's Theorem

In the Hamiltonian $H = -\frac{1}{2}\sum_{ij} J_{ij} \boldsymbol{S_i} \cdot \boldsymbol{S_j}$, if some J_{ij} are negative, then the argument in the previous section does not stand correct and the ferromagnetic state is generally not the ground state. Practically the rigorous solution of the ground state cannot be obtained

In the context of magnetism study, one sensible and important simplification of the Heisenberg Model is the biparticle system. In bipartite systems, all sites can be divided into two disjoint subsets A and B, so that $J_{ij} = 0 \; if \; i,j \in A \; or \; i,j \in B$. So the interaction only exists between particles from different subsets.

An important example of biparticle systems is a square lattice with only nearest neighbor interaction. Fig 1 shows how a two-dimensional square lattice looks when it only has nearest neighbor interactions.

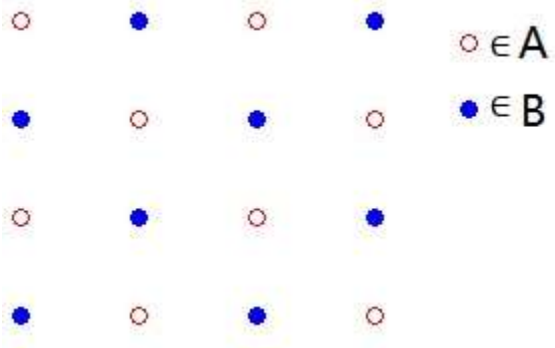

Figure 1 Two dimension square lattice with only nearest neighbor interaction.

In 1948, Louis Néel first proposed the antiferromagnetic state, or the Néel State [2], in which neighboring spins in a system have opposite orientations. In terms of our biparticle system shown in Fig.1, spins in Subset A are aligned and point to the same direction, whereas spins in Subset B are also aligned but point oppositely to the spins in Subset A. Furthermore, if we assume spins in both subsets are fully polarized, that seems to a reasonable guess of the ground state. We can write it as

$$|\psi\rangle = \prod_{i\in A} |S, S\rangle_i \prod_{j\in B} |S, -S\rangle_j$$

Then we have

$$H|\psi\rangle = -\frac{1}{2}\sum_{ij} J_{ij}\left(\frac{1}{2}S_i^+ S_j^- |\psi\rangle + \frac{1}{2}S_i^- S_j^+ |\psi\rangle + S_i^z S_j^z |\psi\rangle\right)$$

$|\psi\rangle$ is an eigenstates of $S_i^z S_j^z$, and the first term is zero, because spins in Subset A cannot be increased and spins in Subset B cannot be decreased. However, $|\psi\rangle$ is not an eigenstates of the second term, so it cannot be an eigenstates of H, and certainly not the ground state.

Relevant to the Heisenberg antiferromagnetic model on a biparticle system, there is a rigorous statement known as Marshall's Theorem: for the Heisenberg model on a bipartite lattice with sublattices of equal size and $J_{ij} \leq 0$ for all $i \in A$ and $j \in B$ or $i \in B$ and $j \in A$ and every pair of sites i, j is connected by a string of bonds with $J_{kl} \neq 0$, the ground state $|\psi_0\rangle$ is non-degenerate and is a singlet of total spin: $\mathbf{S}|\psi_0\rangle = 0$, where $\mathbf{S} = \sum_i \boldsymbol{S_i}$

We should notice that with Marshall's Theorem, the ground state is not uniquely defined because there could be many total-spin singlet states. There are also no preferred orientation of the spin system, so we cannot find any magnetic ordering just from Marshall's Theorem.

It is not a trivial job to find the exact ground state solution of the Heisenberg

Antiferromagnetic Model. In reality, the first rigorous solution was the contribution of Hans Bethe, who formulated the famous “Bethe ansats” in 1931 [1] to approach the one-dimensional Heisenberg model with spin-1/2. In a 1-D model, the spins form a chain and each spin can only take either up or down direction. In 1971, Rodney Baxter worked out the exact solution to the 1D XYZ model. However, this solution is extremely complex, and it indicates even more complex approach to the 2D and 3D cases. Up to now, no one has successfully solved exactly the Heisenberg antiferromagnetic model in higher than one dimension system.

1.3 The classical limit and long range antiferromagnetic ordering

We have seen that the ground state of quantum Heisenberg model is only easy to solve when all $J_{ij} \geq 0$. When this is not true, it is difficult to get a rigorous solution. Even if we consider the Heisenberg Antiferromagnetic Model in the context of biparticle system, we cannot identify a Néel state or other kinds of antiferromagnetic ordering from it.

Experimentally, the antiferromagnetic long range ordering has been discovered first by neutron scattering measurements. To explain this antiferromagnetic state, one important method is to solve the Heisenberg Antiferromagnetic Model for the ground state by a classical approximation. In the classical approximation, we

replace the spin operator $\boldsymbol{S_i}$ by real three-component vectors with the magnitude $|\boldsymbol{S_i}| = S$, and the Hamiltonian can be written as:

$$\mathrm{H} = -\frac{1}{2}\sum_{ij} J_{ij}\boldsymbol{S_i}\cdot\boldsymbol{S_j}$$

The classical approximation works better when the spin S is large and when the dimensionality is higher. For example, it works better for three dimension than 2 dimension.

Now we can try to minimize H under the condition $|\boldsymbol{S_i}| = S$. We will consider the model on a Bravais lattice $\{\boldsymbol{R_i}\}$ and assume J_{ij} is only a function of the separation $|\boldsymbol{R_i} - \boldsymbol{R_j}|$, so $J_{ij} = J_{ji} = J\left(\left|\boldsymbol{R_i} - \boldsymbol{R_j}\right|\right) = J(\Delta R)$. Since the spins are just real vectors, we can define the Fourier transform

$$\boldsymbol{S_q} = \frac{\boldsymbol{1}}{\sqrt{\boldsymbol{N}}}\sum_{\boldsymbol{i}} \boldsymbol{e^{-iq\cdot R_i}}\boldsymbol{S_i}$$

$$\boldsymbol{S_i} = \frac{\boldsymbol{1}}{\sqrt{\boldsymbol{N}}}\sum_{\boldsymbol{q}} \boldsymbol{e^{iq\cdot R_i}}\boldsymbol{S_q}$$

where N is the number of sites, and the sum on q run through the first Brillouin zone. Inserting this into H, we have

$$\mathrm{H} = -\frac{1}{2N}\sum_{qq'}\sum_{ij} J(\Delta R)\boldsymbol{e^{iq\cdot R_i}e^{iq'\cdot R_j}}\boldsymbol{S_q}\cdot\boldsymbol{S_{q'}}$$

$$= -\frac{1}{2N}\sum_{qq'}\sum_{\Delta R} J(\Delta R)\sum_{R_i} e^{i(\boldsymbol{q}+\boldsymbol{q'})\cdot\boldsymbol{R_i}}e^{\boldsymbol{iq\cdot\Delta R}}\,\boldsymbol{S_q}\cdot\boldsymbol{S_{q'}}$$

We notice that $\sum_{R_i} e^{i(\boldsymbol{q}+\boldsymbol{q'})\cdot\boldsymbol{R_i}}$ is actually the Fourier transform of a δ-function

$$\sum_{R_i} e^{i(\boldsymbol{q}+\boldsymbol{q'})\cdot\boldsymbol{R_i}} = N\delta_{\boldsymbol{q}+\boldsymbol{q'},\boldsymbol{0}}$$

Plugging this in we get

$$\mathrm{H} = -\frac{1}{2}\sum_{q}\sum_{\Delta R} e^{-iq\cdot\Delta R} J(\Delta R)\boldsymbol{S_q}\cdot\boldsymbol{S_{-q}} = -\frac{1}{2}\sum_{q} J(q)\boldsymbol{S_q}\cdot\boldsymbol{S_{-q}}$$

where we have defined $J(q) = \sum_{\Delta R} e^{-iq\cdot\Delta R} J(\Delta R)$. To minimize H, there should be a wavevector Q that $J(Q)$ has to assume a global maximum. We expect that when H is minimized, $S_Q \neq 0 \; and \; S_{-Q} \neq 0$, but for all other $\mathrm{q} \neq \pm\mathrm{Q}, S_q = 0$.

If Q=0, then $\boldsymbol{S_i} = \frac{\mathbf{1}}{\sqrt{N}}\sum_{\boldsymbol{q}} \boldsymbol{e^{iq\cdot R_i}}\boldsymbol{S_q} = \frac{\mathbf{1}}{\sqrt{N}}\boldsymbol{S_Q}$ for all the spins, and we actually obtain a homogeneous spin polarization, the ferromagnet.

If $\mathrm{Q} \neq 0$, we can consider the normalization on $\boldsymbol{S_i}$:

$$S^2 = \boldsymbol{S_i}\cdot\boldsymbol{S_i} = \frac{1}{N}\sum_{qq'} e^{i(\boldsymbol{q}+\boldsymbol{q'})\cdot\boldsymbol{R_i}}\boldsymbol{S_q}\cdot\boldsymbol{S_{q'}}$$

$$= \frac{1}{N}(2\boldsymbol{S_Q}\cdot\boldsymbol{S_{-Q}} + e^{2i\boldsymbol{Q}\cdot\boldsymbol{R_i}}\boldsymbol{S_Q}\cdot\boldsymbol{S_Q} + e^{-2i\boldsymbol{Q}\cdot\boldsymbol{R_i}}\boldsymbol{S_{-Q}}\cdot\boldsymbol{S_{-Q}})$$

Recall that we are minimizing H under the condition $|\boldsymbol{S_i}| = S$, so the right-hand must be independent of $\boldsymbol{R_i}$. The last two terms then have to be zero. We thus obtain $\boldsymbol{S_Q}\cdot\boldsymbol{S_Q} = \boldsymbol{S_{-Q}}\cdot\boldsymbol{S_{-Q}} = 0$. $\boldsymbol{S_Q}$ is generally complex since it is a Fourier transform, and since $\boldsymbol{S_i}$ is real, we have $\boldsymbol{S_{-Q}} = \boldsymbol{S_Q^*}$.

Let's assume $\boldsymbol{S_Q} = \boldsymbol{R_Q} + i\boldsymbol{I_Q}$, where $\boldsymbol{R_Q}$ and $\boldsymbol{I_Q}$ are real vectors. Then $\boldsymbol{S_{-Q}} = \boldsymbol{S_Q^*} = \boldsymbol{R_Q} - i\boldsymbol{I_Q}$, and $\boldsymbol{S_Q}\cdot\boldsymbol{S_{-Q}} = R_Q^2 + I_Q^2$. We also have $\boldsymbol{S_Q}\cdot\boldsymbol{S_Q} = R_Q^2 - I_Q^2 + 2i\boldsymbol{R_Q}\cdot\boldsymbol{I_Q} = 0$, which gives us two equations:

$$R_Q^2 = I_Q^2$$

$$\boldsymbol{R_Q} \cdot \boldsymbol{I_Q} = 0$$

We can also explicitly write the magnitude of spin as $S^2 = \frac{1}{N} 2\boldsymbol{S_Q} \cdot \boldsymbol{S_{-Q}} = \frac{\boldsymbol{2}}{\boldsymbol{N}}(R_Q^2 + I_Q^2)$, and thus calculate $R_Q^2 = I_Q^2 = \frac{NS^2}{4}$

The ground state energy is

$$H_0 = -\frac{1}{2}J(Q)\boldsymbol{S_Q} \cdot \boldsymbol{S_{-Q}} - \frac{1}{2}J(-Q)\boldsymbol{S_{-Q}} \cdot \boldsymbol{S_Q} = -J(Q)\left(R_Q^2 + I_Q^2\right) = -J(Q)\frac{NS^2}{2}$$

To figure out the magnetic ordering, we reverse the Fourier transform and obtain

$$\begin{aligned}\boldsymbol{S_i} &= \frac{1}{\sqrt{N}}\left(\boldsymbol{e^{iQ\cdot R_i}}\boldsymbol{S_Q} + \boldsymbol{e^{-iQ\cdot R_i}}\boldsymbol{S_{-Q}}\right) \\ &= \frac{1}{\sqrt{N}}\left[\boldsymbol{e^{iQ\cdot R_i}}\left(\boldsymbol{R_Q} + i\boldsymbol{I_Q}\right) + \boldsymbol{e^{-iQ\cdot R_i}}\left(\boldsymbol{R_Q} - i\boldsymbol{I_Q}\right)\right] \\ &= \frac{2}{\sqrt{N}}(\boldsymbol{R_Q}\cos(\boldsymbol{Q}\cdot\boldsymbol{R_i}) - \boldsymbol{I_Q}\sin(\boldsymbol{Q}\cdot\boldsymbol{R_i}))\end{aligned}$$

We can define the unit vectors $\widehat{\boldsymbol{R}} = \frac{\boldsymbol{R_Q}}{|\boldsymbol{R_Q}|}, and\ \widehat{\boldsymbol{I}} = \frac{\boldsymbol{I_Q}}{|\boldsymbol{I_Q}|}$, and rewrite

$$S_i = S(\widehat{\boldsymbol{R}}\cos(\boldsymbol{Q}\cdot\boldsymbol{R_i}) - \widehat{\boldsymbol{I}}\sin(\boldsymbol{Q}\cdot\boldsymbol{R_i}))$$

Now we can illustrate the long range antiferromagnetic state on a two-dimensional square lattice. The only constraint on the choice of $\widehat{\boldsymbol{R}}$ and $\widehat{\boldsymbol{I}}$ is that they have to be orthogonal to each other, so we can select $\widehat{\boldsymbol{R}} = \hat{\boldsymbol{x}}, \widehat{\boldsymbol{I}} = -\hat{\boldsymbol{y}}$. Then the choice of $\mathbf{Q} = (\frac{\pi}{a}, \frac{\pi}{a}, 0)$ gives us the traditional Néel state. As shown in Fig 2,

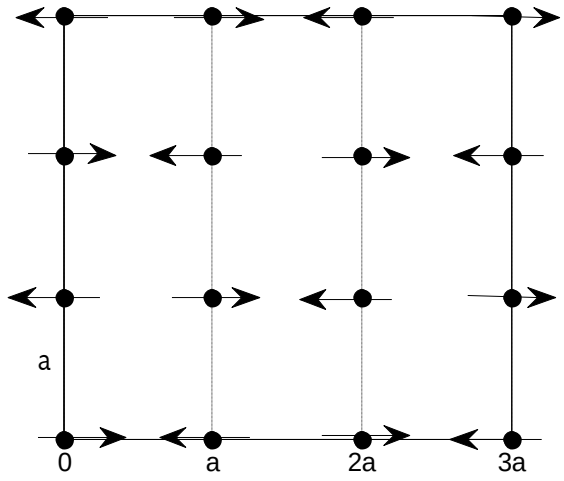

Figure 2 Néel State on 2D square lattice. Neighboring spins are antiparallel to each other.

To show explicitly how we get this antiferromagnetic state, we insert $\widehat{\boldsymbol{R}} = \hat{\boldsymbol{x}}, \hat{\boldsymbol{I}} = -\hat{\boldsymbol{y}}$ to have

$$\boldsymbol{S_i} = S(\hat{\boldsymbol{x}}\cos(\boldsymbol{Q}\cdot\boldsymbol{R_i}) + \hat{\boldsymbol{y}}\sin(\boldsymbol{Q}\cdot\boldsymbol{R_i}))$$

$\boldsymbol{R_i}$ is the lattice vector and on the two dimension square lattice, it can be written as $\boldsymbol{R_i} = (ma, na, 0)$, where m and n are integers. The $\boldsymbol{Q}\cdot\boldsymbol{R_i} = (m+n)\pi$, and $\boldsymbol{S_i} = S(\hat{\boldsymbol{x}}\cos(m+n)\,\pi + \hat{\boldsymbol{y}}\sin(m+n)\,\pi) = S(-1)^{m+n}\hat{\boldsymbol{x}}$, which means the orientation of the spins are always along x-axis and neighboring spins are pointing to opposite directions. The resultant antiferromagnetic ordering is visualized in Fig 2.

1.4 Frustrated system and triangular lattice antiferromagnetic

For a spin system with antiferromagnetic interactions, sometimes the spins cannot take the trivial Néel state because of its geometric shape. We call this a magnetic frustrated system. This concept was first introduced by Gérard Toulouse [3] [4] in 1977, and it has been intensely studied for decades.

One example of magnetic frustrated system is the two-dimensional triangular lattice. As shown in Fig 3a, in a triangle, when two spins assume opposite orientations, there is no trivial orientation left for the third one, which indicates a different ground state from the simple Néel state. Other frustrated systems include the Kagome lattice (Fig. 3b) and the Tetrahedron lattice.

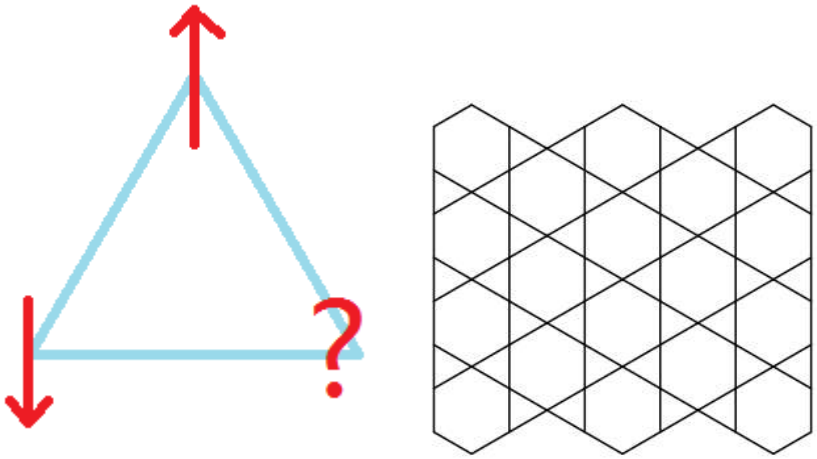

Figure 3 (a) Frustration in triangular lattice. When two spins are antiparallel to each other, the third spin, which is also a nearest neighbor to the other two spins, does not have a well-defined orientation. (b) The Kagome lattice in two dimension.

It has always been an interesting topic to solve the Heisenberg antiferromagnetic model on a geometrically frustrated system, because this may lead to many exotic magnetic ordering or disordered systems.

The two-dimensional triangular lattice first attracted interest from physicists because it is a two-dimensional analog of the face center cubic structure. G.H.Wannier first studied it in an Ising-Model frame [5]. In the Ising model, the spins can only take two possible orientations, and Wannier concluded there is no long range magnetic at any temperature. This conclusion was verified by K. Husimi and I. Syˆozi [6] with a stricter quantum mechanical derivation.

In 1973, P. W. Anderson calculated the energy of a 120 °Néel state and that of a "Resonating Valence Bond" state, and pointed out that the latter had a lower energy [7]. However, the 120 °Néel state Anderson studied was only a quasi-1D lattice since what he calculated was actually the energy of a "railroad trestle" lattice (fig. 4).

Figure 4 Railroad Trestle lattice [7], as proposed by Anderson. The system can be seen as a quasi-1D frustrated lattice.

Since the late 1980s, theorists started to be able to better estimate the ground state energy of a two-dimensional triangular lattice with spin-1/2, and the system was believed to have long-range order with the 120 °state [8] [9]. The 120 °state divides the spin system into three sublattices. Spins in each sublattice point to the same direction, and spins from different sublattices make 120 °angle to each other. All the spin vectors are in the same plane.

As we pointed out in Section 1.2, the difficulty of solving the two-dimensional Heisenberg Antiferromagnetic model is to find the simultaneous eigenstates of H and S. With the development of technology, especially with the progress in calculation power provided by computers, theorists in the 1990s tried to fully diagonalize the Hamiltonian of the Heisenberg model on a finite-size lattice. Up to 1999, scientists were able to solve the quantum Heisenberg antiferromagnetic model on triangular lattice with

144 sites, each occupied by a 1/2 spin [10]. These numerical calculation provided strong evidence that the 120 ℃phase is the ground state of triangular lattice antiferromagnet (TLA) at zero field.

The previous discussions are limited to zero field condition. When a magnetic field perpendicular to the triangular plane is turned on, the Hamiltonian becomes

$$\mathrm{H} = -\sum_{ij} J_{ij} \boldsymbol{S_i} \cdot \boldsymbol{S_j} - h \sum_{i} S_i^z$$

If we assume an isotropic lattice, the model can be further simplified to be

$$\mathrm{H} = -\mathrm{J} \sum_{ij} \boldsymbol{S_i} \cdot \boldsymbol{S_j} - h \sum_{i} S_i^z,$$

Where J<0 to account for the antiferromagtism, and i, j run through all the nearest neighbors. This model, although simplified, is still not trivial to solve, but the introduction of the Monte- Carlo method as a way of numerical calculation can help us to identify many important features of the triangular lattice antiferromagnet. Seabra, *et al* thus proposed a phase diagram for the two-dimensional triangular lattice, according to their Monte- Carlo simulation (see Fig 5) [11].

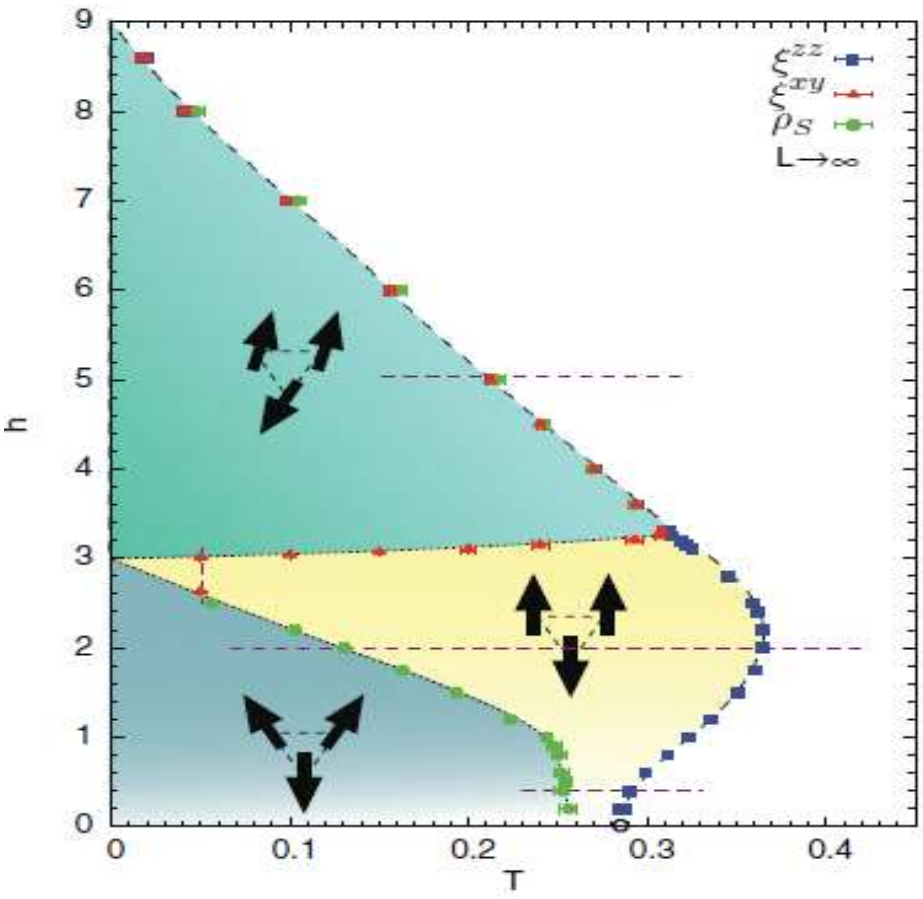

Figure 5 Monte-Carlo simulation results of the classical Heisenberg Antiferromagnetic model for 2D triangular lattice [11]. At zero temperature, there is a quantum critical point at 1/3 of the saturation field. The uud state only exists at finite temperature.

From this phase diagram, we can see that at zero field, the ground state is the 120 °state, and as we turning on the field, there is a quantum critical point at 1/3 of the saturation field. At non-zero temperature, there is a phase transition from the 120 °phase to a so-called "up-up-down" (uud) phase, which is stabilized by thermal fluctuations. The uud phase is featured by two sublattices with spin-up and the other sublattice with spin-down, which gives an averaged spin magnetization 1/3 of the fully saturated value over a certain range of magnetic field (the magnetic plateau). I will discussed the uud phase

in more detail in the following section. Upon increasing the field, where is another phase transition from the uud phase to the "canted" phase. All the three phases in the phase diagram are coplanar, with all spins in the same plane perpendicular to the triangular surface.

1.5 The up-up-down phase

The first theoretical indication of the up-up-down phase came from a numerical calculation by H. Nishimori *et al* [12]. They proposed a Hamiltonian for the quantum Heisenberg antiferromagnetic model on a 2D triangular lattice with spin-1/2

$$\mathrm{H} = 2\mathrm{J}\sum_{ij}\left(S_i^x S_j^x + S_i^y S_j^y + AS_i^z S_j^z\right) - h\sum_i S_i^z \quad (\mathrm{J} > 0)$$

In this Hamiltonian, A represents an exchange anisotropy. H. Nishimori *et al* ran the numerical calculation on a 12-site lattice (Fig 6a) and an 18-site lattice (Fig 6b), diagonalize the Hamiltonian, and found the ground state magnetization as a function of applied field.

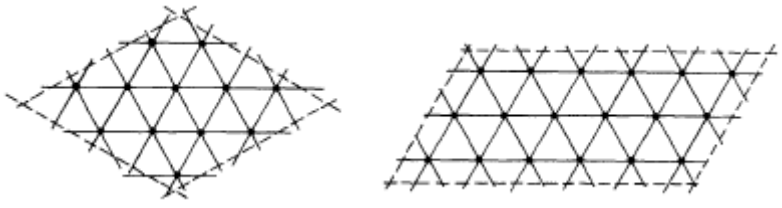

Figure 6 (a) 12-site lattice [12]. (b) 18-site lattice [12]

We cite the resultant magnetization from Nishimori's paper [12] in Figure 7 (12-site) and Figure 8 (18-site). From these figures, we can see a magnetic plateau between a field range $h_{c1} \leq h \leq h_{c2}$, and the onset of the magnetic plateau h_{c1} does not strongly depend on the anisotropy factor A, - it is always about 1/3 of the saturation field. On the other hand, the size of the magnetic plateau, or the position of the second critical field h_{c2}, obviously depends on the anisotropy of the spin system.

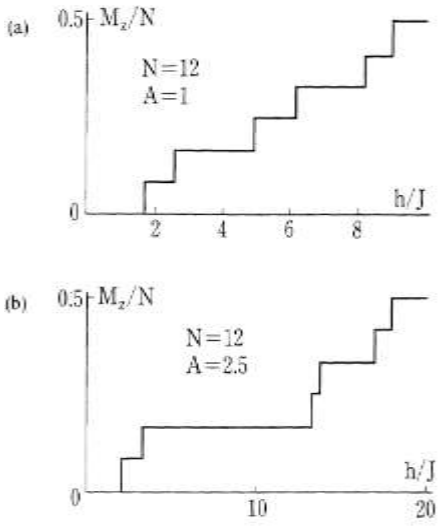

Figure 7 12-site lattice, magnetization as a function of field. Figures from ref [12].

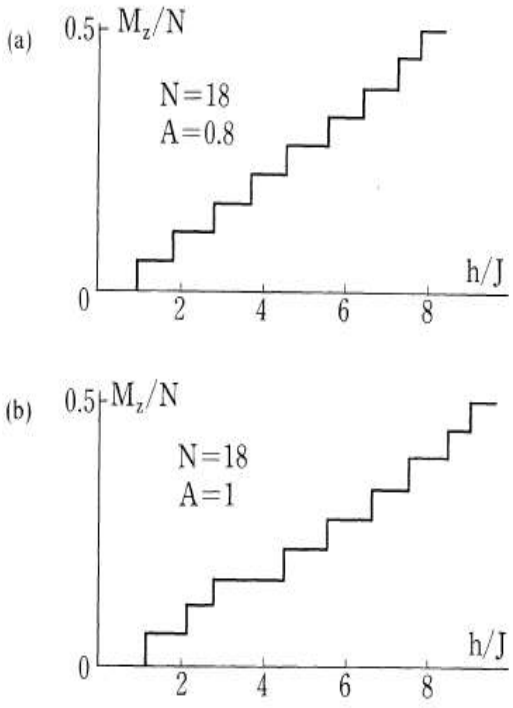
(a)
0.5
M_z/N
N=18
A=0.8
h/J
0
2
4
6
8
(b)
0.5
M_z/N
N=18
A=1
h/J
0
2
4
6
8

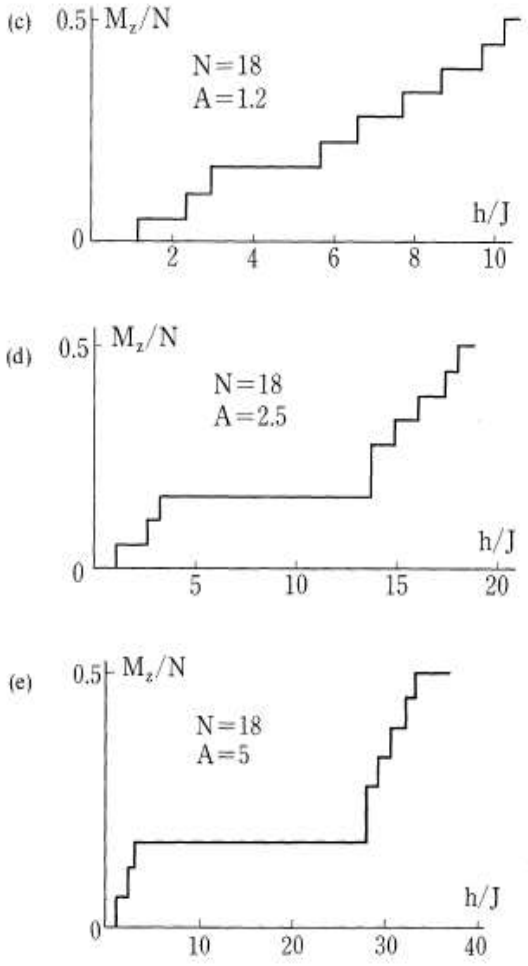

Figure 8 18-site lattice, magnetization as a function of field. Figures from ref [12]

To explain this magnetic plateau, H. Nishimori and S. Miyashita [12] proposed the up-up-down phase, in which the system is divided into three sublattice, with spins in two sublattices pointing to one direction and spins in the other sublattice pointing to the opposite direction. All the spins are parallel to the z-direction, which we call an easy-axis type of magnetic ordering. The 2:1 ratio of the spins give an average magnetization 1/3 of the saturated value.

We should notice that the result of the quantum model resembles that of the classical picture (fig 5) in the sense that at zero temperature in the classical phase diagram, we also observe a critical point at 1/3 of the saturated field. However, in the classical limit, up-up-down phase can only exist at non-zero temperature, while in the quantum picture, the quantum fluctuation help to stabilize the uud phase, and critical point opens up.

The theoretical work on the up-up-down phase run over the experimental discovery by almost twenty years. The difficulty in synthesizing high-quality triangular lattice crystals delayed the discovery of 1/3 magnetic plateau until it was observed in Cs_2CuBr_4 [13] [14]. However, the triangular lattice of this compound is distorted, and in analyzing the magnetization process, physicists found that the Dzyaloshinskii-Moriya (DM) interaction plays an important role. The DM interaction is an antisymmetric exchange mechanism contributing to the total magnetic interaction between two neighboring magnetic spins. It was first postulated by Igor Dzyaloshinskii [33] and then extended by Toru Moriya [34]. In magnetically ordered systems, the DM interaction favors spin canting rather than (anti)parallel alignment with the applied field, and is thus a source of weak ferromagnetic behavior in an antiferromagnet. A common example of DM interaction is two neighboring ions interacting with each other through a third ion by the superexchange mechanism. In comparison to Cs_2CuBr_4, the $Ba_3CoSb_2O_9$ single crystal has many advantages that make it a better choice to explore the full

magnetic phase diagram. We will discuss this further in a later section.

1.6 Triangular lattice antiferromagnet with interlayer coupling

In actual experimental work, it is not easy to synthesize a pure 2D triangular lattice material. The best approximation is usually a compound with triangular plane stacking in the perpendicular direction (c-direction by convention) to form a layered structure. In this case, if the interlayer coupling is weak enough compare to the intralayer coupling, it can be a good substitute of the two-dimensional lattice. However, since the interlayer coupling always exists, it certainly play a role in the magnetic properties of the compound. R. S. Gekht and I. N. Bondarenko systematically explored the phase diagram of a triangular antiferromagnet with a layered structure from a theoretical aspect. We summarize their main results below [15].

The Hamiltonian is defined as

$$\mathcal{H} = 2J \sum_{<i,j>n} \boldsymbol{S_{in}} \cdot \boldsymbol{S_{jn}} + 2J' \sum_{in} \boldsymbol{S_{in}} \cdot \boldsymbol{S_{i,n+1}} - \mu \boldsymbol{H} \cdot \sum_{in} \boldsymbol{S_{in}},$$

where the summation with respect to <i, j> is over all the nearest pairs in the *n*th layer. The second term represent the interlayer coupling, and J' is the interlayer exchange energy. The last term is the Zeeman energy, which cannot be ignored as the external field is not zero. The direction of field is assumed to be along c axis (or

z-axis), which is perpendicular to the triangular plane.

To determine the magnetic order, we have to know the angle between the field the spin, which we label as θ. In the classical two-dimensional model, the spin lattice is divided into three sublattices. In the layered structure model, the periodicity of stacking is two, so it is divided into 6 lattices. The energy of the 6-sublattice structure can be written as

$$\frac{E_0}{N} = J\sum_{\alpha>\beta} \boldsymbol{S_\alpha}\cdot\boldsymbol{S_\beta} + \frac{2}{3}J'\sum_{\alpha} \boldsymbol{S_\alpha}\cdot\boldsymbol{S_{\alpha+3}} - \frac{1}{6}\mu H\sum_{\alpha} S_\alpha^z$$

In this equation, we treat the spins as regular 3-components vectors, so it works in the classical limit, e.g. for large spin S. To get the equilibrium state, we just need to minimized the energy

$$\frac{\partial E_0}{\partial \theta_\alpha} = 0, \qquad \frac{\partial E_0}{\partial \varphi_\alpha} = 0$$

θ_α is the angle between the α sublattice and the c-axis, and φ_α is the azimuthal angle. There are actually many solutions with different structures. R. S. Gekht and I. N. Bondarenko proposed nine possible structures and calculated the energy of each possibility. Here I will only show the results of the umbrella phase, the up-up-down phase and the "Y" phase

In the umbrella phase, as shown in Fig 9, the 6 sublattices form a non-planar structure with the same inclination angle θ. The resultant azimuthal angle and the energy are

$$f(x) = \begin{cases} \frac{2\pi(\alpha-1)}{3}, & \text{if } \alpha = 1,2,3 \\ \frac{(2\alpha-5)\pi}{3}, & \text{if } \alpha = 4,5,6 \end{cases}$$

$$\frac{E_0}{N} = -(3J + 2J')S^2 + (9J + 4J')S^2 cos^2\theta - \mu HScos\theta$$

The saturation field $H_s = (18J + 8J')S/\mu$, and the equilibrium condition is $\cos\theta = \frac{H}{H_s}$. Putting these substitution in to obtain

$$\frac{E_*}{N} = \frac{E_0}{N} = -(3J + 2J')S^2 - \frac{1}{2}\mu S H_s h^2, \quad h = \frac{H}{H_s}$$

We denote the energy of the umbrella phase as E_* so later we can compare the energy of different phases.

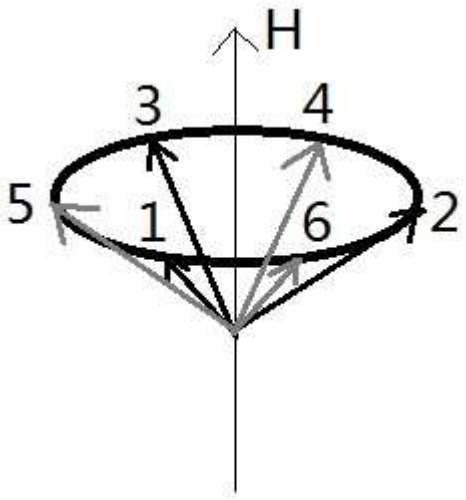

Figure 9 umbrella phase with a 6-sublattice structure. All the sublattice magnetizations have the same angle with the applied field.

In the up-up-down phase, as shown in Fig 10, all the 6 sublattices are in the same plane parallel to c-axis. Sublattice 1 and 6 have $\theta = \pi$, and for the other 4 sublattices, $\theta = 0$. Assuming the spin S is large, the energy of this state is calculated to be

$$E_0 = E_* + [(1-3h)^2 + \frac{4}{3}j(1-2h+3h^2)]JS^2N,$$

where $j = J'/J$ is the ratio between interplanar coupling and the intraplanar coupling.

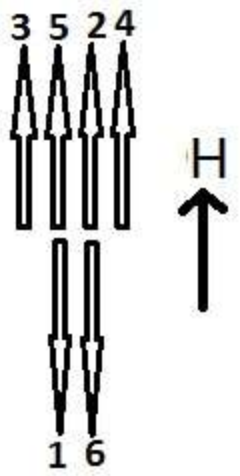

Figure 10 the up-up-down phase with a 6-sublattice structure. Four sublattices are parallel to the applied field, while the other two sublattices are antiparallel to the field. Thus the averaged magnetization is 1/3 of the full magnetization.

In the classical 2D triangular antiferromagnet, the ground state is the Y phase (see Fig 5). When there is a layered structure, the counterpart of the Y phase is shown in Fig 11, with antiferromagnetic interaction between adjacent layers. $\theta_1 = \pi, \theta_2 = -\theta_3 = \theta, \theta_4 = 0, and\ \theta_5 = -\theta_6 = \chi$. The energy of this state (in the classical limit) is

$$\frac{E_0}{N} = JS^2(\cos 2\theta + \cos 2\chi) - \left(2JS^2 + \frac{\mu HS}{3}\right)cos\theta + \left(2JS^2 - \frac{\mu HS}{3}\right)cos\chi - \frac{2}{3}J'S^2 \times [1 - 2\cos(\theta + \chi)]$$

Minimizing the energy with respect to θ and χ to obtain the field dependence of

the angles:

$$cos\theta = \frac{3h+1}{2} - \frac{1}{3}jh, \qquad cos\chi = \frac{3h-1}{2} - \frac{1}{3}jh.$$

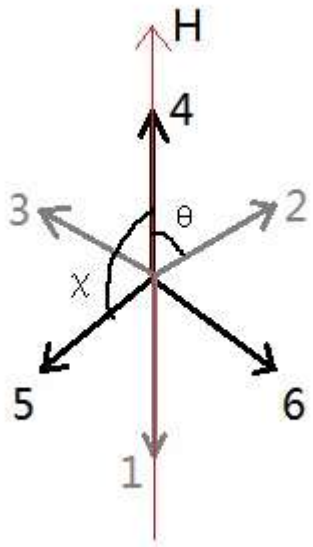

Figure 11 the "Y" phase with 6-sublattice structure. The most prominent feature of this state is that two sublattices are antiparallel to each other along the direction of the applied field.

Gekht and Bondarenko worked out a “jS-h” phase diagram for the ground state in the large-spin limit. To help the reader better understand the phase diagram, I cite Fig 1 from ref [15] to show the 9 phases they studied. The phase diagram is shown in Fig 13. From the phase diagram, we can see that for non-zero interlayer coupling, the antiferromagnetic “Y” phase (Phase (f) in Gekht’s notation) is always the ground state at zero field. Approaching the saturation field, it is the umbrella phase (Phase (a) in Gekht’s notation) that has the lowest energy level. The up-up-down phase (Phase (c) in Gekht’s notation) exists for a certain range of j, and the onset of the uud phase is again roughly 1/3 of the saturation field.

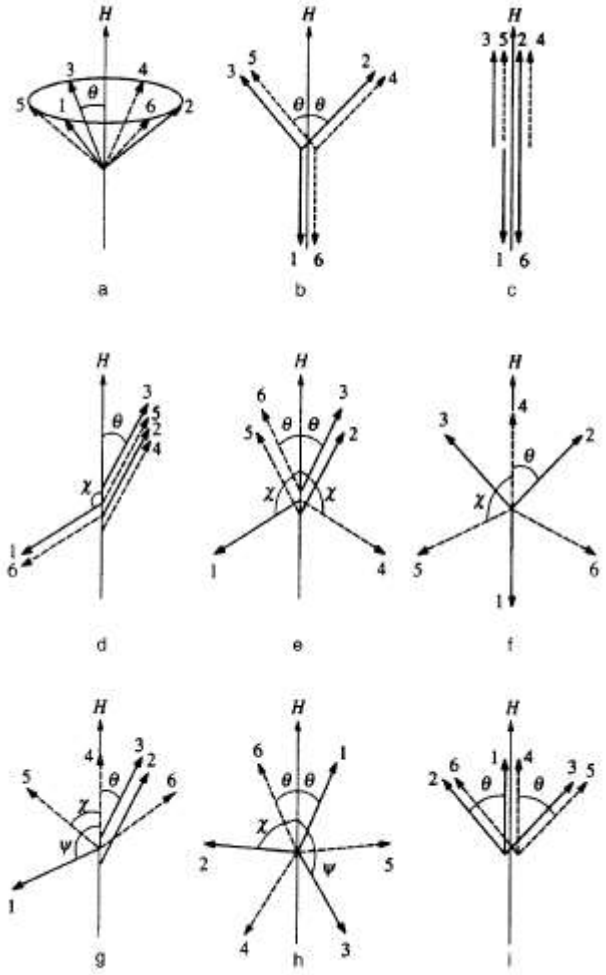

Figure 12 Fig 1 from ref [15]. The possible spin-configurations for quasi-2D triangular lattice antiferromagnet.

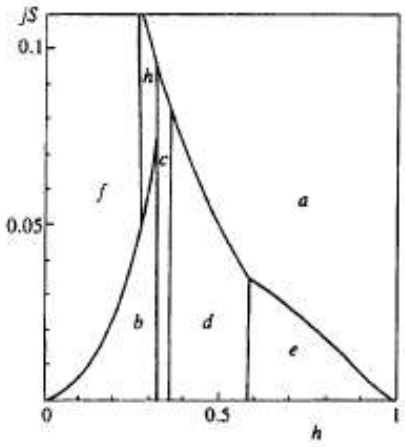

Figure 13 The jS-H phase diagram from ref [15]

Chapter Two

Structural Properties and Preliminary Work on $Ba_3CoSb_2O_9$

The magnetic frustration has induced many exotic disordered ground states like the quantum spin liquid state, in which the spin system is prevented from ordering by the quantum fluctuation and remains at a liquid-like state even at the lowest temperature experimentalists can reach. As an example, the organic κ-$(BEDT\text{-}TTF)_2Cu_2(CN)_3$ compound has been studied intensely and is assumed to be a candidate for the quantum spin liquid state. On the other hand, the realization of the magnetic plateau is rare, and before $Ba_3CoSb_2O_9$, the other compound showing this feature is the Cs_2CuBr_4 [37] [38]. However, for Cs_2CuBr_4, the antisymmetric Dzyaloshinshy-Moriya (DM) interaction plays an essential role in the magnetization process, which is not typical for the isotropic triangular lattice system.

The discovery of the 1/3 magnetic plateau makes $Ba_3CoSb_2O_9$ an important compound in the study of triangular lattice antiferromagnet. As mentioned, the first spin-1/2 system that has a magnetic plateau is the Cr_2CuBr_4 compound, which has a distorted triangular lattice. In contrast, the in-plane homogeneity of $Ba_3CoSb_2O_9$ is much better and that makes the comparison of the experimental results and the theoretical prediction

more meaningful. Furthermore, the nearest-neighbor exchange energy of $Ba_3CoSb_2O_9$ is only 19.5K, and the effective spin of the ground state is 1/2, the saturation field is thus relatively low (~30T according to the magnetization measurements [16] [17]). The low saturation field indicate a possibility to explore the full H-T phase diagram, which would make a perfect comparison to the theoretical model.

2.1 The lattice structure of $Ba_3CoSb_2O_9$

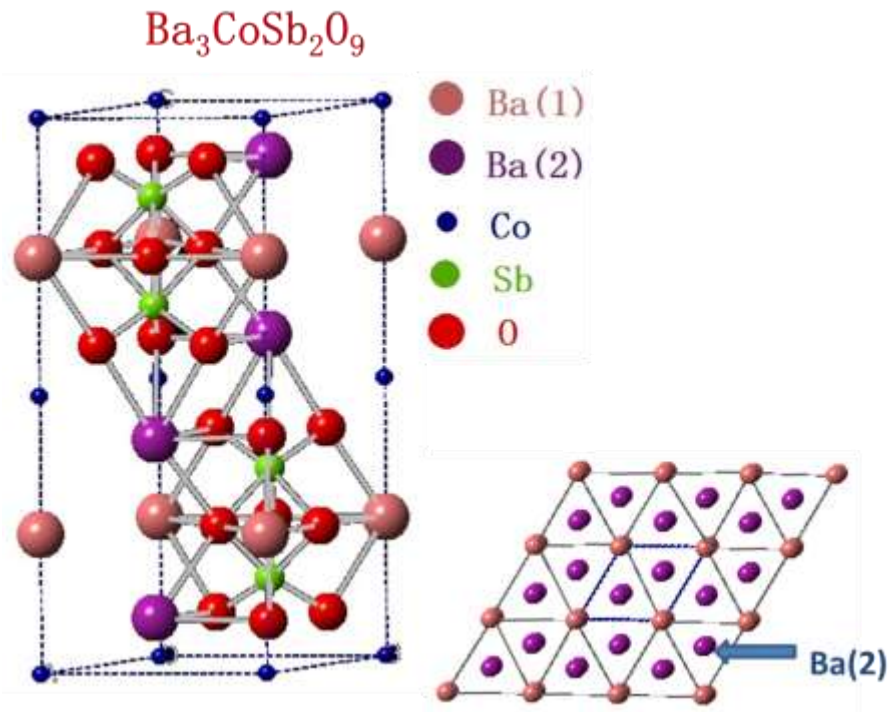

Figure 14 Structure of $Ba_3CoSb_2O_9$

The Structure of $Ba_3CoSb_2O_9$ is shown in Fig 14. This compound crystallizes in a highly symmetric hexagonal structure, $P6_3/mmc$, which has triangular planes formed by the magnetic Co^{2+} ions in the CoO_6 octahedron. These planes stack directly to one

another in the c-direction. A face-sharing Sb_2O_9 double octahedron sits right in the midway between two triangular layers. There are two different Ba sites in the compound, which I will discuss in detail in a later section. The structural parameters were first measured by Y Doi, *et al* [18], and the numbers are a=5.8413(1)Å, c=14.4283(2)Å, where a is the distance between two nearest Co^{2+} in the same plane, and c is twice the distance between a Co^{2+} and its nearest neighbor in adjacent plane.

The effective spin moment of Co^{2+} in a hexagonal structure was studied by M. E. Lines [19] and H. Shiba [20]. According to the Hund's rule, the free Co^{2+} ion has 7 3d electrons and the total orbital and spin angular momenta are L=3 and T=3/2, respectively. The cubic crystal field split the 7 levels of the orbital momentum L=3 in to 1 orbital singlet and 2 orbital triplet, and the lowest state is a triplet T_1, which is well separated from the others states with an energy gap. The trigonal field is taken as a distortion (perturbation) to the cubic field, and along with the spin-orbital coupling, it splits the $^4T_1$ ground state into 6 Kramers doublets. The lowest energy doublet is effectively a 1/2 spin, and it is separated with the next energy-level doublet by a gap of the order 200-300K [21], so it is legitimate to take the effective spin of Co^{2+} as 1/2 when we work at low temperature (lower than 77K).

The intralayer exchange energy $\frac{J}{k_B} = 19.5K$, and the interlayer exchange energy $\frac{J'}{k_B} = 0.48K$. There is an in-plane anisotropy $\frac{\Delta J}{k_B} = 1.02K$, which is small compared to J. All these numbers on exchange energy were measured by Susuki, *et al* [22]. They evaluated

the exchange energy from the saturation field Hs by using the relation $g\mu_B H_s = 9J/2$. The issue of the g-factors and magnetization measurements will be revisited later.

As a short summary, the $Ba_3CoSb_2O_9$ compound possesses a spin-1/2 triangular plane with a layered structure. There is a weak interplanar coupling and a small intraplanar anisotropy, which makes it a good simulation of the two-dimensional triangular lattice. The fact that the exchange energy is small and that the effective spin moment is 1/2 makes the exploration of the full magnetic phase diagram possible.

2.2 Preliminary data on $Ba_3CoSb_2O_9$- the magnetic and thermal measurements

The first indication of the magnetic ordering in $Ba_3CoSb_2O_9$ came from the susceptibility measurements and the zero-field specific heat measurement by Y. Doi, *et al* [18]. Their results are shown in Fig 15 and Fig 15b.

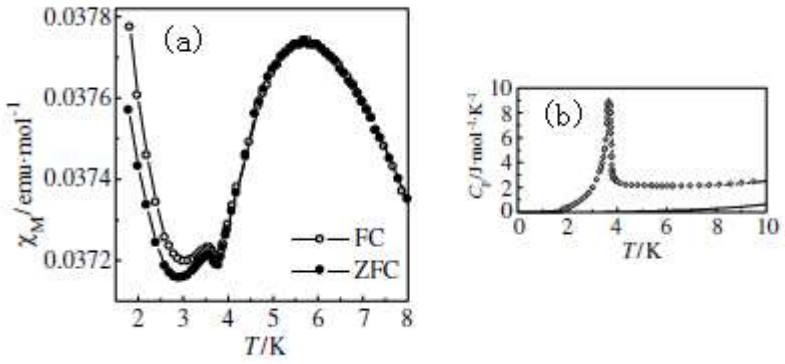

Figure 15 (a) Temperature dependence of magnetic susceptibility of $Ba_3CoSb_2O_9$ at low temperature. A kink is observed at about 3.6K, indicating an antiferromagnetic transition. (b) Temperature dependence of the specific heat of $Ba_3CoSb_2O_9$. Cite from ref [18].

The Magnetic susceptibility has a broad maximum at around 6K and the sharp cusp at 3.8K, while the specific heat data shows a "λ" shape anomaly at 3.8K. They concluded that there is a phase transition into a long-range antiferromagnetic state and they further identified the state as a 120 °state with antiferromagnetic ordering between adjacent layers.

The first experimental proof of the existence of up-up-down phase in $Ba_3CoSb_2O_9$ comes from the magnetization measurements made on a powder sample by Y. Shirata, *et al* [16]. The magnetization data after the subtraction of a temperature-independent Van Vleck paramagnetism are shown in Fig 16, and we can clearly see a magnetic plateau within the field range $0.306 < \frac{\mathrm{H}}{H_s} < 0.479$, which agrees very well with the theoretical prediction from numerical calculations.

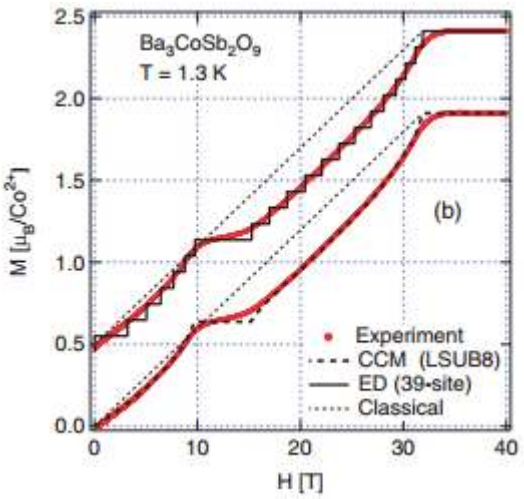

Figure 16 Magnetization curve corrected for Van Vleck paramagnetism [16], in comparison to the "higher order coupled cluster method (CCM)" calculation [23] and the exact diagonalization (ED) for a 39-site rhombic cluster [24] [25]. The 1/3 magnetic plateau can be observed after the correction.

The H-T phase diagram of $Ba_3CoSb_2O_9$ was first explored by H. D. Zhou et al [17]. The group did temperature-dependence magnetization and specific heat measurements at various fields to identify the phase transition points. The measurements were conducted on a piece of single crystal sample. Their main results are shown in Fig 17 (Magnetization) and Fig 18 (Specific heat).

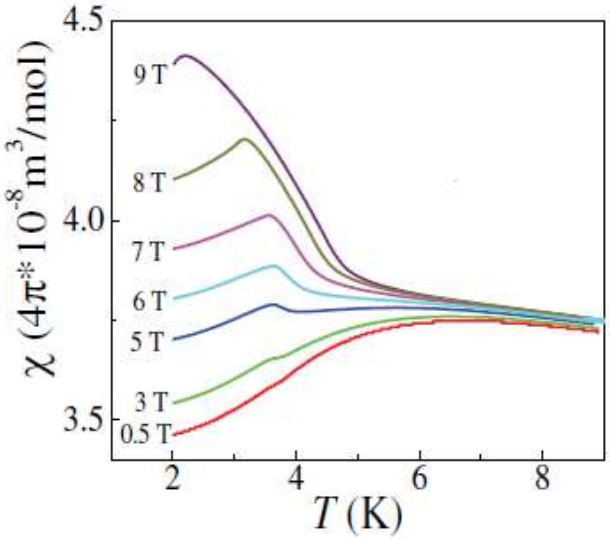

Figure 17 Temperature dependence of spin susceptibility of $Ba_3CoSb_2O_9$ at different fields H//a [17]. For fields between 5T and 9T, two phase transitions can be observed.

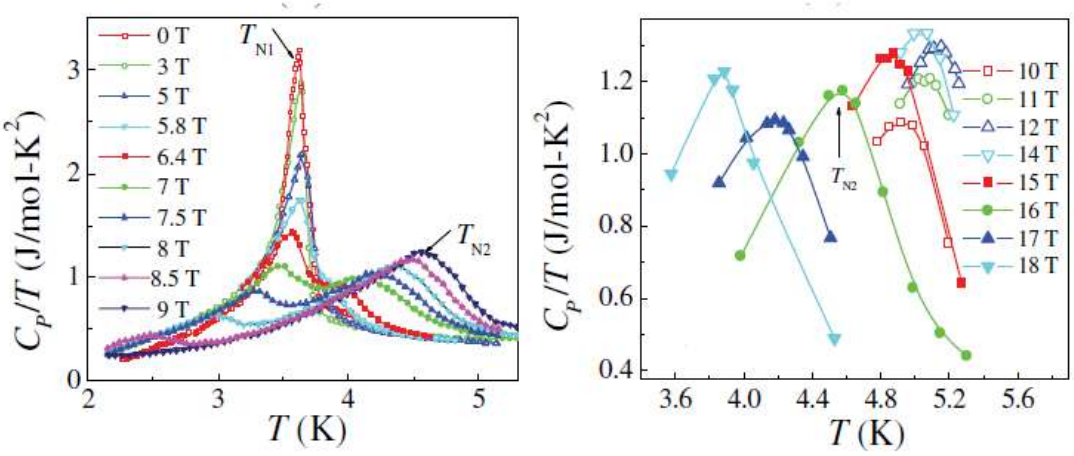

Figure 18 Temperature dependence of C_p/T at different fields H//a [17]. These data were used to plot the phase diagram.

It should be noted that in the original paper of H. D. Zhou et al, the field orientation was labeled incorrectly [22], so what was claimed to be the H//c direction, was actually

H//a direction, and the phase diagram they referred to was also for H//a direction (see Fig 19)

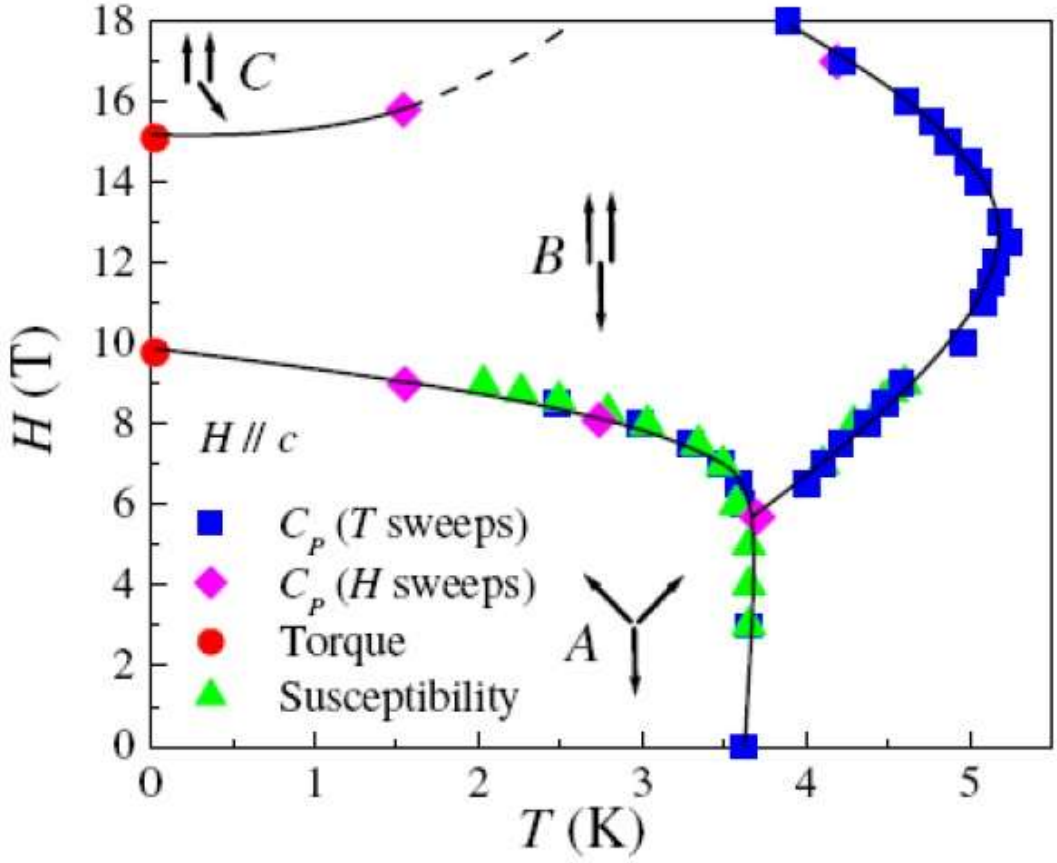

Figure 19 H-T phase diagram for $Ba_3CoSb_2O_9$, H//a [17]. The original work by H.D. Zhou had a mistake in the orientation of the sample, so what they labeled as H//c is actually H//a direction.

In the phase diagram, the authors used a three-sublattice notation, which means they did not identify the inter-plane ordering. The zero field ground state is determined to be the 120 ºphase, and in increasing the applied field, one sublattice is always antiparallel to the field direction, and the other two sublattices are rotating towards parallel-to-field direction, which results in an increase of the magnetization. A phase transition happens when those two sublattices become parallel to field, which is the up-up-down phase.

The up-up-down phase is stable for a finite range of field, and upon increasing the field, there is another phase transition with all the spins becoming canted.

We can see that this phase diagram resembles the results of the 2D classical model in many aspects. I copy Fig 5 (relabeled as Fig 20) here for comparison.

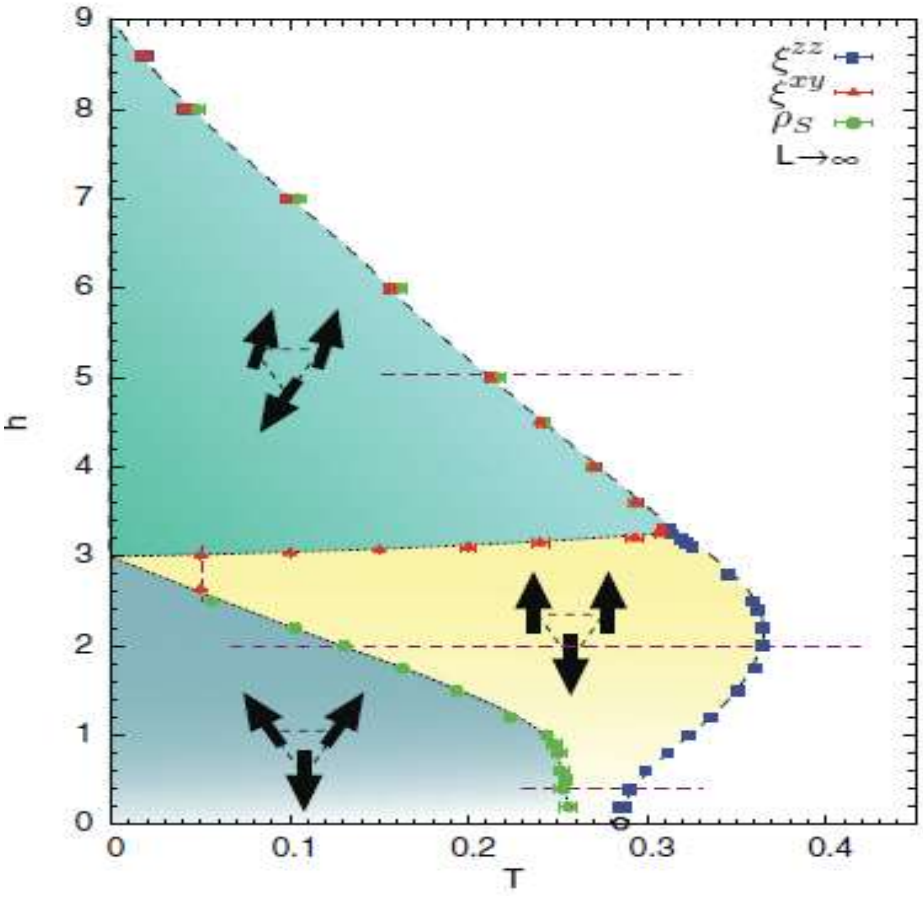

Figure 20 Monte-Carlo simulation results of the classical Heisenberg Antiferromagnetic model for 2D triangular lattice [11].

However, there are two important differences between the experiment and the 2D classical model. First, the uud state at zero temperature is no longer just a critical point, and it can actually exist for a finite range of field. Second, the magnetic

ordering of $Ba_3CoSb_2O_9$ is of an easy-plane type, while in the classical 2D model, it is of an easy-axis type.

2.3 A summary of important structural and magnetic parameters

The $Ba_3CoSb_2O_9$ compound has a triangular lattice formed by spin-1/2 Co^{2+} ions. We define the triangular plane as the ab plane, and perpendicular to the ab plane is the c direction. The saturation fields for both H//ab and H//c sample orientation are determined by magnetization measurements (see Fig 20) [22]. The results are $H_S^{\parallel c} = 32.8T, H_S^{\perp c} = 31.9T$.

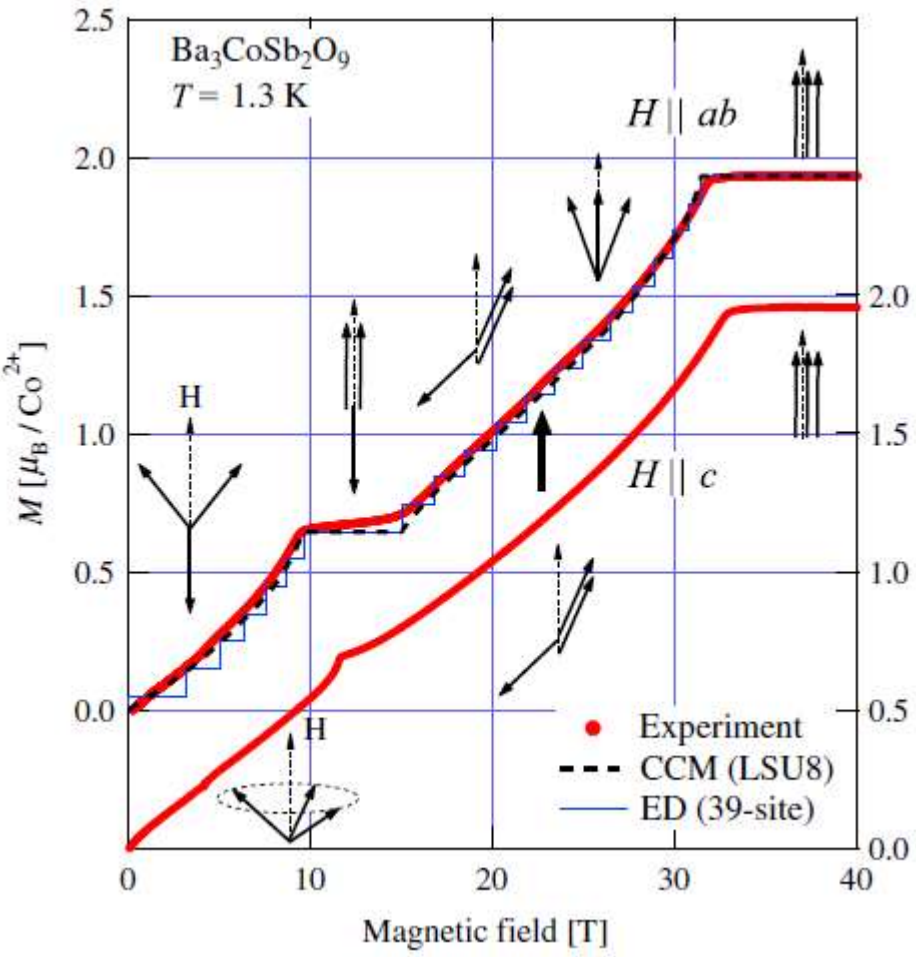

Figure 21 Magnetization of $Ba_3CoSb_2O_9$ after subtraction of the Van Vleck paramagnetism, for both orientations [22]. The magnetic plateau was observed for H//a direction.

The g-factors for both orientations were decided by Electron Paramagnetic Resonance (EPR) measurements [22], and the results are $g^{\parallel c} = 3.87, g^{\perp c} = 3.84$.

The intralayer exchange energy is evaluated by using the relation $g\mu_B H_s = 9J/2$, and the result is $\frac{J}{k_B} = 19.5K$. To determine the interlayer coupling and the in-plane anisotropy, T. Susuki et al plotted a frequency-field diagram of the collective Electron Spin Resonance (ESR) modes for H//c direction, and fit the results with

the equation:

$$\hbar\omega_{\pm} = \sqrt{\left(4J' + \frac{9}{2}J\right)\{\frac{3\Delta J}{4} + \frac{(8J' + 9J - 6\Delta J)}{2(4J' + 9J + 3\Delta J)^2}(g\mu_B H)^2\}} \pm \frac{9J}{8J' + 18J + 6\Delta J} g\mu_B H$$

In this equation, J and J' are the intralayer and interlayer exchange constants, respectively, and ΔJ is the in-plane anisotropy exchange energy defined as $\Delta J(S_i^x S_j^x + S_i^y S_j^y)$. The fitting results give $\frac{J'}{k_B} = 0.48K$, and $\frac{\Delta J}{k_B} = 1.02K$.

2.4 A semi-classical theory for $Ba_3CoSb_2O_9$

Our collaborators Yoshitomo Kamiya and Cristian Batista formulate a semi-classical theory for $Ba_3CoSb_2O_9$, which is an essential contribution. This section introduces their theoretical work.

Recall that the spin-orbital coupling split the $^4T_1$ ground state of Co^{2+} ions into six Kramers Doublets, and there is an energy gap that is much larger compared to the temperature we work at, so we can focus on the lowest energy doublet and write an effective spin-1/2 Hamiltonian

$$\mathcal{H} = \sum_n \mathcal{H}_{2D}^{(n)} + \mathcal{H}_{anis} + \mathcal{H}_{3D}, \quad (1)$$

where

$$\mathcal{H}_{2D}^{(n)} = J \sum_{<ij>} \boldsymbol{S_{n,i}} \cdot \boldsymbol{S_{n,j}} - g\mu_B \boldsymbol{B} \cdot \sum_i \boldsymbol{S_{n,i}} \quad (2)$$

Is the Hamiltonian for a 2D isotropic triangular lattice Heisenberg antiferromagnet

in a magnetic field on the n-th layer and <ij> Runs over the in-plane nearest neighbors. The other two terms, $\mathcal{H}_{anis}$ and $\mathcal{H}_{3D}$, represent the in-plane anisotropy and the interlayer coupling, respectively. $\mathcal{H}_{3D}$ is a small quantity because $J'/J \approx 0.025$. $\mathcal{H}_{anis} = (J_{\parallel} - J)\sum_{n,<ij>} S^z_{n,i} S^z_{n,j}$ is also a small quantity because $\frac{J_{\parallel}}{J} \approx 0.95$ ($J_{\parallel} = J - \Delta J$). In calculation, we can take $\mathcal{H}_{anis}$ and $\mathcal{H}_{3D}$ as perturbations to the 2D isotropic model, and the quantum effects can be included by considering the 2D limit described by $\mathcal{H}^{(n)}_{2D}$.

The magnetic phase diagram of the quasi-2D system is then determined from a balance between the 2D zero-point energy $\Delta E \propto JS$ and the combined effects of interlayer coupling $\propto J'S^2$ and the in-plane anisotropy $\propto (J - J_{\parallel})S^2$. The procedures would be first deriving the effective classical interaction that is induced by quantum fluctuations, and then introducing the effect of the perturbation in a mean-field level.

We first look at the classical ground state of $\mathcal{H}_{2D}$(the index n is omitted because we are considering an arbitrary layer), which has an accidental degeneracy in a magnetic field [26]. We divide the lattice into three sublattices with the unit vectors of the classical sublattice magnetization labeled as $\boldsymbol{\Omega_{\mu=1,2,3}}$. The classical ground state is completely specified by the condition:

$$\boldsymbol{\Omega_1} + \boldsymbol{\Omega_2} + \boldsymbol{\Omega_3} = \frac{g\mu_B \boldsymbol{B}}{3JS} \quad (3)$$

For illustration purpose, I show the sketches of “Y”, “inverted Y”, “UUD”, ”V”,

and umbrella states in Fig 22.

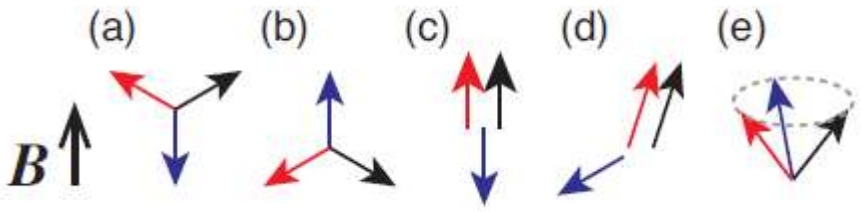

Figure 22 Representative states of the isotropic TLHAF in 2D: (a) Y; (b) inverted Y; (c) up-up-down (uud); (d) V, and (e) umbrella states [27].

The approach applied by Y. Kamiya and C. Batista was to compute the zero-point energy ΔE of a given classical ground state $\{\boldsymbol{\Omega_\mu}\}$ by expanding the Hamiltonian up to quadratic order in Holstein-Primakoff bosons (linear spin waves) and calculating the Bogoliubov dispersion $\omega_{\boldsymbol{k},\nu}$. The index $\nu = 1,2,3$ denotes the three branches associated with the three sublattices. The result is

$$\Delta E\left(\{\boldsymbol{\Omega_\mu}\}\right) = \frac{1}{2}\sum_{k\in BZ}\sum_{1\le\nu\le3}\omega_{\boldsymbol{k},\nu}\left(\{\boldsymbol{\Omega_\mu}\}\right) - \frac{3N_{2D}}{2}JS \quad (4)$$

In this equation, N_{2D} is the total number of sites per layer and BZ stands for the Brillouin zone in 2D.

The zero point energy can be also written as a polynomial function of $\boldsymbol{\Omega_1}, \boldsymbol{\Omega_2}, and\ \boldsymbol{\Omega_3}$. Specifically we have the equation

$$\frac{\Delta E(\{\boldsymbol{\Omega_\mu}\})}{N_{2D}} \approx g_1(M)S^2\sum_{1\le\mu\le3}\left(\boldsymbol{\Omega_\mu}\cdot\boldsymbol{\Omega_{\mu+1}} - 1\right) + g_2(M)\sum_{1\le\mu\le3}\left[\left(\boldsymbol{\Omega_\mu}\cdot\boldsymbol{\Omega_{\mu+1}}\right)^2 - 1\right]$$

$$\equiv g_1(M)S^2F_1\left(\{\boldsymbol{\Omega_\mu}\}\right) + g_2(M)F_2\left(\{\boldsymbol{\Omega_\mu}\}\right) \quad (5)$$

In this equation, $g_1(M)S^2$ and $g_2(M)$ are the effective coupling constants of the order O(S). $M = g\mu_B B/9JS$ refers to the magnetization in the classical limit. $F_1(\{\boldsymbol{\Omega_\mu}\})$ and $F_2(\{\boldsymbol{\Omega_\mu}\})$ are defined as $F_1 = F_2 = 0$ in the fully polarized state.

To satisfy the condition of Eq (3), we have $F1 = \left(\frac{9}{2}\right)\left[\left(\frac{M}{M_{sat}}\right)^2 - 1\right]$, which is independent of the spin configuration Ω_μ. Then we can calculate $g_2(M)$ by extracting the energy difference between two classical ground states X and X' (the reference states), which are selected from Y/UUD/V, inverted Y, and umbrella states as shown in Fig 22. The expression of $g_2(M)$ can be derived easily:

$$g_2(M) \approx \frac{\Delta E\left(\left\{\Omega_\mu^{(X)}\right\}\right) - \Delta E\left(\left\{\Omega_\mu^{(X')}\right\}\right)}{N_{2D}\left(F_2\left(\left\{\Omega_\mu^{(X)}\right\}\right) - F_2\left(\left\{\Omega_\mu^{(X')}\right\}\right)\right)} \quad (6)$$

To check the consistency of the results, different combinations of reference states are selected and the results are shown in Fig 23.

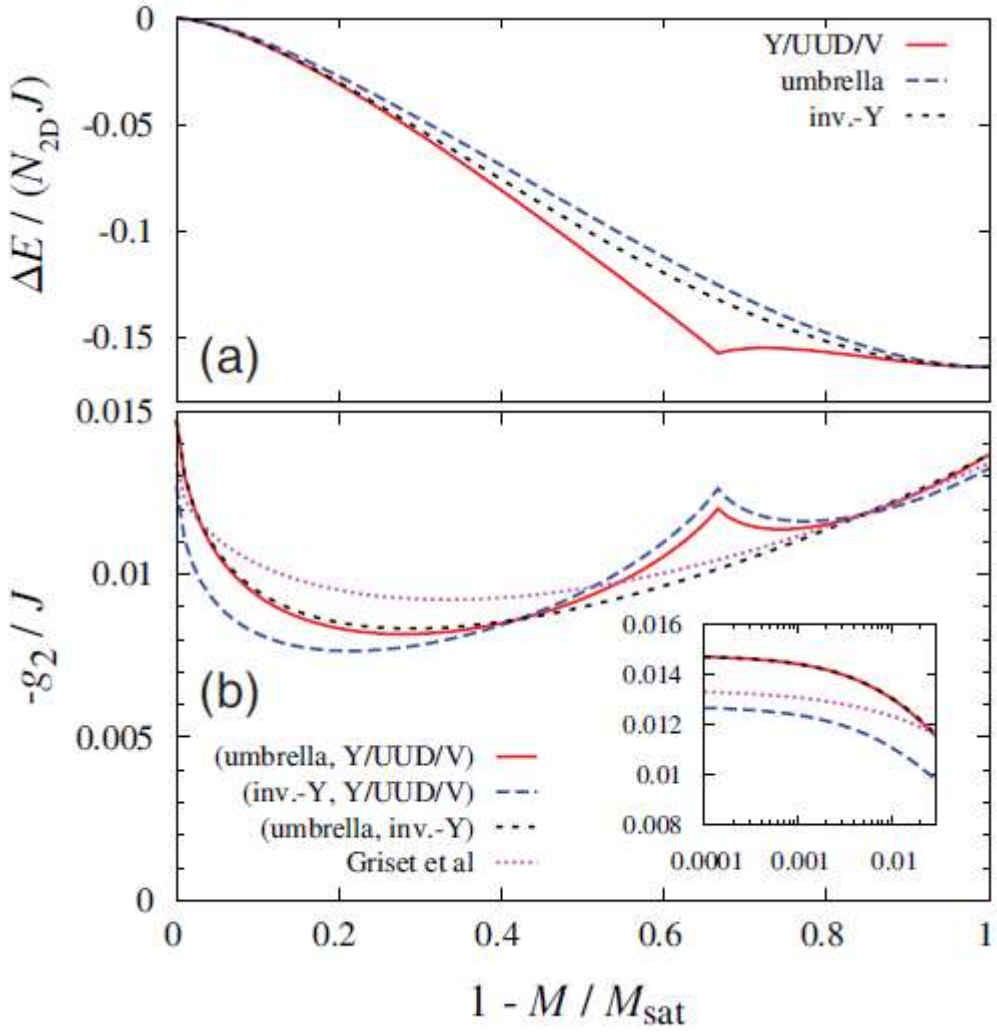

Figure 23 Field-dependence of (a) the 2D zero-point energy, and (b) the effective biquadratic coupling. The different estimators shown in panel (b) are the results of using different reference states in Eq. (6). For comparison, a functional form proposed by Griset, *et al* (ref [28]) is also shown.

From Fig 23, we can see that the different reference states give consistent estimates of the same order (≈-0.01J), except for the cusp at $M=M_{sat}/3$, which is generated by the UUD state. This observation suggests that Eq. (5) is indeed a very good approximation, and the negative value of $g_2(M)$ indicates that the ferro-biquadratic coupling mimics the effect of quantum fluctuations. [28] [29] [30].

Now we are in a position to take into account the effect of $\mathcal{H}_{anis}$ and $\mathcal{H}_{3D}$. We treat the two terms in the mean-field approximation, and write the energy density based on a sin-sublattice structure:

$$\frac{E}{N_{tot}} = \frac{1}{2}\sum_{\xi=e,o}\sum_{1\le\mu\le3}\Big[\big(J+g_1(M)\big)S^2\boldsymbol{\Omega}_{\xi,\mu}\cdot\boldsymbol{\Omega}_{\xi,\mu+1} + (J_{\parallel}-J)S^2\Omega^z_{\xi,\mu}\Omega^z_{\xi,\mu+1} + g_2(M)\big(\boldsymbol{\Omega}_{\xi,\mu}\cdot\boldsymbol{\Omega}_{\xi,\mu+1}\big)^2\Big] + \frac{J'S^2}{3}\sum_{1\le\mu\le3}\boldsymbol{\Omega}_{e,\mu}\cdot\boldsymbol{\Omega}_{o,\mu+1} - \frac{g\mu_B S\boldsymbol{H}}{6}\cdot\sum_{\xi,\mu}\boldsymbol{\Omega}_{\xi,\mu} \quad (7)$$

In this equation, N_{tot} is the total number of sites in three dimension, $\xi = e, o$ refers to even (e) and odd (o) layers, and $1 \le \mu \le 3$ is the sublattice index. $g_2(M)$ is obtained by adopting the Y/UUD/V and umbrella states as X and X' in Eq. (6), respectively. The spin orientations and thus the magnetic ordering are determined by minimizing the energy with respect to θ and φ. The definition of the two angles are shown in Fig 24. From the figure, we can see that θ is the angle between the field direction and the c-axis of the Ba3CoSb2O9 lattice. The minimization process can be done in principle by making the first partial derivative with respect to θ and φ to be zero:

$$\frac{\partial E}{\partial\theta} = 0, \quad \frac{\partial E}{\partial\varphi} = 0 \quad (8)$$

The resultant phase diagram is shown in Fig 25. [27] To help understand the phase diagram and the spin configurations of the six-sublattice structure, 9 possible magnetic states are shown in Fig 26, including those show up in the phase diagram.

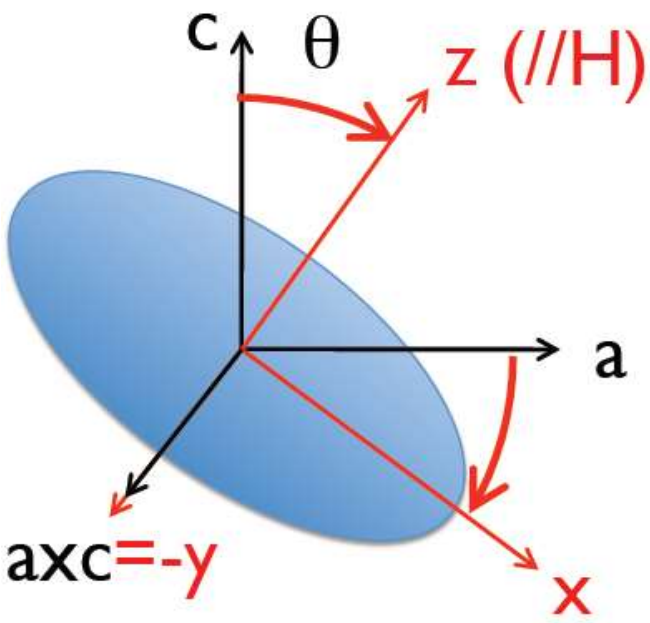

Figure 24 The reference system used in the calculation. a and c are the lattice axes, and z-axis is always parallel to the applied field. The angle between c and z axis is thus the angle between the crystal c-axis and the applied field.

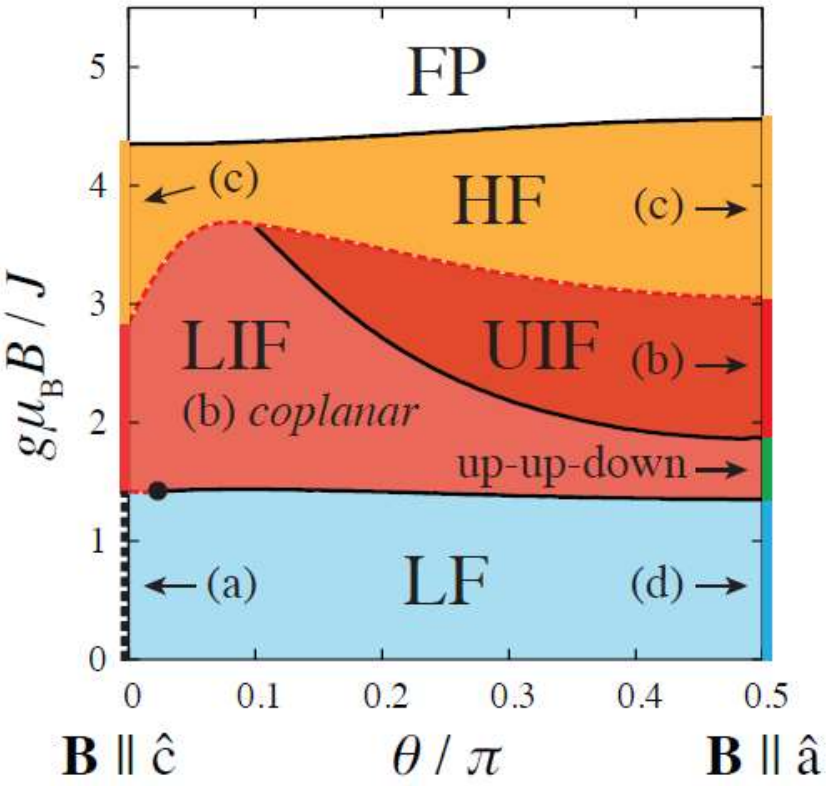

Figure 25 Mean-field phase diagram parameterized by the magnetic field orientation (θ) and strength ($g\mu_B$B/J). The five different phases are demoted as low-field (LF), lower intermediate-field (LIF), upper intermediate-field (UIF), high-field (HF), and fully-polarized (FP) phases.

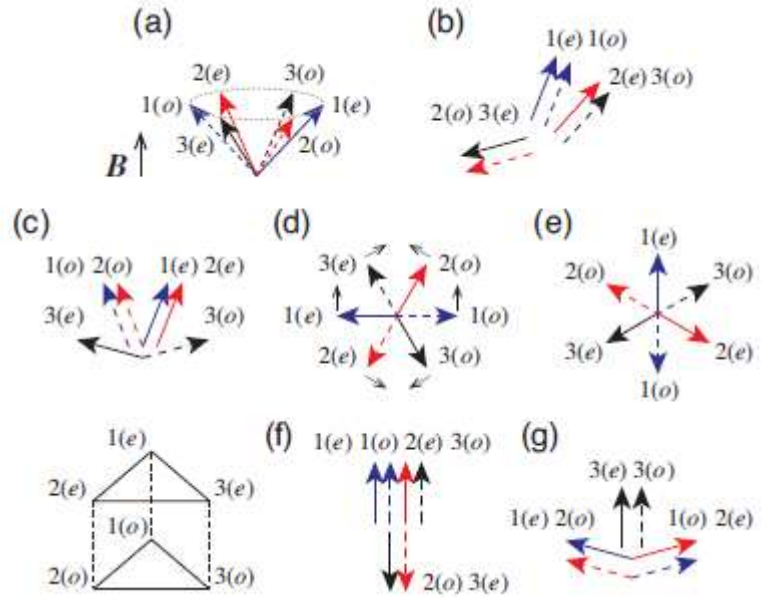

Figure 26 Magnetic states in 3D: the non-coplanar states in the LF, UIF, and HF phases for an intermediate value of $0<\theta<\pi/2$ are similar to (d), (b), and (c), respectively, but they are deformed because of the competition between the external magnetic field and the anisotropy.

Since our experiment focused on the B//c (field perpendicular to the triangular plane) and B//ab (field in plane) directions, it is necessary to make a short summary about the phase diagram.

For the B//c direction, the ground state at low field is the umbrella, which is a non-coplanar phase, and all the six sublattices have the same angle θ with the applied field. As the field increasing, there is a phase transition, after which the magnetic state becomes (b), which is a coplanar phase. Then there is another phase transition and the phase near the saturation is the (c) phase. For this direction, the easy-plane anisotropy dominates the low-field regime ($B \lesssim B_{sat}/3$), stabilizing the umbrella state and

destabilizing the uud phase.

For the B//ab direction, because the field is parallel to the easy plane, the spins are always parallel to the ab-plane, so the phase sequence only contains coplanar phases. The zero field ground state is the (d) phase, which is actually the 120 °state with antiferromagnetic interlayer arrangement, so nearest spins between adjacent layers have opposite directions. As the field going up, four sublattices start to move towards z-direction (the field direction, see Fig 26(d)), and finally the up-up-down phase is built up, which is stabilized by quantum fluctuation. On further increasing the magnetic field, the UUD phase undergoes a second-order phase transition to a high field (b) phase. Finally, as for B//c, the model predicts a first-order phase transition from (b) to (c).This phase transition could be related to the experimental observation of magnetization that around M= (3/5)M_{sat}, there is a tiny jump in M(B) [22].

We can do a quick check of the validity of this semi-classical model. Since we can calculate the orientations of each sublattice as a function of field, we can try to reproduce the results of magnetization measurements. The results are shown in Fig 27 and Fig 28 for B//c and B//ab, respectively.

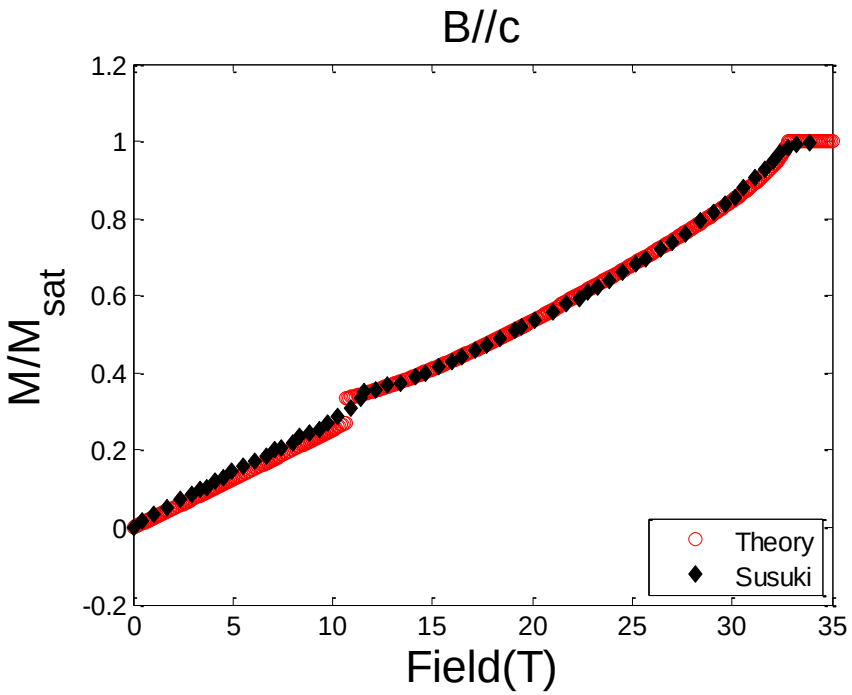

Figure 27 Normalized magnetization B//c. The red curve is the magnetization from the theoretical calculation, and the black points are digitized from Fig 2 in ref [22].

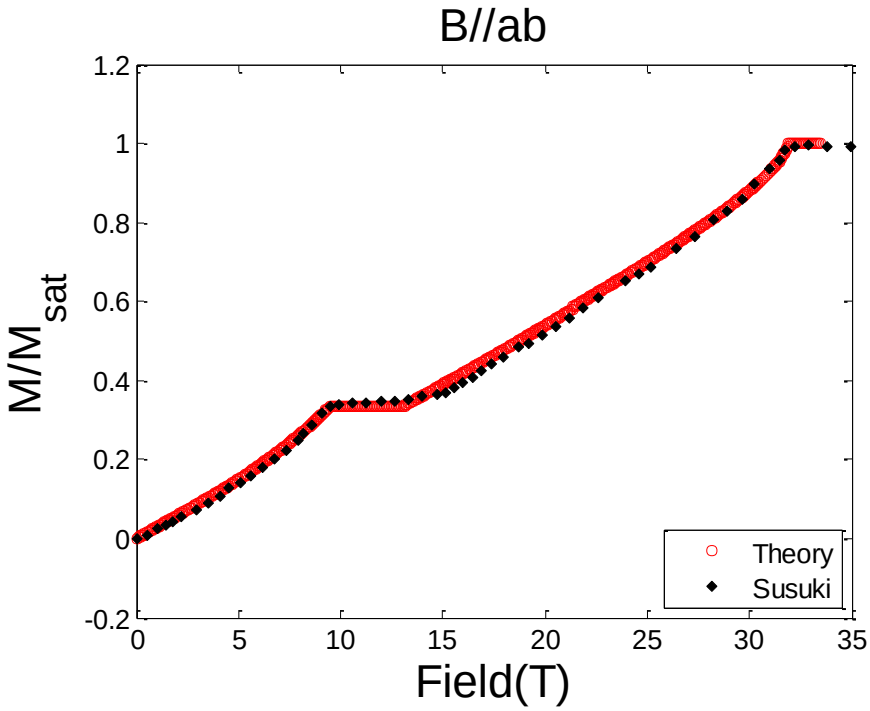

Figure 28 Normalized magnetization B//ab. The red curve is the magnetization from the theoretical calculation, and the black points are digitized from Fig 2 in ref [22]

We can see that for B//c direction, the "kink" feature at about 12T is correctly captured by the theoretical calculation, and for B//a direction, the uud phase is simulated correctly both in the onset field and the width of the uud phase, so the theoretical calculation of the magnetization agrees with the experimental data very well, which is a strong support for the validity of the semi-classical model.

Before closing the theory section, it is useful to comment on the g-tensor anisotropy. Recall that $\Delta J = J - J_{\parallel} > 0$ is the coefficient of anisotropic exchange interaction in the layer defined as $\Delta J(S_i^x S_j^x + S_i^y S_j^y)$, which indicate that it takes lower energy cost to align a uniform magnetization component along the c-axis. In other words, the easy-plane exchange anisotropy implies that it is easier to polarize spins along the "hard" axes (the c-axis). The Zeeman energy required to fully polarize the spins is

$$h_{sat,3D}^{\perp} \equiv g_{\perp}\mu_B B_{sat,3D}^{\perp} = (9J + 4J')S \quad for\ B \perp c \quad (9)$$

$$h_{sat,3D}^{\parallel} \equiv g_{\parallel}\mu_B B_{sat,3D}^{\parallel} = (3J + 6J_{\parallel} + 4J')S \quad for\ B \parallel c \quad (10)$$

It is easy to see $h_{sat,3D}^{\perp} > h_{sat,3D}^{\parallel}\ if\ J > J_{\parallel}$. If we put in the numbers from ref [22]:

$$\frac{J_{\parallel}}{\mathrm{J}} \approx 0.95, \frac{\mathrm{J}'}{\mathrm{J}} \approx 0.025, B_{sat,3D}^{\perp} = 32.8T, B_{sat,3D}^{\parallel} = 31.9T,$$

We obtain

$$g_{\parallel}/g_{\perp} \approx 0.93$$

In fact, $g_{\parallel} < g_{\perp}$ is a rather generic property expected for the pseudospin-1/2 of the Kramers doubles in Co^{2+} ions with easy-plane exchange anisotropy [21]. However, the EPR measurements give $g_{\parallel} = 3.87, g_{\perp} = 3.84, and\ g_{\parallel}/g_{\perp} \approx 1.01$ [22], which is still

controversial at the moment. It is possible that there could be a dynamical shift of the measured g-values because of short-range ordering effects that should still be present at the temperature of the EPR measurements, T=20K, which is comparable to J. EPR measurements at high enough temperature or field will be very helpful to settle this issue.

Chapter Three

NMR shift of $Ba_3CoSb_2O_9$

The magnetization and specific heat measurements play an important role in sketching the phase diagram, because it is quick and straightforward to see the phase transition points. However, these measurement results cannot serve as direct evidence of magnetic ordering, and it is almost impossible to look into the details of spin configurations. In contrast, the nuclear magnetic resonance (NMR) experiment, as a local probe technique, has the advantage of detecting the local magnetic environment of a certain nucleus, and thus is capable of exploring the spin orientations and the magnetic ordering.

3.1 Starting point: magnetic resonance of a single nucleus

Considering a free nucleus with non-zero spin S, the application of a magnetic field $\boldsymbol{H}$ would produce an interaction energy $-\boldsymbol{\mu}\cdot\boldsymbol{H}$, and from the aspect of quantum mechanics, we write it as a simple Hamiltonian

$$\mathcal{H} = -\boldsymbol{\mu}\cdot\boldsymbol{H}$$

If we define the direction of the applied field as z-direction, the Hamiltonian can be simplified to

$$\mathcal{H} = -\gamma\hbar H_0 I_z,$$

where γ is called the gyromagnetic ratio, and $\hbar$ is the Planck's constant. The eigenvalues of this Hamiltonian is simply $-\gamma\hbar H_0 m$, where m is the eigenvalues of I_z. Then the allowed energy levels are

$$\mathrm{E} = -\gamma\hbar H_0 m, \;\; m = I, I-1, \ldots, -I$$

In total there are (2I+1) energy levels. The energy levels for a spin-3/2 nucleus (e.g. Na or Cu) are illustrated in Fig 29. The levels are equally spaced by $\gamma\hbar H_0$.

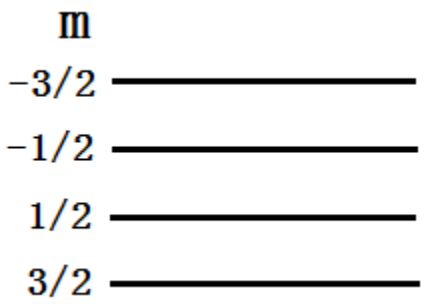

Figure 29 Energy levels for spin-3/2 nuclei in a magnetic field

The split of energy levels shown in Fig 29 is called the Zeeman Effect. To detect the presence of such a set of energy levels, one would need induce a transition between energy levels. If we choose to use electromagnetic waves to achieve this, then from a quantum mechanical view, the energy of photons should be exactly equal to the energy difference between levels:

$$\hbar\omega = \Delta E,$$

where $\omega = 2\pi f$ is the angular frequency of the EM wave, and ΔE is the energy difference between the initial and final energy levels.

In actual experimental work, we usually use oscillating magnetic field to induce the transition, which can be explicitly written as a perturbation Hamiltonian:

$$\mathcal{H}_1 = -\gamma\hbar\left(H_x I_x + H_y I_y\right) = -\frac{1}{2}\gamma\hbar H_1\left(I_+ e^{-i\omega t} + I_- e^{i\omega t}\right),$$

where $H_x = H_1 cos\omega t, H_y = H_1 sin\omega t.$ $I_+ \; and \; I_-$ are ladder operators defined as $I_+ = I_x + iI_y, I_- = I_x - iI_y$.

From the knowledge of quantum mechanics, we know that $I_+ \; and \; I_-$ only have matrix elements between an eigenstates |m〉 and |m ±1〉, which implies the selection rule that the transition can only happen between adjacent energy levels ($\Delta m = 1$). Then we have

$$\hbar\omega = \Delta E = \gamma\hbar H_0 \Delta m = \gamma\hbar H_0$$

$$\omega = \gamma H_0$$

This frequency is called the Larmor frequency, which is also the resonance condition.

It is worthwhile to point out that in the resonance condition $\omega = \gamma H_0$, the Planck's constant has disappeared, which indicate that a classical approximation is possible for describing the system. In fact, the classical picture is not only possible, but also quite useful in understanding the NMR experiment.

In the classical picture, we can imagine the nuclear spin to be a magnet, which is in the magnetic field **H**. The field produces a torque on the magnet, which tends to line up the magnet to the same direction of the field. However, if the magnet possess an angular

momentum, it will not move towards the direction of the field. Instead, like a gyroscope, it would proceed about the field.

To be more accurate, as shown in Fig. 30, the field **H** produce a torque on the magnetic moment **μ** of the amount $\boldsymbol{\mu} \times \boldsymbol{H}$. The angular moment is related to the magnetic moment by $\boldsymbol{J} = \gamma\boldsymbol{\mu}$, and the simply from the relation between torque and angular momentum we know $\frac{dJ}{dt} = \boldsymbol{\mu} \times \boldsymbol{H}$, so we obtain the equation:

$$\frac{d\boldsymbol{\mu}}{dt} = \boldsymbol{\mu} \times (\gamma \boldsymbol{H}) \quad (3.1)$$

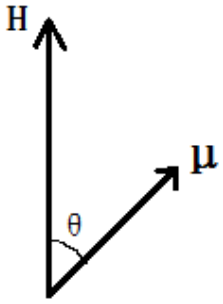

Figure 30. Illustration of a magnetic moment in an external field.

Now we should consider the effect of an oscillating EM field, which is easy to generate in the lab by connecting a solenoid to EM wave generator. We first notice that in the sense of NMR experiment, having an EM field $\boldsymbol{H_1} = 2H_1\hat{\boldsymbol{x}}cos\omega t$ is equivalent to having a field rotating about the lab reference frame z-axis at an angular frequency ω. To justify this, we can write (also see Fig 31)

$$\boldsymbol{H_1} = \boldsymbol{H_R} + \boldsymbol{H_L},$$

where $\boldsymbol{H_R}$ and $\boldsymbol{H_L}$ are rotating fields about z-axis, with opposite direction:

$$\boldsymbol{H_R} = H_1(\hat{\boldsymbol{x}}cos\omega t + \hat{\boldsymbol{y}}sin\omega t)$$

$$\boldsymbol{H_L} = H_1(\hat{\boldsymbol{x}}cos\omega t - \hat{\boldsymbol{y}}sin\omega t)$$

If we take $\boldsymbol{H_R}$ a field rotating about z-axis with angular frequency ω, then $\boldsymbol{H_L}$ can be simply taken as a rotating field with angular frequency $-\omega$. One can show that at frequency near ω, the $\boldsymbol{H_L}$ can be neglected, and we reach the conclusion that the oscillating field $\boldsymbol{H_1}$ is equivalent to a rotating field about the z-axis.

$$\boldsymbol{H_1} = H_1(\hat{\boldsymbol{x}}cos\omega_z t + \hat{\boldsymbol{y}}sin\omega_z t)$$

Now we can consider a spin under the combined effect of a static external field $\mathbf{H_0}$ and a rotating field $\mathbf{H_1}$. Rewrite Eq. (3.1) to get

$$\frac{d\boldsymbol{\mu}}{dt} = \boldsymbol{\mu} \times \gamma[\boldsymbol{H_0} + \boldsymbol{H_1}(t)] \quad (3.2)$$

Calculation about Eq. (3.2) can be made much easier if we solve it in a rotating reference frame. We should assume the angular velocity of the rotating frame relative to the laboratory frame is $\boldsymbol{\omega} = (0, 0, \omega_z)$, which means it rotates about z-axis of the lab frame at the same frequency as $\boldsymbol{H_1}$. We further assume that $\boldsymbol{H_1}$ is always on the x'-axis (we label the axes of the rotating frame as x', y', and z'=z) of the rotating frame, so

$$\boldsymbol{H_1} = H_1\hat{\boldsymbol{x}'} \quad (3.3)$$

We also know from the knowledge of analytical geometry that

$$\frac{d\boldsymbol{\mu}}{dt} = \frac{\partial\boldsymbol{\mu}}{\partial t} + \boldsymbol{\omega} \times \boldsymbol{\mu} \quad (3.4)$$

Substituting Eq. (3.3) and Eq. (3.4) into Eq. (3.2) to obtain

$$\frac{\partial\boldsymbol{\mu}}{\partial t} = \frac{d\boldsymbol{\mu}}{dt} - \boldsymbol{\omega} \times \boldsymbol{\mu} = \boldsymbol{\mu} \times \gamma[\boldsymbol{H_0} + \boldsymbol{H_1}(t)] - \boldsymbol{\omega} \times \boldsymbol{\mu} = \boldsymbol{\mu} \times \gamma\left[H_0\hat{\boldsymbol{z}} + H_1\hat{\boldsymbol{x}'}\right] + \boldsymbol{\mu} \times \boldsymbol{\omega}$$

$$= \boldsymbol{\mu} \times \left[(\omega_z + \gamma H_0)\hat{\boldsymbol{z}} + \gamma H_1\hat{\boldsymbol{x}'}\right] \quad (3.5)$$

By convention, we define $\omega = -\omega_z$ and rewrite EQ.(3.5) as

$$\frac{\partial \boldsymbol{\mu}}{\partial t} = \boldsymbol{\mu} \times \gamma \left[\left(H_0 - \frac{\omega}{\gamma} \right) \hat{\boldsymbol{z}} + H_1 \widehat{\boldsymbol{x}'} \right] = \boldsymbol{\mu} \times \boldsymbol{H_{eff}} \quad (3.6)$$

where

$$\boldsymbol{H_{eff}} = \left(H_0 - \frac{\omega}{\gamma} \right) \hat{\boldsymbol{z}} + H_1 \widehat{\boldsymbol{x}'}$$

Physically Eq. (3.6) means in the rotating reference frame, the spin moment act as if in a static magnetic field $\boldsymbol{H_{eff}}$. When the resonance condition is satisfied, $\omega = \gamma H_0$, and the effective field in the rotating frame is just an "H_1" field in the x'-direction, and the spin would proceed about the $\mathbf{H_1}$ direction.

3.2 The behavior of nuclei in a solid and the detection of NMR spectrum

In real world, it is usually not possible to isolate a single nucleus for research. A common studying area is the behavior of an ensemble of nuclei with a certain lattice structure, for example, a solid.

Recall Fig 29 and the Zeeman splitting. If we have an ensemble of nuclei with the same total spin S in an external field $\mathbf{H_0}$, and each could occupy one of the (2S+1) energy levels. In equilibrium, the population on each energy level is determined by the Boltzmann relation

$$N_m \propto e^{-E_m/k_B T}$$

where k_B is the Boltzmann constant, and T is the temperature.

When an electromagnetic pulse at the resonant frequency is applied to the system, every spin of the system, except those already in the highest level absorbs the energy of a photon and jump to a higher energy level, which causes an imbalance of the system. After the effect of the pulse, the spin system needs to go back to its equilibrium state, which requires the exchange of energy. The channels of energy exchange can be various, for example the interaction between nuclei, the interaction between nuclei and nearby electrons, and the interaction between nuclei and the lattice. We call this process relaxation.

In the classical picture, let's consider the case discussed in the last section, which is when the effective field in always on the x'-direction of the rotating frame. As shown in Fig 31, a spin that is originally parallel to z-direction would rotate about x-axis, and after the effect of the pulse, the spin makes some angle θ with the z-direction, and it now possess both z-component and a component in the xy plane. Both components will decay after the pulse, and the time dependence of the spin magnetization follow the Bloch's equations [31].

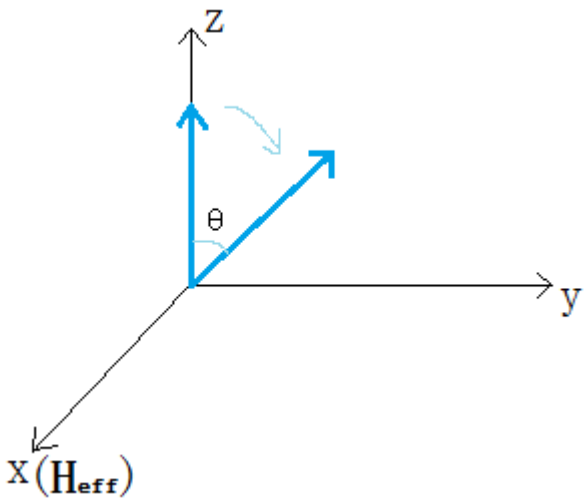

Figure 31. Illustration of a nuclear spin being tilted by an H_1-field.

$$\frac{dM_z}{dt} = -\gamma M_y H_1 + \frac{M_0 - M_z}{T_1} \quad (3.7a)$$

$$\frac{dM_x}{dt} = \gamma M_y h_0 - \frac{M_x}{T_2} \quad (3.7b)$$

$$\frac{dM_y}{dt} = \gamma (M_z H_1 - M_x h_0) - \frac{M_y}{T_2} \quad (3.7c)$$

In these equations, $h_0 = H_0 + \omega_z/\gamma$.

We can immediately notice that these equations imply that the relaxation time of M_z, which is T_1, is different from the relaxation time of the in-plane components, which is T_2. Usually we call T_1 the spin-lattice relaxation time, which is the characteristic time for the energy exchange between nuclei and the lattice, which can be taken as an energy reservoir. On the other hand, the decay of the transverse components conserves energy, and there is no need of an energy transfer to a reservoir. One possible mechanism for the T_2 process in a solid is that each nucleus spin produce a field to the nearby nuclei, which could either add or oppose the external field. As a result, each nucleus has a

different precession rate. If at time t=0, all the nuclei are in phase, then after a certain time τ, they would get out of step, and the averaged magnetization is thus reduced.

If we solve the Bloch' Equations, we can obtain

$$M_X(t) = (\chi' cos\omega t + \chi'' sin\omega t) H_{X0} \quad (3.8)$$

with

$$\chi' = \frac{\chi_0}{2}\omega_0 T_2 \frac{(\omega - \omega_0)T_2}{1 + (\omega - \omega_0)^2 T_2^2} \quad (3.8a)$$

$$\chi'' = \frac{\chi_0}{2}\omega_0 T_2 \frac{1}{1 + (\omega - \omega_0)^2 T_2^2} \quad (3.8b)$$

χ' and χ'' represent the real and imaginary parts of the NMR spectrum in the frequency space, and they both have the form of Lorentzian Function. In real experiment, this NMR spectrum in the frequency regime is what we look for.

In the classical picture, one obvious way of obtaining the spectra is that we apply a pulsed H_1 field to the nuclear system, which tilts the nuclear spin exactly to the xy-plane. In other words, the pulse makes the nuclei rotate by 90 degrees, and we call this pulse the π/2 pulse (or 90 ̊pulse). Then we can measure the induced magnetization in the xy-plane with a detection coil. This method is called a Free Induction Decay (FID) detection, which is both simple and straightforward.

However, as we mentioned before, different nuclei feel different local fields, and thus they proceed in different rates. If we just send aπ/2 pulse (with H1 field along +x-direction) to the system, what we should expect in the rotating reference frame is that

right after the$\pi/2$ pulse (t=0), all the nuclear spins are knocked to the xy-plane (Fig 32a). Specifically, the +y-direction. Since the pulse has finished, the spins start proceed about the z-axis in the laboratory frame. After a certain time t_0 ($t_0<T_2$), the spins "fan out" (Fig 32b) because of the different procession rate. In the rotating frame, we can see a distribution of spins in the xy-plane. Now imagine at time $t=t_0$ we apply another pulse with double duration and assume the H_1 field is +y-direction (Fig 32c). This is called a π pulse, and since it has twice the length of the $\pi/2$ pulse, it rotates the spin about y-axis by 180 degrees. In the rotating frame, it results in that the spins in the front of the fan now fall behind, and the spins at the back of the fan now lead (Fig 32d). Then after another time t_0, all the nuclear spins will collapse to the +y-direction (Fig 32e). This phenomenon is called the spin echo, and it is first discovered by Erwin Hahn [32].

There are many advantages related to using a spin echo rather a FID. For example, the FID signal reflects an inhomogeneous effect from the distribution of local fields and thus create much uncertainty in calculating the NMR shift. On the other hand, the spin echo effectively reduce the inhomogeneity and provide a more accurate measure of the shift. Moreover, in actual experimental work, there is usually a dead time right after the applied pulse, during which the data are meaningless. An FID signal starts right after the pulse, so it is surely affected by the dead time. In contrast, when we use spin echo, the signal is pushed further away from the pulses (see Fig 33), and therefore the dead time effect is eliminated.

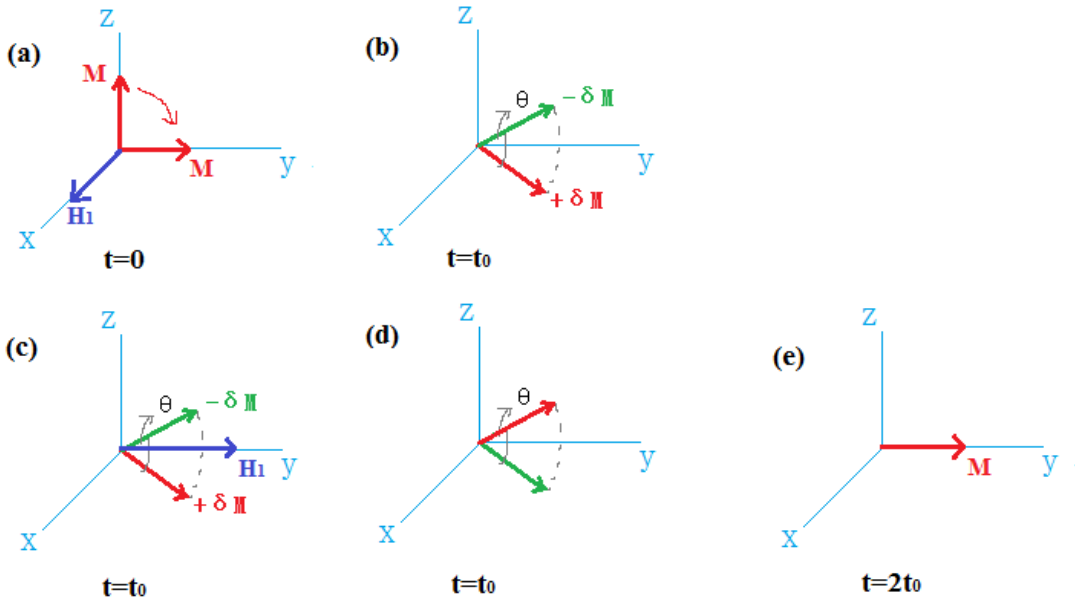

Figure 32 Illustration of spin echo sequence. (a) A pi/2 pulse knocks the spin to y-axis. (b) The transverse components of nuclear spins fan out in the xy-plane. (c) Applying a pi pulse along y-axis to the nuclear spin system. (d) The spins are flipped by 180° around the y-axis. (e) The transverse components refocus to y-axis again and forms an echo.

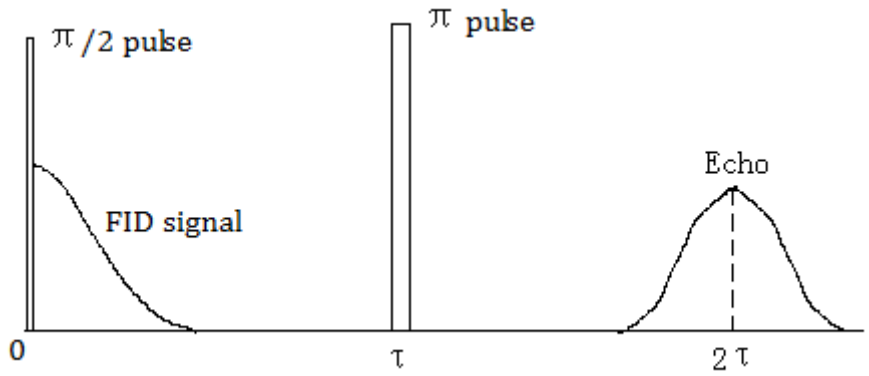

Figure 33 Illustration of spin echo sequence.

3.3 The quadrupolar interaction term and the satellites

The interactions a nuclear spin experiences in a solid can be summarized as the following Hamiltonian

$$\mathcal{H} = \mathcal{H}_z + \mathcal{H}_Q + \mathcal{H}_{n-n} + \mathcal{H}_{e-n} \quad (3.9)$$

The first term is the Zeeman term, and the second term is due to the electric quadrupole effects. The third and the fourth terms are the nucleus-nucleus interactions and the electron-nucleus interactions, which I will discuss in later sections. In this section, we will focus on the quadrupolar interaction.

The electric quadrupole interaction comes from the energy given by electric field felt by the nucleus. In our study ($Ba_3CoSb_2O_9$) as well as many other cases, we can write a simplified Hamiltonian with the assumption of a field with axial symmetry. If we consider the applied magnetic field to be in the z'-axis, which in general not the same as z-axis (the principle axis of the lattice structure), then the Hamiltonian including the Zeeman and Electric Quadrupolar interaction can be written as

$$\mathcal{H} = -\gamma_n \hbar H_0 I_{z'} + \frac{e^2 qQ}{4I(2I-1)}(3I_z^2 - I^2) \quad (3.10)$$

In this equation, e is the electron charge, and q is the nuclear charge. Q is called the Quadrupole moment, which is the property of the nucleus. The axes z, z', x, and x' are defined as shown in Fig 34.

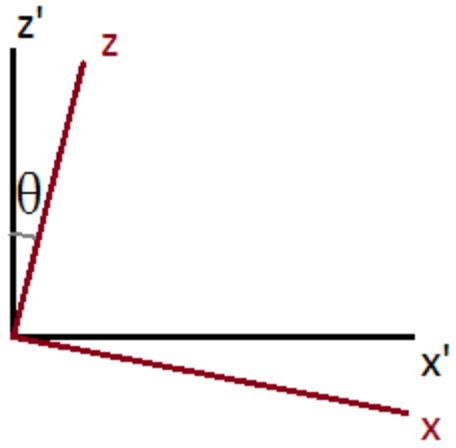

Figure 34 x'-axis lie in the plane containing z' and z.

It is easy to see that

$$I_z = I_{z'}cos\theta + I_{x'}sin\theta \quad (3.11)$$

Substituting Eq. (3.11) into Eq. (3.10) we obtain

$$\begin{aligned}\mathcal{H} = -\gamma_n \hbar H_0 I_{z'} \\ &+ \frac{e^2qQ}{4I(2I-1)}\left[3I_{z'}^2 cos^2\theta + 3I_{x'}^2 sin^2\theta\right. \\ &\left. + 3(I_{z'}I_{x'} + I_{x'}I_{z'})sin\theta cos\theta - I^2\right] \quad (3.12)\end{aligned}$$

Recall that we have axial symmetry, so the diagonal elements of $I_{x'}$ and $I_{y'}$ should be the same.

$$\begin{aligned}\langle m|I_{x'}^2|m\rangle &= \langle m|I_{y'}^2|m\rangle = \frac{1}{2}\langle m|I^2 - I_{z'}^2|m\rangle \\ &= \frac{1}{2}[I(I+1) - m^2] \quad (3.13)\end{aligned}$$

By expressing $I_{x'} = \frac{1}{2}(I'^{+} + I'^{-})$, it is obvious that $I_{x'}$ does not have diagonal elements. $I_{z'}$, on the other hand, is diagonal in the first order, so we have no

contribution from $(I_{z'}I_{x'} + I_{x'}I_{z'})$ in the first order. The energy levels can be then written as

$$E_m = -\gamma_n \hbar H_0 m + \frac{e^2 qQ}{4I(2I-1)}\left(\frac{3cos^2\theta - 1}{2}\right)[3m^2 - I(I+1)] \quad (3.14)$$

One thing we should notice from Eq. (3.14) is that m comes into the quadrupolar term in the quadratic form, so +m and –m energy levels have the same correction. For spin-3/2, which is the case of Ba nuclei, the shift of energy levels are shown in Fig 35a. Accidentally the magnitude of the shift is the same for all the energy levels in the first order, because $\left|\left[3\left(\frac{1}{2}\right)^2 - \frac{3}{2}\left(\frac{3}{2}+1\right)\right]\right| = \left|\left[3\left(\frac{3}{2}\right)^2 - \frac{3}{2}\left(\frac{3}{2}+1\right)\right]\right| = 3$. Now the energy differences between levels are different, and transitions between levels can be induced by photons of different energies, corresponding to different NMR frequencies. For spin-3/2, we would expect three NMR lines (satellites) (Fig 35b), and by convention we also call the middle one the central transition line.

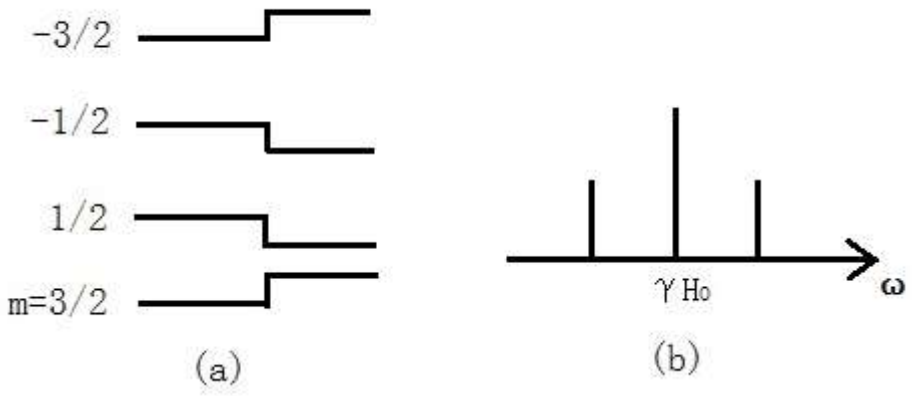

Figure 35 The energy levels of a 3/2 spin in a magnetic field are split by the electric field gradient.

If we looked at Eq. (3.14) further, we can easily notice that the transition between m=1/2 and m=-1/2 requires exactly the Zeeman energy $\gamma_n \hbar H_0$, but for other permitted transitions ($m \leftrightarrow m \pm 1$), the energy exchange is different from the Zeeman energy. If we consider the transition between m and (m-1), we can directly calculated from Eq. (3.14) that

$$\Delta E = \gamma_n \hbar H_0 + \frac{e^2 qQ}{4I(2I-1)}\left(\frac{3cos^2\theta - 1}{2}\right)(-6m + 3),$$

which is linearly related to quantum number m. So in principle we can define a quadrupole frequency υ_Q, which is the frequency distance between neighboring satellites. Take spn-3/2 as an example, we should expect 3 NMR signals at frequency $\upsilon_0 - \upsilon_Q\left(\frac{3cos^2\theta-1}{2}\right), \upsilon_0, and\ \upsilon_0 + \upsilon_Q\left(\frac{3cos^2\theta-1}{2}\right)$, respectively, where υ_0 is the Zeeman frequency.

3.4 The identification of NMR lines in $Ba_3CoSb_2O_9$

Our Nuclear Magnetic Resonance (NMR) measurements were conducted on a 30mg single crystal sample of $Ba_3CoSb_2O_9$, which was synthesized by H. D. Zhou et al using the traveling-solvent floating-zone method [17]. The dimension of the sample is approximately $4mm^2 \times 1.2mm$ thickness. A picture of the sample is shown in Fig 36.

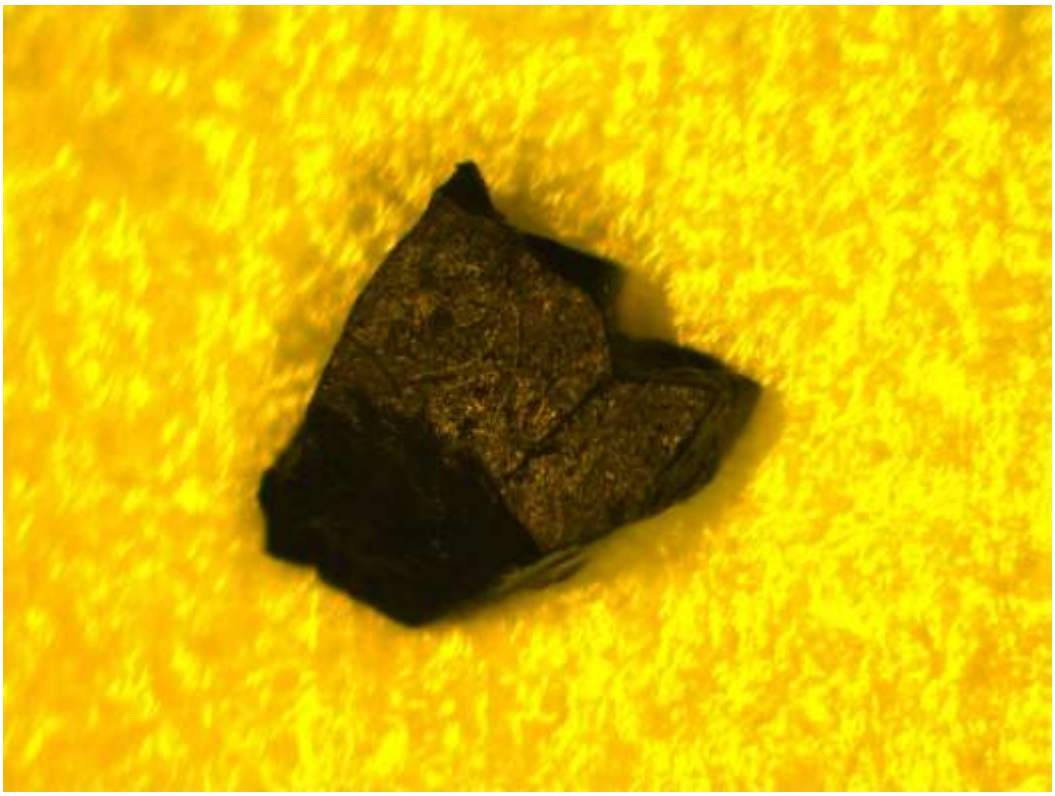

Figure 36 A picture of the $Ba_3CoSb_2O_9$ single crystal sample

The experiments took place in two laboratories. All the measurements under fields below 12T were done in the Department of Physics, UCLA, and measurements under higher field (13.5T-30.4T) were in the National High Magnetic Field Lab (NHMFL) in Tallahassee, FL.

The sample sits inside an NMR coil, which was mounted on a single axis piezo-driven rotator (Attocube ANRv51/RES). The relative rotation angle was determined by a resistive sensor built into the rotator. The absolute value of the angles was obtained by observing the variation of the NMR frequencies, which I will discuss in detail later.

Now we should review the lattice structure of $Ba_3CoSb_2O_9$. There are two different Ba sites in the compound- Ba(1) and Ba(2), and the number of Ba(2) sites is twice as many as Ba(1) sites. There are two Ba isotopes available for NMR detection, ^{135}Ba and ^{137}Ba, both with spin-3/2. The other Ba isotopes are either not stable or have a zero spin. The natural abundance of ^{135}Ba and ^{137}Ba are 6.59% and 11.32%, respectively. In summary, there are in total 4 different Ba nuclei to study, and it is easy to work out the relative intensity of NMR signals (take the intensity of $^{135}Ba(1)$ as 1).

Nuclei	$^{137}Ba(2)$	$^{137}Ba(1)$	$^{135}Ba(2)$	$^{135}Ba(1)$
Relative intensity	3.4	1.7	2	1

Since Ba nuclei is of spin-3/2, the electric quadrupolar effect splits its NMR signal into three lines- one central line and two satellites. This means we should expect 12 NMR lines in total for Ba nuclei. The Co and Sb nuclei also have non-zero spin, but we did not see their NMR signal. Possible reasons could be too fast spin-lattice relaxation rate (Co) and too broad and thus too weak signals (Sb).

As the first step of the experiment, we did frequency sweep measurements and sum up the Fourier transform of the signal to get the spectra. The measurements were done under field B=8.4524T and temperature T=6K, where according to the phase

diagram by H. D. Zhou [17] the sample is in the paramagnetic state. The results for both B//ab (field in plane) and B//c (field out of plane) are shown in Fig 37.

In determining the NMR lines, we considered the Zeeman frequency ($\omega_0 = \gamma H_0$) relative intensities of different Ba signals, and the fact that the two satellites should be roughly symmetric on each side of the central transition signal.

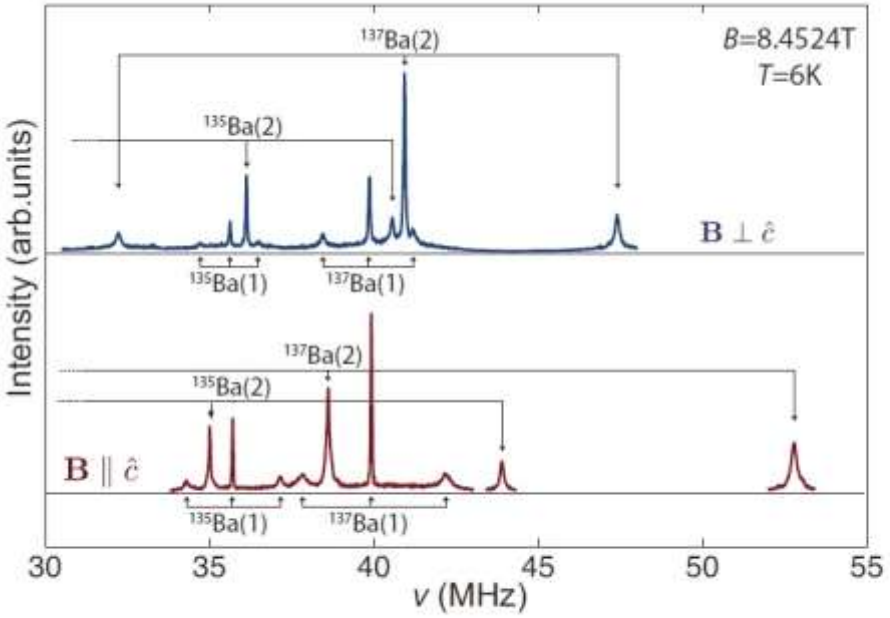

Figure 37 NMR spectra obtained by summing up the Fourier transform results of spin-echo signals at equally spaced frequencies. Different peaks are attributed to different Ba nuclei by considering the relative intensities and the frequency shift. The low frequency peaks were not measured due to the limitation of the tuning range of the RF circuit.

The reader may have noticed from Fig 37 that the relative positions of ^{137}Ba(1) and ^{137}Ba(2) central transition signals are different for B//ab and B//c. That is mainly because of the second order (in υ_Q) quadrupolar frequency, which is a correction to the Zeeman frequency. For spin-3/2, which is the case of ^{137}Ba and ^{135}Ba, the second order correction can be written as

$$\upsilon_{2nd} = \frac{3\upsilon_Q^2}{16\gamma B}(1 - cos^2\theta)(1 - 9cos^2\theta) \quad (3.15)$$

In this equation, υ_Q is the quadrupole frequency, γ is the gyromagnetic ratio, B is the external field, and θ is the angle between the external field the c axis of the crystal. Eq. (3.15) assumes that the principle axis is just the c-axis of the crystal. To better understand the angle dependence of the second order quadrupolar frequency, I graph the function $(1 - cos^2\theta)(1 - 9cos^2\theta)$ in Fig. 38. We should notice from Fig 38 that this function takes local maximum at 0 degree and 90 degrees, which corresponds to B//c and B//ab directions, respectively. This is important for the experiment, because it means we can accurately rotate the sample to B//c or B//ab direction by following the central transition signals of Ba nuclei and locate the sample where we have the local maximum of frequency.

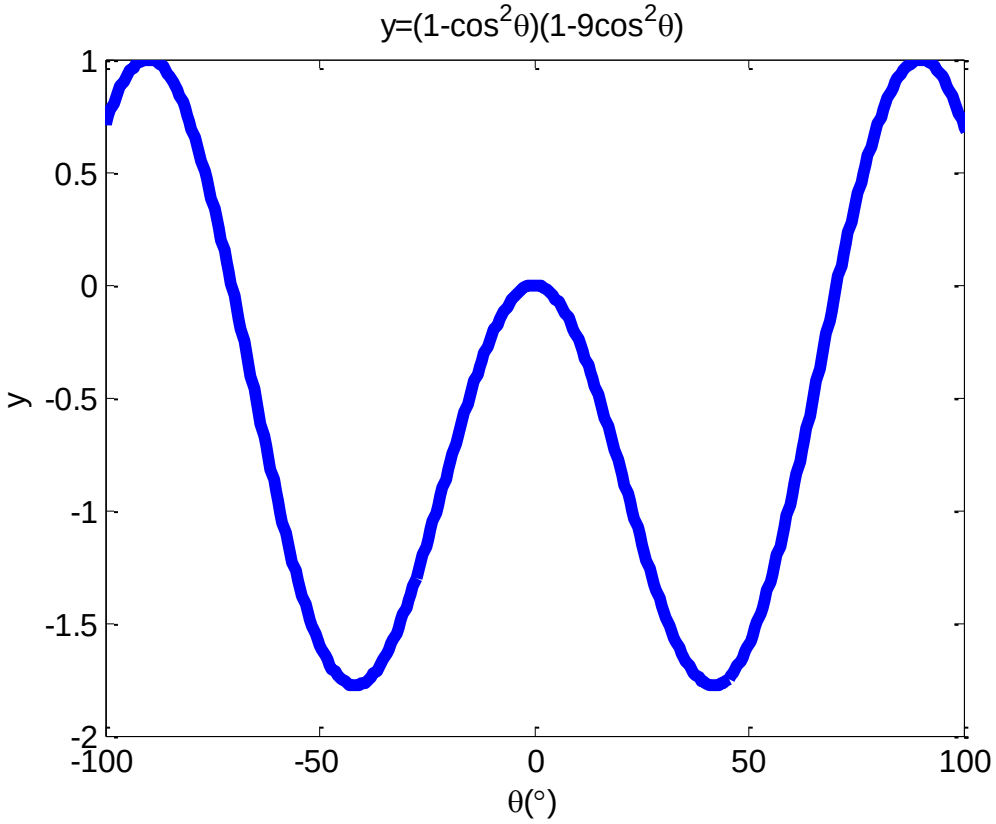

Figure 38 Functional shape of $(1 - cos^2\theta)(1 - 9cos^2\theta)$

As I mentioned before, the labeled orientation of the sample was problematic initially, so we need to identify the correct orientations by NMR experiments. One straightforward observation to make is the distance in frequency between satellites that belong to the same nucleus. For spin-3/2 nuclei, the frequency difference between the lowest-frequency satellite and the highest-frequency satellite is $|2\upsilon_Q\left(\frac{3cos^2\theta-1}{2}\right)|$. For B//c ($\theta = 0$), it is $2\upsilon_Q$, and for B//ab ($\theta = 90°$), the value is half (υ_Q). In Fig 37, if we look at the satellites of ^{137}Ba(2), which has the strongest signal and the largest υ_Q, we can easily see that the distance between two satellites is only half for B//ab, compared to B//c direction. Which is an obvious evidence of

the orientation. The quadrupolar frequencies v_Q for different nuclei then can be taken by reading the distance between satellites of the corresponding nuclei.

To further verify the orientation and for completeness of an NMR study, we did a rotation study on ^{137}Ba(2) central transition and graphed the central transition frequency as a function of angle from c-axis. Theoretically, the angle variation should conform to

$$v = \gamma B(1 + K_\alpha sin^2\theta + K_c cos^2\theta) + \frac{3v_Q^2}{16\gamma B}(1 - cos^2\theta)(1 - 9cos^2\theta) \quad (3.16)$$

where K_α and K_c are shifts from the Zeeman frequency, which were determined by the local maxima positions.

The results are shown in Fig 39

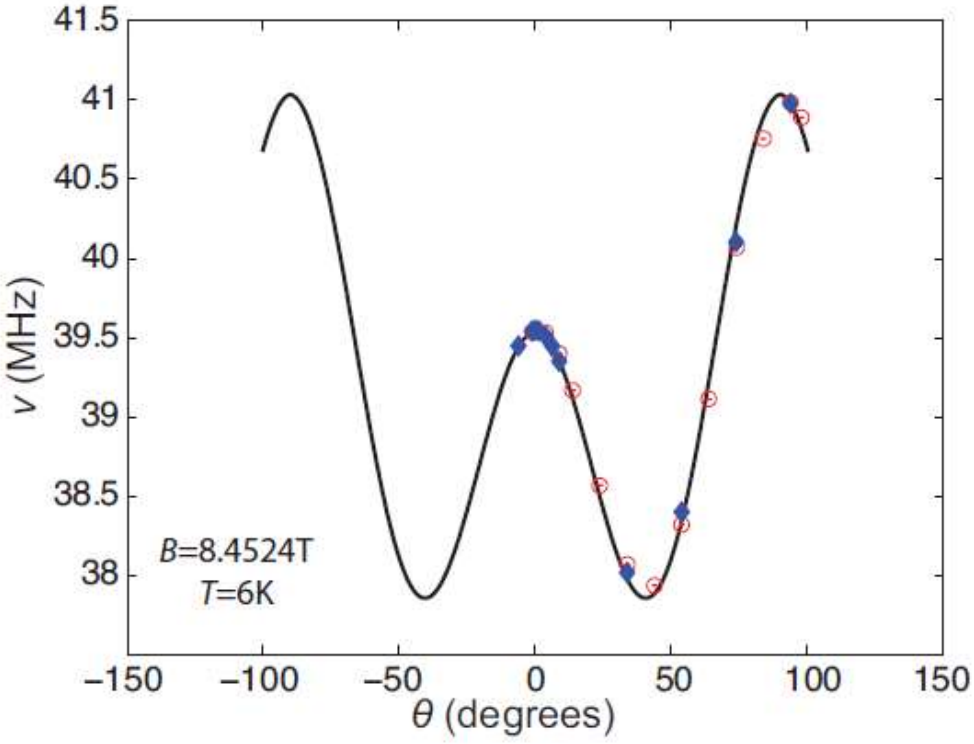

Figure 39 NMR frequency of the ^{137}Ba(2) central transition vs. θ for B=8.4524T and T=6K

We can see from Fig 39 that the experimental data (the blue and red points) agree with the theoretical curve (the black line) very well, which solidifies our interpretation of the sample orientations.

3.5 The NMR shift

Recall Eq. (3.9)

$$\mathcal{H} = \mathcal{H}_z + \mathcal{H}_Q + \mathcal{H}_{n-n} + \mathcal{H}_{e-n} \quad (3.9)$$

We have discussed the Zeeman term $\mathcal{H}_z$ and the quadrupole term $\mathcal{H}_Q$. The third term $\mathcal{H}_{n-n}$ is the interaction between nuclear spins, and it can be simply taken as

the interaction between the nuclear moment μ and the dipolar field created by the other nuclear spins in the lattice

$$\mathcal{H}_{n-n} = \frac{\mu_0}{4\pi}\sum_i \left[\frac{\boldsymbol{\mu}\cdot\boldsymbol{\mu_i}}{r_i^3} - \frac{3(\boldsymbol{\mu}\cdot\boldsymbol{r_i})(\boldsymbol{\mu_i}\cdot\boldsymbol{r_i})}{r_i^5}\right], \quad (3.17)$$

where $\boldsymbol{\mu_i}$ is the magnetic moment of a nuclear spin at displacement $\boldsymbol{r_i}$ from the moment μ, and the sum runs through the whole lattice. The nuclear magnetic moment is in the order of a nuclear magneton, which is $\mu_N = 5.05 \times 10^{-27} J/T$, and the magnetic moment of an electron is in the order of a Bohr magneton, which is $\mu_B = 9.27 \times 10^{-24} J/T$. We can see that the nuclear magnetic moment is 3 orders of magnitude smaller than the electron magnetic moment, so the magnetic dipolar interaction between nuclei is not important in shifting the NMR frequency. In our research, we basically ignored the $\mathcal{H}_{n-n}$ term in studying the NMR shift.

The last term in Eq. (3.9) $\mathcal{H}_{e-n}$ is often called the hyperfine interaction, which represents the coupling between the nuclear spin and the electron. This term is important because it reveals the state of electrons in a lattice, especially those near the nuclei, and it is the reason why NMR can serve as a local probe technique. By studying the hyperfine interaction, or the hyperfine shift of the NMR signal, we can identify the arrangement of electron spins in a lattice and detect the existence of magnetic orderings.

The hyperfine interaction can be summarized as

$$\mathcal{H}_{e-n} = \frac{\mu_0}{4\pi}\gamma_e\hbar\sum_i\left[-\frac{\boldsymbol{\mu}\cdot\boldsymbol{L_i}}{r_i^3}+\frac{\boldsymbol{\mu}\cdot\boldsymbol{S_i}}{r_i^3}-\frac{3(\boldsymbol{\mu}\cdot\boldsymbol{r_i})(\boldsymbol{S_i}\cdot\boldsymbol{r_i})}{r_i^5}-\frac{8\pi}{3}\boldsymbol{\mu}\cdot\boldsymbol{S_i}\delta(\boldsymbol{r_i})\right] \quad (3.18)$$

The first term in Eq. (3.18) is from the coupling of nuclear spin and the electron orbital angular momentum, and the shift caused by this orbital term is usually called the chemical shift. In most real materials, the expectation value of the orbital angular momentum $\boldsymbol{L_i}$ is zero under the crystal field, and that causes the quenching of the orbital term.

The second and the third term together is the magnetic dipolar interaction, which is caused by the magnetic dipolar field of an electron spin at the nuclear site. The fourth term is the Fermi contact term, which relates to the direct interaction of the nuclear dipole with the electron spin dipoles and is only non-zero if the electron wave function has a finite spin density a the position of the nucleus. This contact interaction can be divided into an isotropic part and an anisotropic part with an angle dependence$\sim\frac{3cos^2\theta-1}{2}$, where θ is the angle between the direction of the nuclear spin and the displacement vector starting from the electron to the position of the nucleus.

Taking into account of the NMR shift shown in Eq. (3.18), we can write the NMR central transition frequency as

$$\upsilon = \gamma B(1 + K_{\alpha}) + \frac{3\upsilon_Q^2}{16\gamma B}(1 - cos^2\theta)(1 - 9cos^2\theta), \quad (3.19)$$

where K_{α} is the hyperfine shift, and α denotes the two orientations (B//c or B//ab). A closer observation of Eq. (3.18) reveals that the direct dipolar interaction and the contact part are proportional to the electron spin susceptibility χ, while the orbital term is independent of χ. This means we can write the hyperfine shift K as a function of the electron spin susceptibility χ

$$K_{\alpha}(T) = K_{\alpha}^0 + A_{\alpha}\chi_{\alpha}(T), \quad (3.20)$$

In this equation, K_{α}^0 is the orbital shift, which is temperature-independent, and A_{α} is called the hyperfine constant. To determine the orbital shift and the hyperfine constant, we can measure the total shift K_{α} at some different temperatures, and find out the corresponding susceptibility at the same temperatures. Then we can plot the results in a $K - \chi$ plot with T to be the implicit variable. In such a plot, the y-intercept is the orbital shift, and the slope is the hyperfine constant. We did this for ^{137}Ba(1) and ^{137}Ba(2) central transitions on both field orientations, and the resultant $K - \chi$ plots are shown in Fig 40.

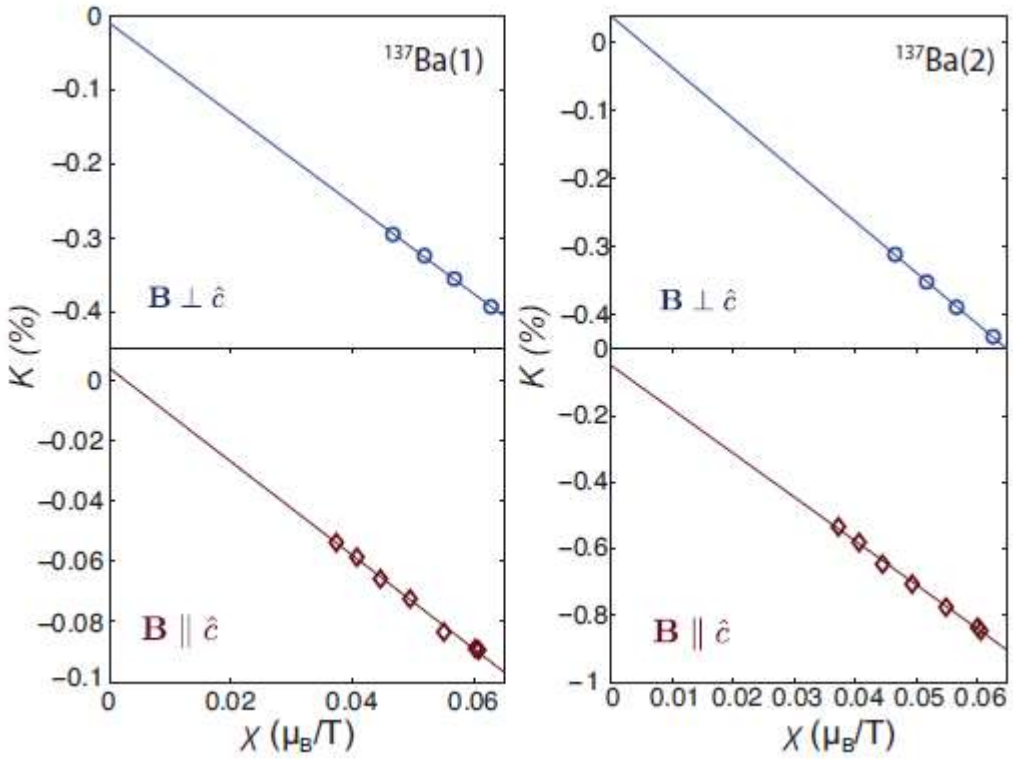

Figure 40 $K-\chi$ plots for both Ba sites at B=8.4524T. The temperature ranged from 10K to 50K.

From the fitting lines to the $K-\chi$ plot, we first notice that the orbital part (y-intercept) is almost zero, so we will assume the orbital part is negligible in further analysis. A summary of the hyperfine constants are shown in the following table

Nuclear site	ν_Q(MHz)	$A_{\parallel c}(\mathrm{G}/\mu_B)$	$A_{\perp c}(\mathrm{G}/\mu_B)$
^{137}Ba(1)	2.72	-156	-612
^{137}Ba(2)	15.4	-1313	-752
^{135}Ba(1)	1.75	-156	-612
^{135}Ba(2)	9.8	-1313	-752

Table II NMR parameters for the Ba nuclear sites/isotopes

The hyperfine environment for the same site with different Ba isotopes is exactly the same, so from now on, we do not consider the ^{135}Ba(1) and ^{135}Ba(2) nuclei, and in fact, our experiment focused on the central transitions of ^{137}Ba(1) and ^{137}Ba(2).

The total field at a Ba site can be written as $B = B_0 + B_{hf} + B_{macro}$, where B_0 is the applied external field, B_{hf} is the hyperfine field, and B_{macro} is macroscopic field. The macroscopic field includes the Lorentz field and the demagnetization field, which relates to the geometry of the sample. The sum of these two fields can be written as

$$B_{macro} = \frac{\mu_0}{3}\left(M - \frac{D}{4\pi}M\right), \quad (3.21)$$

where M is the bulk magnetization of the sample, and D is called the demagnetization factor, which takes value between 0 and 1. It is straightforward to see that the macroscopic field is proportional to the magnetization, and thus takes larger value at larger external field. In our experiment, the largest field reached was 30.4T, where B_{macro} is calculated to be around 40G, and that is smaller than the line width of the NMR signal. In other words, we can neglect this term in our analysis without affecting the identification of magnetic ordering.

Now we are in a position to step further in the analysis of the hyperfine constants. For ^{137}Ba(1), we can directly calculate the dipolar field by an electron at the nuclear site, using the equation:

$$B_{dip} = \sum_i \frac{\mu_0}{4\pi}\left(\frac{3\boldsymbol{r_i}(\boldsymbol{m_i}\cdot\boldsymbol{r_i})}{r_i^5} - \frac{\boldsymbol{m_i}}{r_i^3}\right), \quad (3.21)$$

where the sum is over all electron spins, and the magnitude of $\boldsymbol{m_i}$ is taken to be $1\mu_B$, so that the resultant A_{dip} is in the unit T/μ_B or G/μ_B. The sum in Eq. (3.21) actually does not converge, so in practice, we have to do the calculation within a finite size sphere. The result by choosing a 50a-radius (a is the lattice constant) sphere is $A_{dip}^{\parallel c} = 750G/\mu_B$, and $A_{dip}^{\perp c} = -375G/\mu_B$. Further expansion of the sphere only changes the results in the order of $1G/\mu_B$. Now we can write the following equations,

$$A_{Ba(1)}^{\parallel c} = A_{iso}^{\parallel c} + A_{aniso}^{\parallel c} + A_{dip}^{\parallel c} = -156G/\mu_B$$

$$A_{Ba(1)}^{\perp c} = A_{iso}^{\perp c} + A_{aniso}^{\perp c} + A_{dip}^{\perp c} = -612G/\mu_B$$

$$A_{aniso}^{\perp c} = -\frac{1}{2}A_{aniso}^{\parallel c}$$

$$A_{iso}^{\parallel c} = A_{iso}^{\perp c}$$

Solving these equations we obtain $A_{iso}^{\parallel c} = A_{iso}^{\perp c} = -460G/\mu_B$, $A_{aniso}^{\perp c} = 223G/\mu_B$, and $A_{aniso}^{\parallel c} = -446G/\mu_B$. In fact, the hyperfine constant is a tensor, which can by represented by a matrix $\mathbb{A}_{Ba(1)}$. For the analysis of ^{137}Ba(1), because the nucleus sits at a highly symmetric position, it is reasonable to assume the matrix is diagonal. Moreover, in the analysis of ^{137}Ba(1), we only consider the two nearest Co^{2+} electrons in adjacent layers. When calculating the hyperfine field using the hyperfine tensor, we have

$$\boldsymbol{B_{hf}} = \mathbb{A}_{Ba(1)} \cdot (\boldsymbol{S_o} + \boldsymbol{S_e}), \quad (3.22)$$

where $\boldsymbol{S_o}, \boldsymbol{S_e}$ are the spin magnetic moments for the odd layer electron and the even layer electron, respectively. Since there are two nearest neighbors, the

hyperfine constants should be divided by two, and the hyperfine tensor can be written as

$$\mathbb{A}_{Ba(1)} = \begin{pmatrix} -0.0306 & 0 & 0 \\ 0 & -0.0306 & 0 \\ 0 & 0 & -0.0078 \end{pmatrix} T/\mu_B$$

The reason we write up the hyperfine matrix is that once we have an assumption of the electron spin orientations, we can test it by calculating the hyperfine field using Eq. (3.22) and compare the result to the experimental data. This procedure would be essential in figuring out the magnetic ordering.

The hyperfine matrix for ^{137}Ba(2) is more complex than that of ^{137}Ba(1), because Ba(2) has three nearest neighbors and it is at a lower symmetry position. We can recall from the lattice structure that Ba(2) is above the triangular layer by 0.0888c, where $c = 14.4283\text{Å}$ is the lattice constant. The projection of Ba(2) into the triangular plane is right in the middle of a triangle. Our coordinate system is shown in Fig 41, with the origin in the middle of the triangle, and the three nearest Co^{2+} electron spins sit at each corner of the triangle.

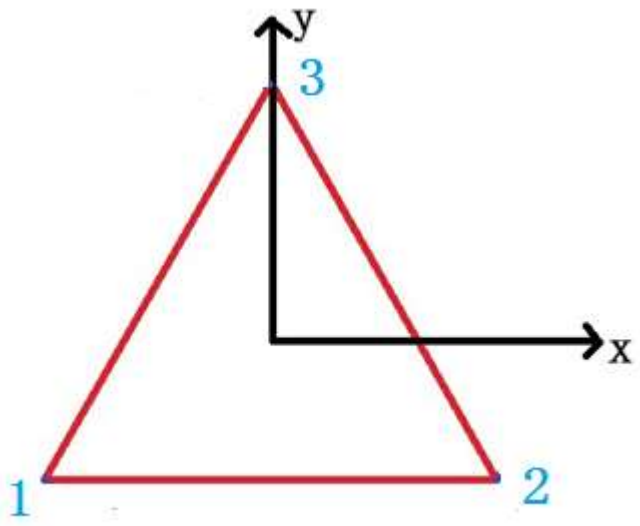

Figure 41 The coordinate system and the positions of the three nearest electrons.

We first notice that within an error of 5%, the hyperfine constants of ^{137}Ba(2) can be divided simply to the isotropic contact part and the direct dipolar part, and the contact part has the value

$$A_{Ba(2)}^{iso} = (-952 \pm 33)G/\mu_B$$

In the matrix form, we can write it as a diagonal matrix

$$\mathbb{A}_{iso} = \begin{pmatrix} -952 & 0 & 0 \\ 0 & -952 & 0 \\ 0 & 0 & -952 \end{pmatrix} \mathrm{G}/\mu_\mathrm{B}$$

The direct dipolar interaction can also be written in matrix form by looking at the geometry. In our calculation, we only consider the nearest neighbors. In the lattice structure, the Ba(2) is not in the triangular plane and its coordinates is $(0, 0, 0.0888c)$. The coordinates of the three electrons are

$$\left(-\frac{1}{2}\mathrm{a}, -\frac{\sqrt{3}}{6}\mathrm{a}, 0\right),$$

$$\left(\frac{1}{2}\mathrm{a}, -\frac{\sqrt{3}}{6}\mathrm{a}, 0\right),$$

$$\left(0, \frac{\sqrt{3}}{3}\mathrm{a}, 0\right),$$

The field by a magnetic dipole is $\mathrm{B} = \frac{\mu_0}{4\pi}\frac{3\mathbf{r}(\mathbf{m}\cdot\mathbf{r})}{\mathrm{r}^5} - \frac{\mathbf{m}}{\mathrm{r}^3}$, where $\mathbf{m}$ is the magnetic moment. The hyperfine matrix related to the dipolar interaction has the following form,

$$\mathbb{A}_{dip} = \frac{\mu_0}{4\pi}\frac{1}{\mathrm{r}^3}\begin{pmatrix} 3\mathrm{r_x^2} - 1 & 3\mathrm{r_x r_y} & 3\mathrm{r_x r_z} \\ 3\mathrm{r_x r_y} & 3\mathrm{r_y^2} - 1 & 3\mathrm{r_y r_z} \\ 3\mathrm{r_x r_z} & 3\mathrm{r_y r_z} & 3\mathrm{r_z^2} - 1 \end{pmatrix}, \quad (3.23)$$

where $\mathrm{r_x}$, $\mathrm{r_y}$, and $\mathrm{r_z}$ are the three normalized components ($r_x^2 + r_y^2 + r_z^2 = 1$) of the displacement vector pointing from the electron to the nuclei, and r is the magnitude of that displacement vector. For the three nearest electron spins of ^{137}Ba(2), the displacement vectors are obtained by direct calculation.

$$\boldsymbol{r_1} = \left(\frac{1}{2}a, \quad \frac{\sqrt{3}}{6}a, \quad 0.0888c\right)$$

$$\boldsymbol{r_2} = \left(-\frac{1}{2}a, \quad \frac{\sqrt{3}}{6}a, \quad 0.0888c\right)$$

$$\boldsymbol{r_3} = \left(0, \quad -\frac{\sqrt{3}}{3}a, \quad 0.0888c\right)$$

The lattice constants a=5.8413Å, c=14.4283Å are used in these expressions.

Next we can calculate the dipolar interaction matrices for each electron spin and the results are

$$\mathbb{A}^{\mathbf{1}}{}_{\mathrm{dip}} = \frac{\mu_0}{4\pi}\frac{1}{\mathrm{r}^3}\begin{pmatrix} 0.9662 & 1.1352 & 0.8625 \\ 1.1352 & -0.3446 & 0.4980 \\ 0.8625 & 0.4980 & -0.6216 \end{pmatrix} \quad (3.23a)$$

$$\mathbb{A}^{\mathbf{2}}{}_{\mathrm{dip}} = \frac{\mu_0}{4\pi}\frac{1}{\mathrm{r}^3}\begin{pmatrix} 0.9662 & -1.1352 & -0.8625 \\ -1.1352 & -0.3446 & 0.4980 \\ -0.8625 & 0.4980 & -0.6216 \end{pmatrix} \quad (3.23b)$$

$$\mathbb{A}^{\mathbf{3}}{}_{\mathrm{dip}} = \frac{\mu_0}{4\pi}\frac{1}{\mathrm{r}^3}\begin{pmatrix} -1 & 0 & 0 \\ 0 & 1.6216 & -0.9960 \\ 0 & -0.9960 & -0.6216 \end{pmatrix}, \quad (3.23c)$$

where

$$\frac{\mu_0}{4\pi}\frac{1}{\mathrm{r}^3} = 198\mathrm{G}/\mu_{\mathrm{B}}$$

As a verification of the results, let us calculate the total hyperfine coupling matrix in the paramagnetic states, when all the electron spins are in the

$$\overleftrightarrow{\mathrm{A}} = \overleftrightarrow{\mathrm{A}^1{}_{\mathrm{dip}}} + \overleftrightarrow{\mathrm{A}^2{}_{\mathrm{dip}}} + \overleftrightarrow{\mathrm{A}^3{}_{\mathrm{dip}}} + \overleftrightarrow{\mathrm{A}}_{\mathrm{iso}} = \begin{pmatrix} -767 & 0 & 0 \\ 0 & -767 & -394 \\ 0 & -394 & -1321 \end{pmatrix}\mathrm{G}/\mu_{\mathrm{B}}$$

We can realize that the diagonal elements are simply the hyperfine constants for B//ab and B//c directions.

When not in the paramagnetic states, the calculation of hyperfine field is different because the electron spins may point to different directions. A general way of calculating would be

$$B_{loc} = \sum_{i}^{3} \mathbb{A}^{\boldsymbol{i}}{}_{\mathrm{dip}} \cdot \boldsymbol{m_i} + \mathbb{A}_{\mathrm{iso}} \cdot \frac{1}{3}\sum_{1}^{3} \boldsymbol{m_i}, \quad (3.24)$$

where $\boldsymbol{m_i}$ is the magnetic spin moment at position i.

Chapter 4

NMR spectra in the magnetic state

In $Ba_3CoSb_2O_9$, the susceptibility and specific heat measurements clearly show phase transitions into antiferromagnetic state [17] [18]. The theoretical phase diagram proposes various magnetic ordering at different fields and temperatures [11]. The neutron scattering experiment group [18] even claimed the ground state magnetic ordering at zero field. However, we are the first group that actually explored the phase diagram in a vast range of field and temperature to figure out the magnetic order and the evolution of electron spin orientations on this quasi-2D triangular lattice.

In this chapter, we will repeatedly refer to the different magnetic orderings, so it is convenient to have them clearly labeled at the start of this chapter. The discussion may include 9 possible magnetic states, and all of them are graphed in Fig. 42.

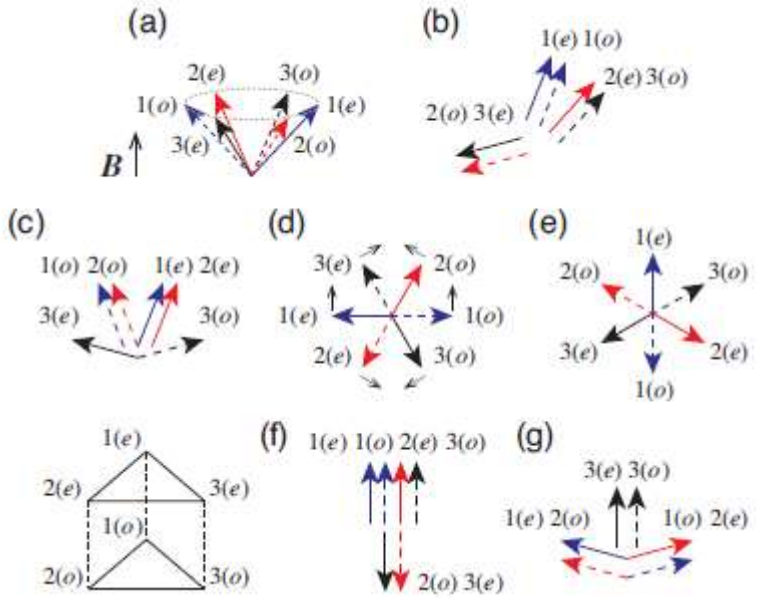

Figure 42 Magnetic states in 3D with a 6-sublattice structure

4.1 The spectrum in the up-up-down state

The up-up-down (uud) state (Fig. 42f) is the most interesting part of the study of triangular lattice antiferromagnetic state. This state is featured by the spin configuration that among the 6 sublattices, four spins point parallel to the field, and two spins point antiparallel to the field, and very importantly, this configuration is stable for a finite range of field. In other words, within a certain range of field, the spin configuration of the lattice is field-independent, and we ought to see the signature of that in the NMR spectrum.

In the uud phase, the Ba(1) site splits into two different magnetic environment, As shown in Fig 43.

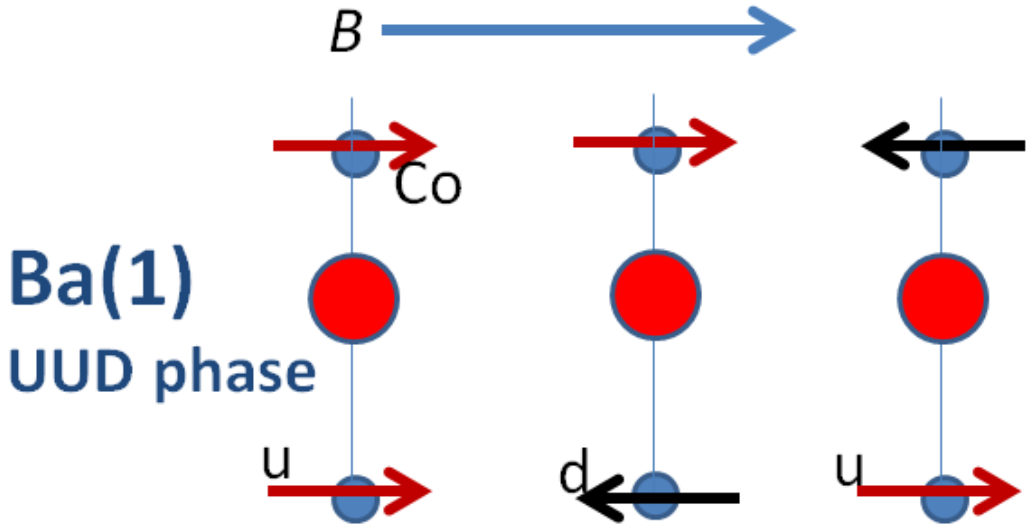

Figure 43 Ba(1) sites in the uud state. The field is parallel to the triangular plane. There are two types of local environment for Ba(1), one seeing two nearest electron spins both parallel to the field, the other seeing two nearest spins antiparallel to each other. The population of these two different Ba(1) sites has the ratio of 1:2, and thus split the Ba(1) line into two parts.

The previous research has proved that the uud phase only happens when the external field is parallel to the triangular plane [22], so the directions of the electron spins are perpendicular to the c-axis of the lattice. One portion of the Ba(1) sites sees two nearest electron spins both parallel to the field, while the other Ba(1) sites have one neighbor parallel and one antiparallel to the field. The ratio of the two Ba(1) sites is 1:2, which makes the total number of "up spin" twice as many as the "down spin". To calculate the hyperfine field at the Ba(1) site, we use $B_{Ba(1)}^{hf} = \overleftrightarrow{\mathbb{A}}_{Ba(1)} \cdot (\boldsymbol{m_e} + \boldsymbol{m_o})$, where $\boldsymbol{m_e}$ and $\boldsymbol{m_o}$ are the magnetic moments of the even

and odd layer spins, respectively. In the uud state, the magnetic moment is simply $\boldsymbol{m_i}(i = e, o) = (\pm m_0, 0, 0)$, where $m_0 = 1.92\mu_B$ is the full moment of Co^{2+} [22], the "+" sign means parallel, and the the "-" sign means antiparallel to the field. Now it is clear that the hyperfine fields are different for the two types of Ba(1) sites. The one with two spins pointing to opposite directions should have basically zero hyperfine field, while the one with two parallel spins should have a negative hyperfine field due to the negative hyperfine constants. Consequently, the Ba(1) NMR spectrum should split into two lines, and the line splitting should be constant in the uud state.

Experimentally, we did a field-dependent spectra study and a temperature-dependent spectra study, as shown in Fig 44.

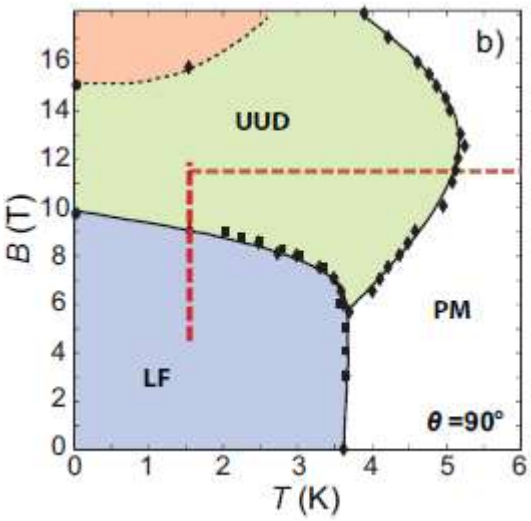

Figure 44 Part of the phase diagram for B//ab direction. The red lines show the range we covered in experiment.

The field dependent measurements (the vertical line) was done in about 1.55K, which is the base temperature of the our cryostat, starting from 4.5T, which is in a low-field phase, and ending at 11.9T, which is the highest field we can reach in UCLA. The temperature dependent measurements (the horizontal line) was at 11.5T, starting from 6K, which is in the paramagnetic state, and ending at 1.55K, which is in the uud state.

The field-dependent NMR spectra are shown in Fig 45. The relative frequency $\Delta\upsilon$ is defined as $\Delta\upsilon = \upsilon - \gamma B_0 - \frac{3\upsilon_Q^2}{16\gamma B_0}$, where υ is the actual frequency, $\gamma = 4.732\mathrm{MHz/T}$ is the gyromagnetic ratio for ^{137}Ba, and $\frac{3\upsilon_Q^2}{16\gamma B_0}$ is the second order quadrupole frequency. In fact, after the subtraction of Zeeman frequency and the second order quadrupole frequency, what is left should be the hyperfine frequency, so $\Delta\upsilon = \gamma B_{hf}$.

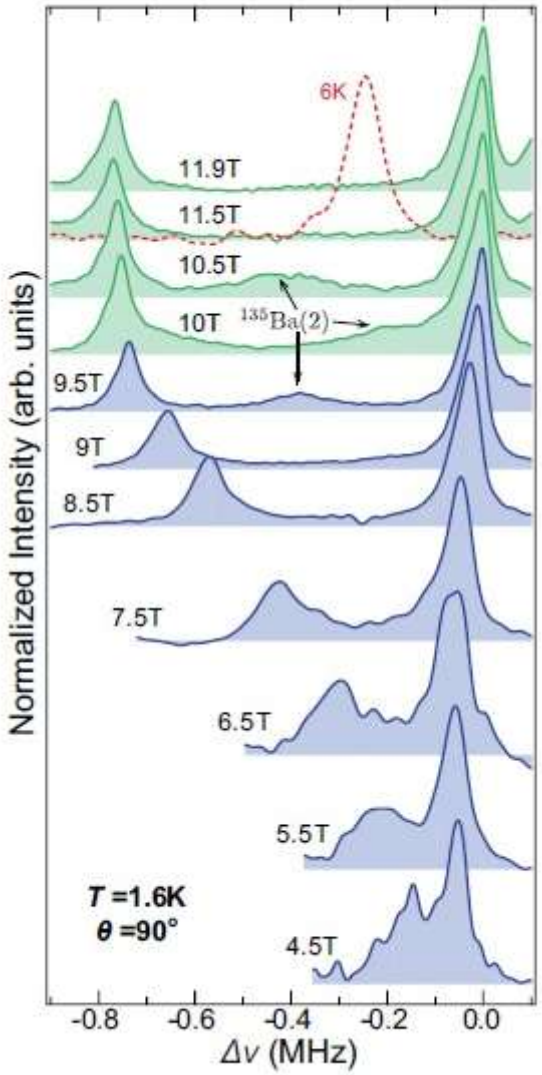

Figure 45 NMR spectra at 1.6K, B//ab, ^{137}Ba(1). The red dotted line is where the signal is in the paramagnetic state.

We first observe that in the uud state (B=10T, 10.5T, 11.5T, and 11.9T), we have two NMR lines for Ba(1), and the intensity ratio is 1:2, which is consistent with the prediction of uud phase. The peak with higher intensity is at almost zero hyperfine frequency position, which is theoretically correct for the Ba(1) site that has two nearest spins facing opposite directions. The splitting between the two

peaks is small at 4.5T, and it obviously opens up as the field increasing. However, starting from 10T, the line splitting barely changes as we further increase the field.

The line splitting in the uud phase is measured to be 760kHz, while the theoretical calculation using the measured hyperfine constant is 556kHz. The discrepancy here comes from the uncertainty of hyperfine constants. The way we obtain the hyperfine constant is fitting the data on a $K-\chi$ plot linearly and taking the slope of the fitting result as the hyperfine constant. This method is certainly not perfect since we only have 4 points. The line splitting in the uud state thus has an uncertainty because it is proportional to the hyperfine constant. To justify the consistency between theoretical calculation and the experimental results, I use the 760kHz line splitting to calculate the hyperfine constant, and take that result as the slope of a straight line, and then watch if this straight line fit the $K-\chi$ plot data in a reasonable way. The result is shown in Fig 46.

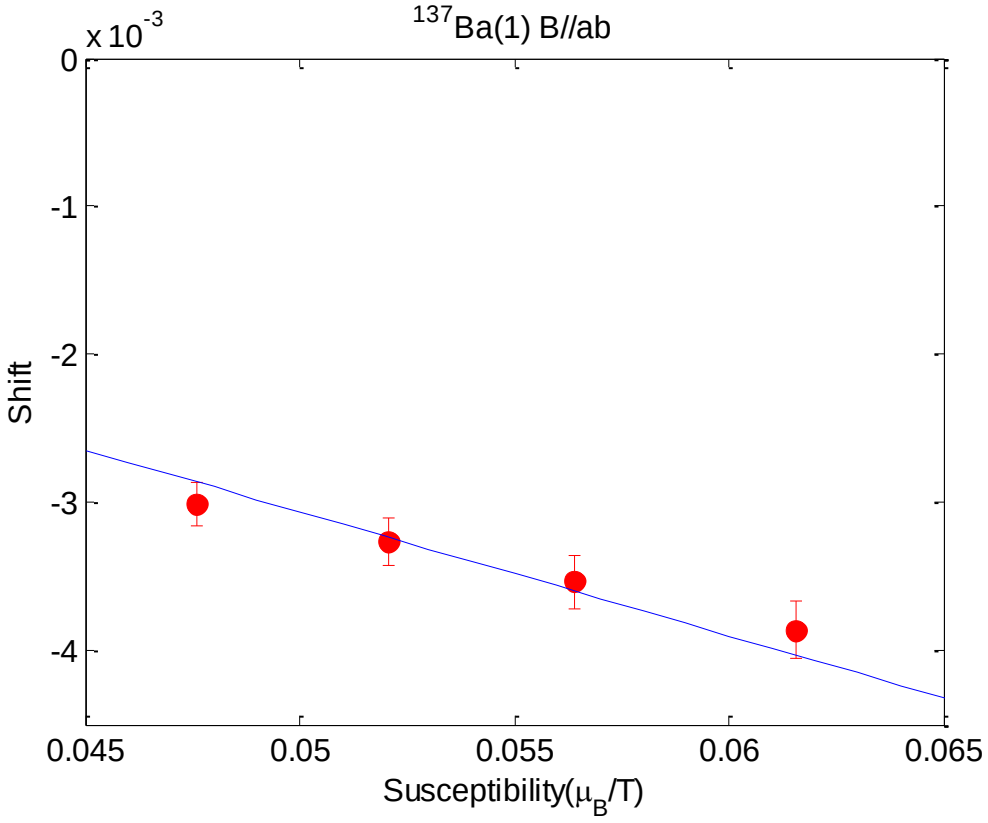

Figure 46 the $K-\chi$ plot for ^{137}Ba(1) with B//ab. The red points are experimental data points, and the blue line has the slope that derives the correct uud phase line splitting. The error bars on the red points are 5% uncertainties.

From Fig 46 we can see that when we assume a slope that gives the experimental line splitting in the uud state, the fitting to the hyperfine data is reasonable within a 5% uncertainty, so it is justified to say the uud state line splittings from the ^{137}Ba(1) NMR spectra agree with the theoretical calculation very well. We have also plotted the line splitting as a function of field (Fig 47), which shows clearly the existence of the plateau. Another thing we should notice from Fig 47 is that the transition from the low field phase to the uud phase is at about 10T, which is roughly 1/3 of the saturation field (31.9T from ref [22]).

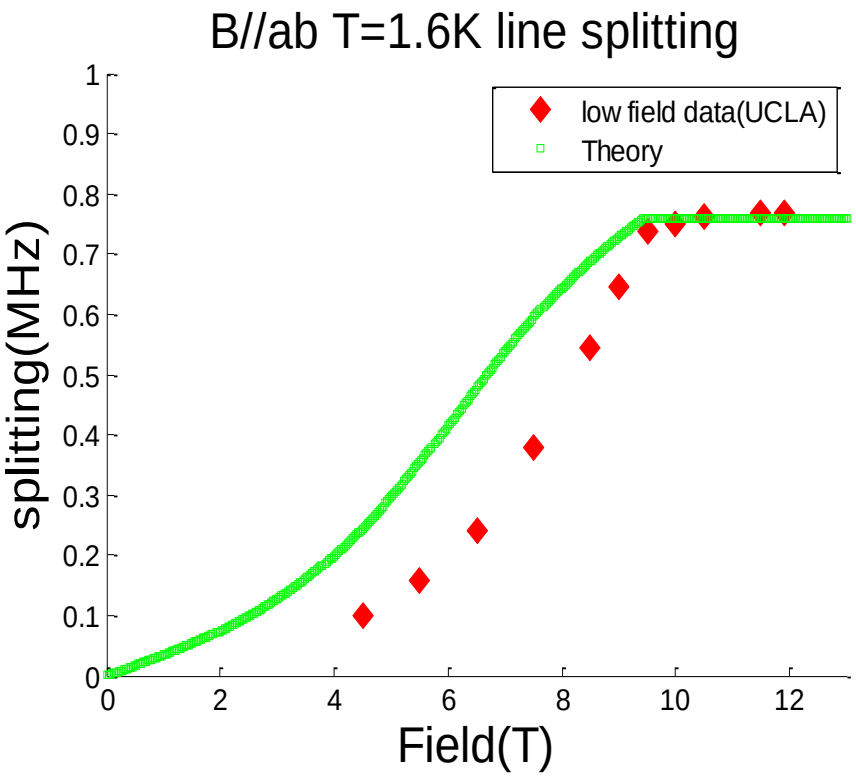

Figure 47 Line splitting of ^{137}Ba(1) as a function of field. The theoretical line (green) is normalized so that the uud phase splitting fits the experimental data. The red points are taken from the experimental data.

The line splitting of ^{137}Ba(1) can serve as a measure of the order parameter, and its temperature dependence as well as the relevant spectra are shown in Fig 48. These temperature dependent spectra were taken at 11.5T. As expected for the uud phase, the line splitting does not change much in the low temperature region. As we increasing the temperature, the ordered moment reduces sharply around the transition point.

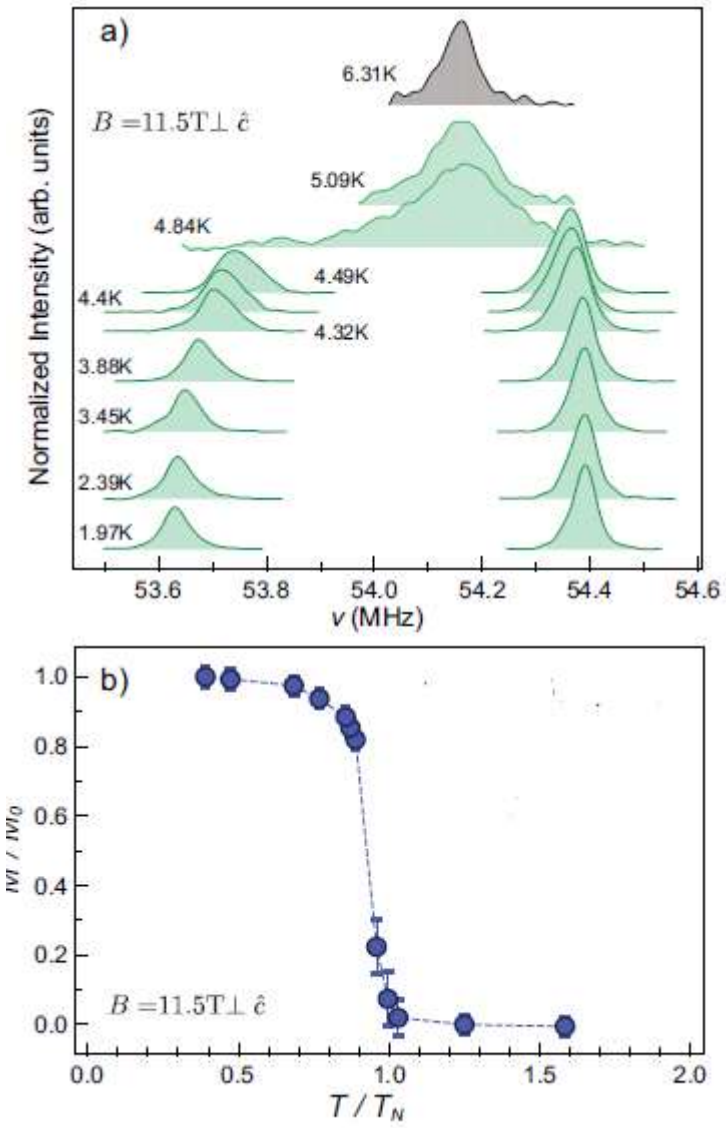

Figure 48 (a) NMR spectra of the ^{137}Ba(1) central transition for different temperatures at B=11.5T, B//ab. (b) Temperature dependence of the ordered moment amplitude in the uud phase.

The ^{137}Ba(1) spectra function as a solid evidence of the existence of the uud state when the field is parallel to the triangular plane. However, it leaves the field with an in-plane freedom, and we are not able to tell the in-plane orientation of the field just from the Ba(1) measurement. On the other hand, the theory about triangular

lattice antiferromagnet provides no indication about the in-plane field direction. To figure this out, we need to analyze the spectra of ^{137}Ba(2).

Recall Eq. (3.24) for the calculation of local field at the Ba(2) site,

$$B_{loc} = \sum_{i}^{3} \mathbb{A}^{\boldsymbol{i}}{}_{\text{dip}} \cdot \boldsymbol{m_i} + \mathbb{A}_{\text{iso}} \cdot \frac{1}{3} \sum_{1}^{3} \boldsymbol{m_i}, \quad (3.24)$$

The dipolar interaction tensor has off-diagonal elements, so the in-plane field direction is important in calculation. Assuming the angle between the field and the a-axis of the lattice to be θ, then an "up" spin has the coordinate representation $(m_0\cos\theta, m_0\sin\theta, 0)$, and the "down" spin is $-(m_0\cos\theta, m_0\sin\theta, 0)$. As an example of calculation, we assume there is a Ba(2) with "up" spin in position 1 and 2, and "down" spin in position 3, then the calculation of the local field should be

$$B_{loc} = \mathbb{A}^{\mathbf{1}}{}_{\text{dip}} \cdot \begin{pmatrix} m_0\cos\theta \\ m_0\sin\theta \\ 0 \end{pmatrix} + \mathbb{A}^{\mathbf{2}}{}_{\text{dip}} \cdot \begin{pmatrix} m_0\cos\theta \\ m_0\sin\theta \\ 0 \end{pmatrix} + \mathbb{A}^{\mathbf{3}}{}_{\text{dip}} \cdot \begin{pmatrix} -m_0\cos\theta \\ -m_0\sin\theta \\ 0 \end{pmatrix} + \mathbb{A}_{\text{iso}} \cdot \frac{1}{3} \begin{pmatrix} m_0\cos\theta \\ m_0\sin\theta \\ 0 \end{pmatrix}$$

The values of the matrices have been calculated in Eq. (3.23abc).

In the uud state, there are six possible different Ba(2) sites, distinguished by the spin orientation and the chirality of the three nearest neighbors, as shown in Fig 49.

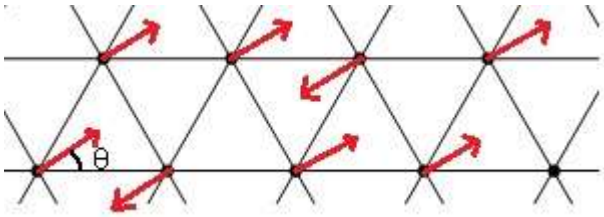

Figure 49 spin orientations in the uud state. Θ is the angle between the "up" spin and the a-axis of the lattice.

If we calculate the hyperfine field for each of the six Ba(2) sites and plot the result as a function of angle θ, we obtain Fig 50. We notice that there are three different local fields with equal intensity, and they all vary as a sine wave with different phases. In Fig 51a, we have the spectrum of ^{137}Ba(2) central transition in the uud state (B=11.5T T=1.6K). We can see three peaks, corresponding to the three different hyperfine fields. Two peaks at the high frequency side are close to each other, and they are both near the zero-shift frequency. Referring to Fig 50, we notice that this means the angle θ is near 30 °or 90 °, where we have two peaks close to each other near the zero local field, and another peak at lower frequency (higher local field). It is worth mentioning that the lattice belongs to space group $P6_3/mmc$, where the number "6" means the lattice structure has a 6-degree rotational symmetry. When we rotate the lattice by "360 °/6=60 °", the physics property should conserve. Then it makes sense to see 30 ° line positions is the same as 90 °. In the National High Magnetic Field Lab, we measured a spectrum under the condition T=2K, and B=13.25T with the field in plane, which is also in the uud state. For that measurement, the field direction is almost the same because we wired the NMR

coil the same way as it was in UCLA. The result is shown in Fig 51b. The low frequency part of the ^{137}Ba(2) spectrum is so close to the ^{137}Ba(1) signal that they overlap each other, but it is still distinguishable. The high frequency part of ^{137}Ba(2) spectrum is now a single peak, which indicates that the field is almost right at 30 ° from a-axis.

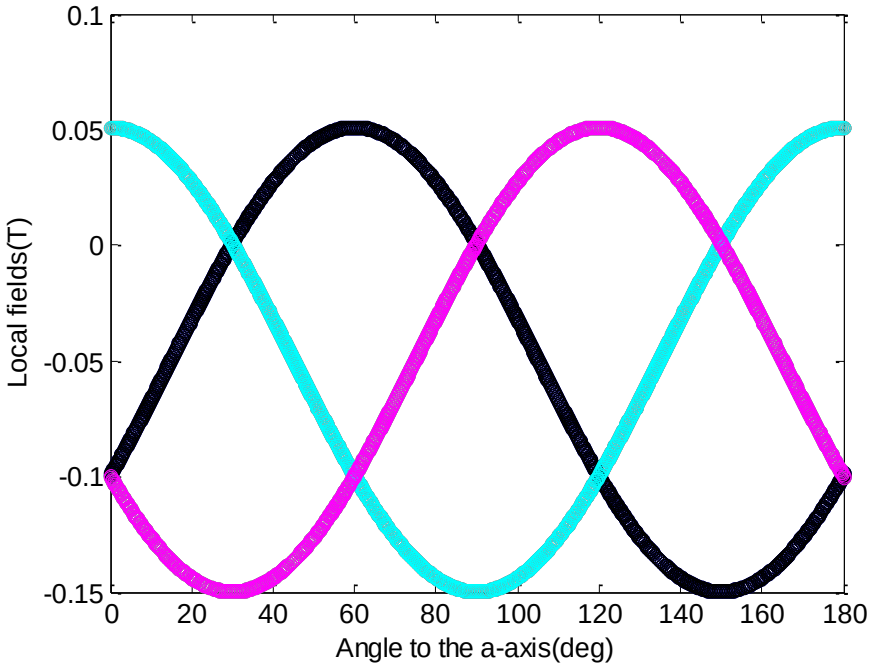

Figure 50 Angle dependence of the local field for ^{137}Ba(2). The three lines come from Ba(2) sites with three different local environments.

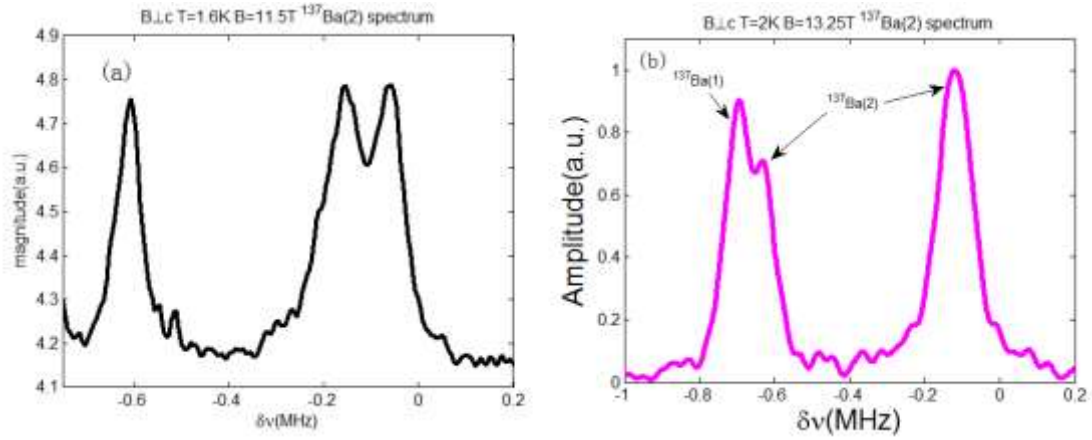

Figure 51 ^{137}Ba(2) spectra. (a) was taken in UCLA, and (b) was taken in NHMFL.

This ^{137}Ba(2) NMR spectrum analysis result has been verified by X-ray diffraction experiment, which directly tested the lattice axis orientation of the sample. This X-ray diffraction measurement was done in the Chemistry Department of UCLA by Dr. Saeed Khan.

4.2 The low field phase at B//ab

The field dependent ^{137}Ba(1) spectra shown in Fig 45 include the low field data we obtained in UCLA. The spectra exhibit several features. First, we have two ^{137}Ba(1) peaks with a 1:2 intensity ratio. Second, the peak at higher frequency (lower shift) has more intensity than the other one. Third, the splitting between the two peaks increase as the field increasing (see Fig 47), and the extrapolation of the line splitting to zero field gives zero splitting. Moreover, the high frequency peak does

not stay at the same hyperfine frequency as we increasing the field, and it does have a field dependence.

The classical 2D triangular lattice has the 120 °state as the ground state at zero field, so it is reasonable to assume the low field phase of $Ba_3CoSb_2O_9$ is some resemblance of the 120 °state. However, since this compound has a layered structure, we would have to consider the magnetic ordering in the context of 6-sublattice structure. There are several candidates for the low field phase, which are shown in Fig 52.

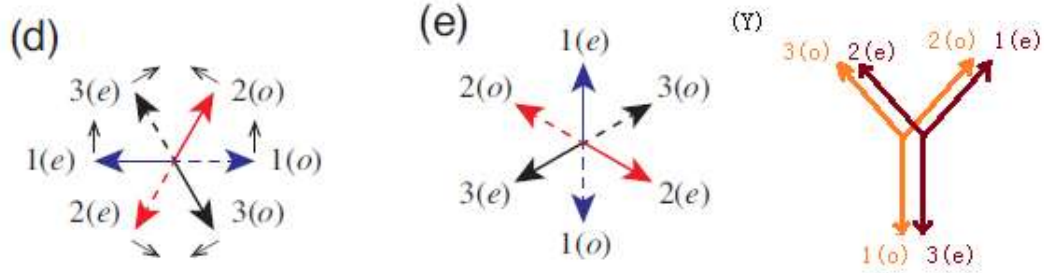

Figure 52 Possible low field phases for $Ba_3CoSb_2O_9$ at B//ab

Among the three candidate phases, (d) and (e) were shown in Fig 42. The (Y) phase is not in Fig 42 because it is not stable under the theoretical model we are using. The three possible states all satisfy the condition that under zero field they resemble the 120 °phase and the net magnetization is zero.

The (d) phase is what we propose in the phase diagram (Fig 25). It states that at zero field the spins in adjacent layers have opposite orientations, which is intuitively correct if we consider the interlayer coupling to be antiferromagnetic. As turning on the field, four sublattices start to get aligned with the field, while the other two approach the antiparallel direction. A Ba(1) site seeing 1(e) and 1(o) as the nearest neighbor would have a larger negative hyperfine field than that of the Ba(1) sites seeing 2(e) and 2(o) (or 3(e) and 3(o)) as the nearest neighbors. Therefore the Ba(1) site split and the NMR line at lower frequency (larger shift) has half intensity of the line at higher frequency (smaller shift). The spins 2(e) and 2(o) (or 3(e) and 3(o)) do not necessarily orient antiparallel to each other at any field, and that is why the high frequency NMR peak does not stay at zero-shift frequency. As we further turning up the field, the phase (d) eventually evolves into the uud phase with a continuous phase transition. Fig 47 has shown the field dependence of the line splitting for ^{137}Ba(1) spectra. The theoretical and the experimental results agree to each other quite well. To further verify the correctness of phase (d), we calculated the averaged magnetic moment of each pair of sublattices using the equation

$$\boldsymbol{m}_{i,theory} = \frac{1}{2}\left(\boldsymbol{m}_{i,o} + \boldsymbol{m}_{i,e}\right), i = 1,2,3 \quad (3.25a)$$

The sublattice magnetic moment $\boldsymbol{m}_{i,(o,e)}$ can be calculated theoretically if we know the orientation of the spins, and that information is provided by Y. Kamiya and C. Batista, who calculated the field dependence of the spin orientations for all 6 sublattices.

Experimentally, we took the shift of each peak of ^{137}Ba(1) spectra, convert it to local field (hyperfine field) unit, and calculated the corresponding magnetic moment by

$$\boldsymbol{m_{exp}} = \frac{\boldsymbol{B_{hf}}}{A_{Ba(1)}^{\perp c}} \quad (3.25b)$$

We can then compare the theoretical results and the experimental values. It is also instructive to compare the first moment of NMR spectra to the published magnetization data. The first moment of ^{137}Ba(1) is taken by calculating the weight average of frequency of the absorption spectrum. The result of the comparison is shown in Fig 53. We can see both the first moment and the sublattice magnetization agree very well between the theoretical and the experimental results, and the first moment of the experimental spectra also align with the magnetization data. The continuous transition from (d) phase to the uud phase happens around 10T, and the magnetic plateau is obvious.

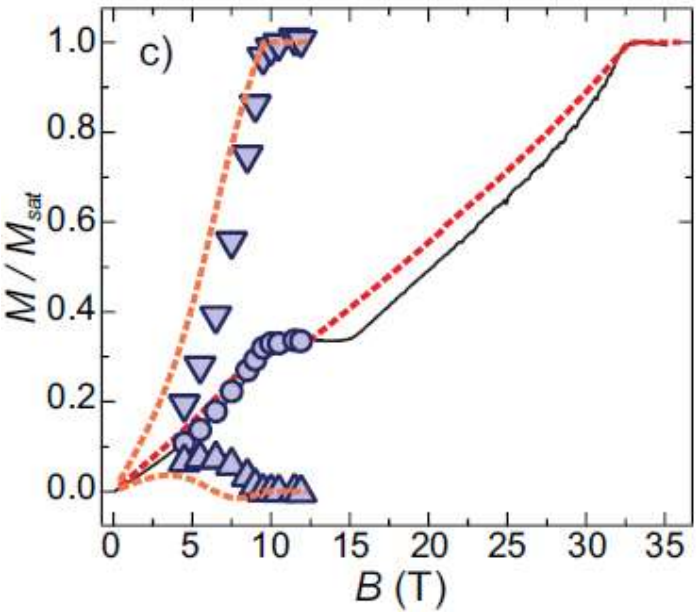

Figure 53 Magnetization vs. magnetic field. The solid, dashed lines are from magnetization results, and the theoretic model, respectively. The data points are derived from the NMR spectra: circles are the first moment of the full ^{137}Ba(1) spectrum, properly normalized, and the triangles are associated to the hyperfine shifts of the two Ba(1) local environments.

The (e) phase is very similar to the (d) phase in that it assumes antiferromagnetic interaction between layers, but it also has major flaws that it cannot be the correct low field phase. We first notice that the NMR peak resulting from 1(e) and 1(o) should have zero-shift, however, it also has the lower intensity, which contradict the experimental results. The 1(e) and 1(o) pair do not change with field, which means at any field, we should have a zero-shift NMR peak for ^{137}Ba(1), but from both the spectra (see Fig 45) and the sublattice magnetization plot (Fig 53), we realized this is not true since the peak near zero-shift certainly has a field dependence. Furthermore, when we put the (e) and the uud phase together, we

would find that there is no "smooth" way for the spin system to evolve from the (e) phase to the uud phase. In other words, a continuous phase transition is not plausible.

Phase (Y) has its foundation when the interlayer coupling J' is sufficiently small compared to the intralayer coupling J (see ref. 15 Fig 6). However, at zero field, the line splitting still exists. For example, the Ba(1) site having 1(e) and 1(o) as nearest neighbors feels a different local field from the Ba(1) site seeing 2(e) and 2(o) as the nearest neighbors.

4.3 The high field phases and the phase diagram of $Ba_3CoSb_2O_9$ with B//ab

The high field (B≥13.25T) ^{137}Ba spectra were taken in NHMFL in a dc resistive magnet at temperature T=2K. The spectra of both ^{137}Ba(1) and ^{137}Ba(2) are shown in Fig 54. The proposed phases are listed besides the spectra with corresponding colors.

If we look at the spectrum at 14.5T, we observe three peaks, which are labeled as a, b, and c in the plot. Peak "a" is purely ^{137}Ba(1) signal, corresponding to the ^{137}Ba(1) nucleus that has two "up" spin as nearest neighbors. Peak "b" is a

combination of ^{137}Ba(1) signal and ^{137}Ba(2) signal, and the 137Ba(1) portion of :b" comes from the nucleus seeing one "up" and one "down" spin as the nearest neighbors. Peak "c" is purely ^{137}Ba(2) signal, which was a double peak when we look at the spectrum at 11.5T (see Fig 51a). The reason these two peaks merge is that in NHMFL, the applied field is closer to 30 ℉rom a-axis (refer to Fig 50).

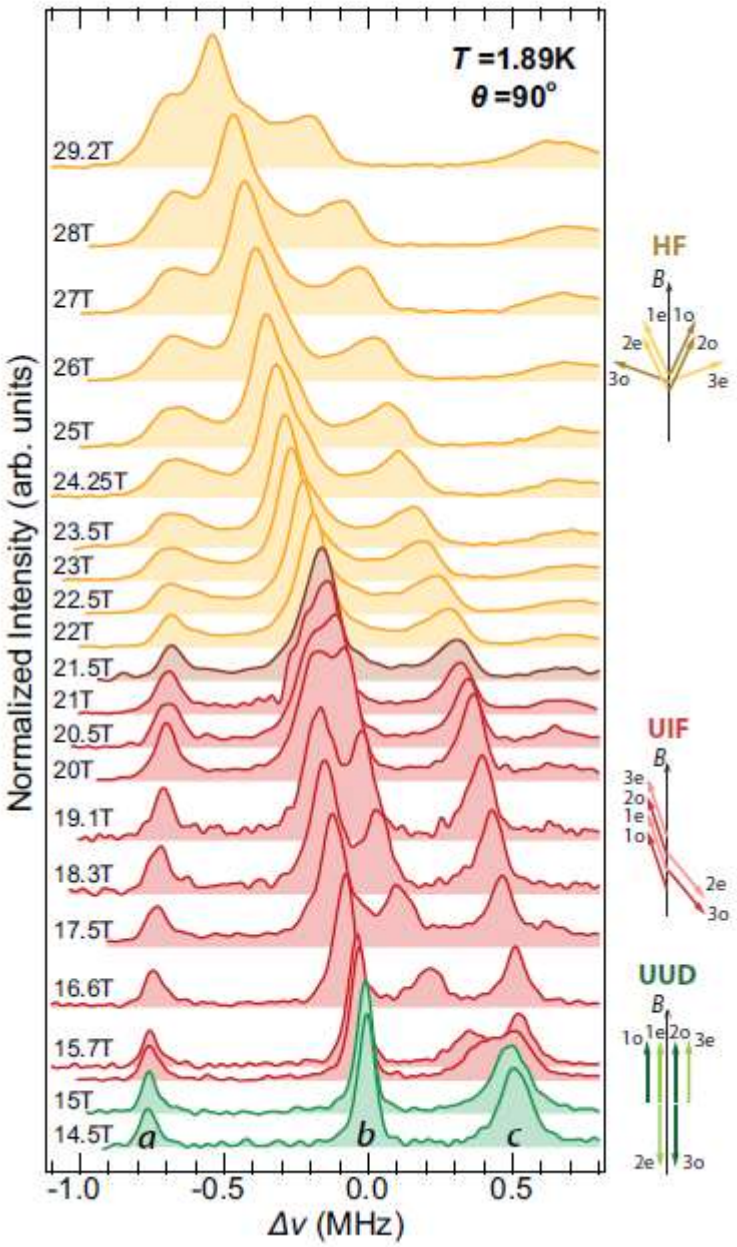

Figure 54 ^{137}Ba central transition absorption spectra at varying applied magnetic fields for B//ab. Spectra recorded in each of the accessed phases is distinguished by color, with the baseline offset according to the field strength.

As the field going up, there is a phase transition at about 15.5T, signified by the fact that the line splitting of ^{137}Ba(1) spectrum starts to shrink after 15.5T, which

means it is no longer the uud phase. The change in the ^{137}Ba(2) spectrum is also obvious. After 15.5T, Peak c gets broader a lot, and then starts to split. After the splitting, the left peak moves quickly towards Peak b with increasing field and merge into Peak b completely after 21.5T.The right part of Peak c also moves towards Peak b but much slower, and we can still distinguish it at the highest field we reached, 30.4T, which is very close to the saturation field for B//ab direction (31.9T, see ref [22]).

The phase sequence is predicted to be uud state → canted coplanar phase (b) → coplanar phase (c). Theorists calculate the field dependence spin orientations for all six sublattices, so it is straightforward to calculated the line splitting of ^{137}Ba(1) central transition spectrum and compare it to the experimental result, as a first check. The comparison is shown is Fig 55.

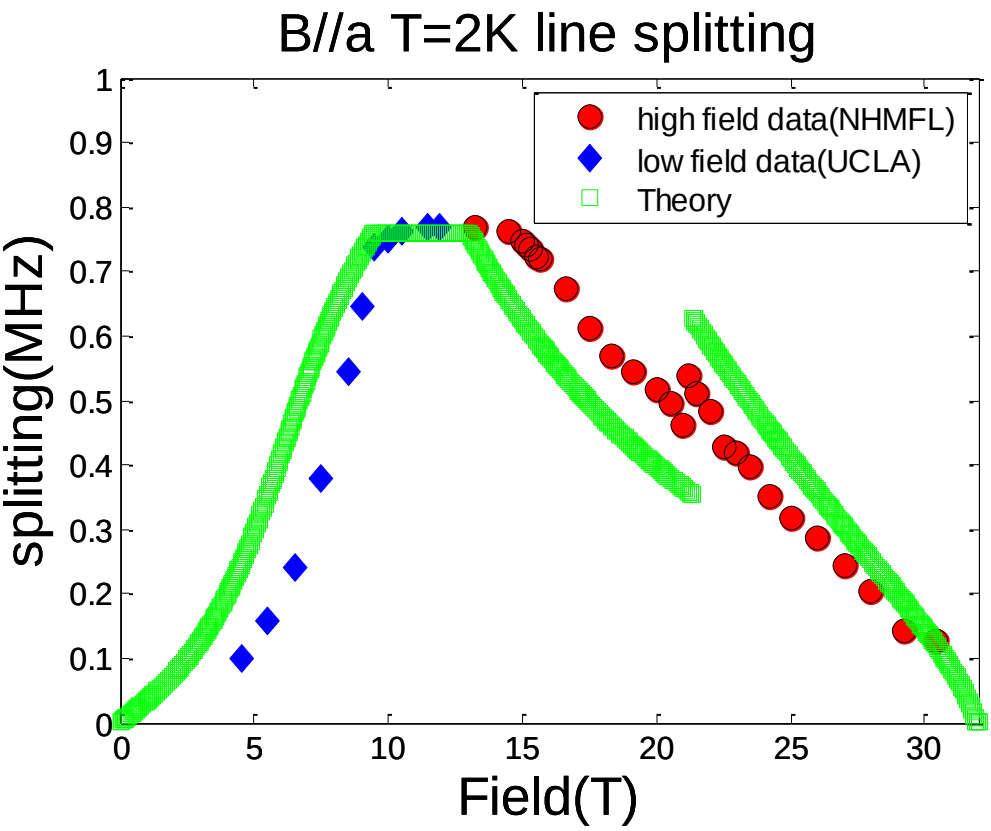

Figure 55 Line splitting of 137Ba(1). The blue points come from low field (<12T) measurements in UCLA, and the red points come from the high field (>13T) measurements in NHMFL. The green line is the predicted line splitting from calculation.

In Fig 55, the experimental line splitting is taken by measure the frequency difference of two ^{137}Ba(1) peaks. The line splitting in the uud state is the same for the experimental results in UCLA and in NHMFL, which proves the reproducibility of the measurement, and reassures the legitimacy of normalizing the theoretical line splitting in the uud state to the experimental value. In Fig, 55, the plateau feature is an obvious observation. The plateau area ends at about 15.15T experimentally, and the decreasing of line splitting afterwards is correctly predicted by the theory. Another phase transition happens at about 21.17T, featured by a jump

in the line splitting. The theory agrees with the data in the transition field very well, and the discontinuity is more substantial. However, the theoretical results work best for the ground state as close to zero temperature as possible, so considered that the experiment was done at 2K, it is natural that thermal effect suppresses the changes in line splitting. In general, the theoretical line splitting correctly describes the experimental results.

^{137}Ba(2) has more complex local environment than ^{137}Ba(1), and part of 137Ba(2) line is mixed with 137Ba(1) line, which further makes it hard to do a quantitative comparison. However, a semi-quantitative comparison is quite instructive. The calculation basically repeat what we did in the uud state since the spin orientations for all sublattices are ready to use. Generally, each Ba(2) has three nearest neighbors, and in the triangular lattice, there are 6 possible local environment, similar to what we have seen in Fig 49 for the uud state. The difference is that these 6 possibilities do not necessarily collapse to three NMR lines as in the uud state. A direct calculation of the local fields gives the results as shown in Fig 56. This plot shows the local fields of ^{137}Ba(2) in the applied field range between 10T and 22T, which includes the uud state and the (b) state. In this figure, we can identify some important features of ^{137}Ba(2) spectra.

Since we have 6 different Ba(2) sites in the magnetic state, we can divide the total intensity of ^{137}Ba(2) central transition spectrum into 6 parts. In the uud state, 4 parts

of the intensity appears in the high frequency (low negative shift) side of the spectrum, and two parts of the intensity sit on the low frequency (high negative shift) side of the spectrum. This has been verified by the ^{137}Ba(2) spectra shown in Fig 51. After the phase transition from uud state to the (b) phase, Fig 56 shows that the high frequency peak of ^{137}Ba(2) split into two peaks with equal intensity, and one of the split peak moves towards the high negative shift side when increasing the field. Finally that peak merge with the low frequency (high negative shift) peak of ^{137}Ba(2), as well as the ^{137}Ba(1) spectrum. The field dependence evolution correctly mimics what we observe from the experimental data, which in turn serves as strong evidence that the theoretical phase diagram (see Fig 25) for B//ab is correct for the region below 22T.

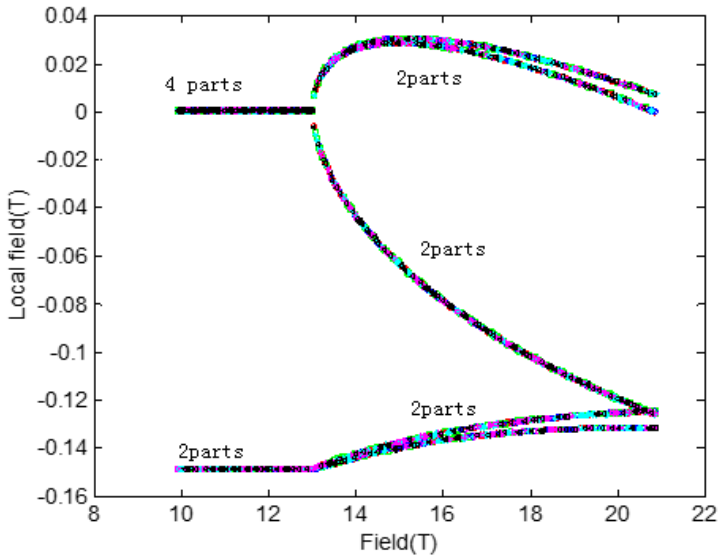

Figure 56 ^{137}Ba(2) local fields in the intermediate field range. There are 6 possible local environments for Ba(2) and they are equally weighted.

The high field spectra are more difficult to analyze because the signals of ^{137}Ba(1) and ^{137}Ba(2) central transitions entangle each other. However, we can still find some convincing clue about the magnetic state.

The theoretical prediction claims that the high field phase is phase (c) in Fig 42.

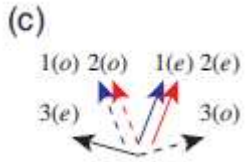

Fig 42c

In this phase, Ba(1) sites seeing 1(o)1(e) or 2(o)2(e) as nearest neighbors should have larger negative shift than those seeing 3(o)3(e) as nearest neighbors, so we should expect the low frequency peak of ^{137}Ba(1) central transition to have twice intensity as the high frequency peak. As a contrast, in phase (b) the low frequency peak has half intensity as the high frequency peak. If there were no Ba(2) signal, we would expect an "intensity flip" before and after the phase transition field 22.17T. It is unfortunate that the high frequency part of ^{137}Ba(1) spectrum merges with the ^{137}Ba(2) spectrum, and to compare the intensity, we need a prediction including both ^{137}Ba(1) and ^{137}Ba(2). To analyze the ratio of intensity, we first notice that the Ba(2) sites are twice as many as the Ba(1) sites, so the total intensity of ^{137}Ba(2) central signal is twice as much as that of ^{137}Ba(1). Let us assume the total intensity of ^{137}Ba(1) is 3, and total intensity of ^{137}Ba(2) is 6. We pick up 14.5T, 16.6T, 20.5T, and 23.5T as the representative fields for our analysis (see Fig 57).

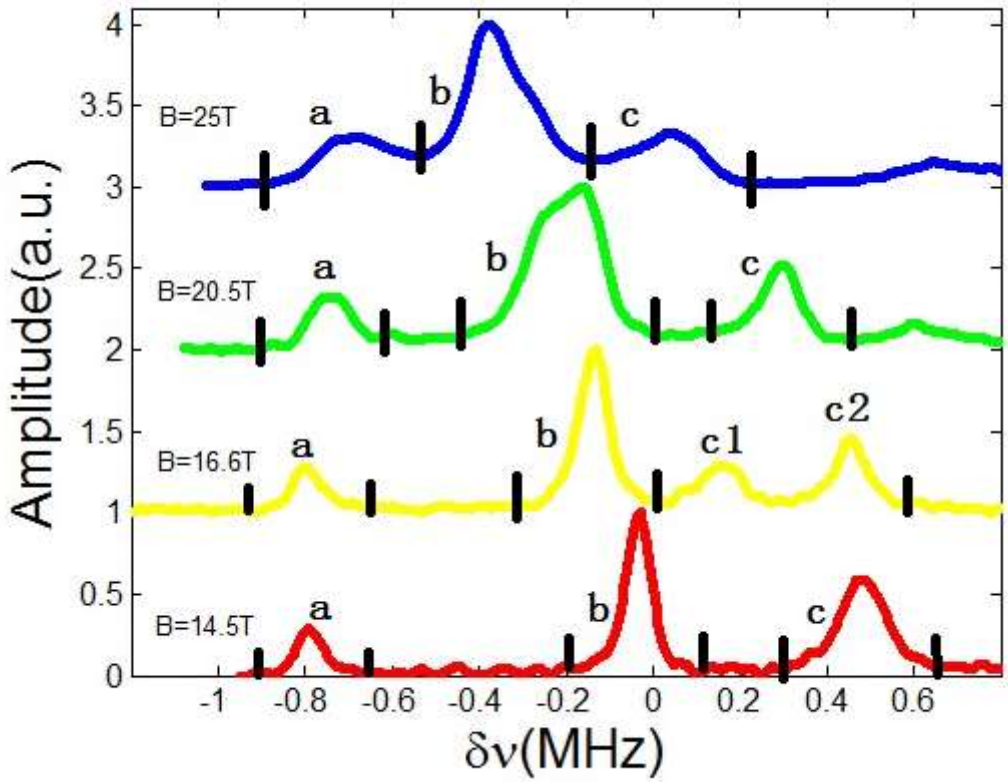

Figure 57 B//ab, spectra at selected fields. The vertical black lines shows the starting and ending frequency between which we calculated the intensity.

When B=14.5T, the system is in uud state. The spectrum has 3 peaks. The left one, labeled as "a", contains 1/3 of ^{137}Ba(1) central transition signal, so its intensity is 1. The middle peak, labeled as "b", contains 2/3 of ^{137}Ba(1) and 1/3 of ^{137}Ba(2), so its intensity is 4. The right peak, labeled as "c", contains 2/3 of ^{137}Ba(2) signal, so its intensity is 4. The ratio of these three peaks is thus 1:4:4.

When B=16.6T, the system is in the canted coplanar (b) phase, and the spectrum has 4 peaks. The left one, denoted as “a”, contains 1/3 of ^{137}Ba(1) central transition signal, so its intensity is 1. The middle peak, denoted as “b”, contains 2/3 of ^{137}Ba(1) and 1/3 of ^{137}Ba(2), so its intensity is 4. The right two peaks, denoted as c1 and c3, each contains 1/3 of ^{137}Ba(2) signal, son each has an intensity 2. The ratio of intensity is thus 1:4:2:2.

When B=20.5T, the system is still in phase (b), but the middle two peaks collapse and we can see in general three parts of a spectrum. The left one, denoted as “a”, contains 1/3 of ^{137}Ba(1) central transition signal, so its intensity is 1. The middle part, denoted as “b”, contains 2/3 of ^{137}Ba(1) and 2/3 of ^{137}Ba(2), so its intensity is 6. The right peak, denoted as “c”, contains 1/3 of ^{137}Ba(2), so its intensity is 2. The ratio of intensity is thus 1:6:2.

When B=23.5T, the system is in phase (c). The left peak, denoted as “a”, has 2/3 of ^{137}Ba(1) central transition signal, so its intensity is 2. The middle part, denoted as “b”, contains 1/3 of ^{137}Ba(1) and 2/3 of ^{137}Ba(2), so its intensity is 5. The right peak, denoted as “c”, contains 1/3 of ^{137}Ba(2), so its intensity is 2. The ratio of intensity is thus 2:5:2.

The intensity of each part of the spectra can also be measurement from the experimental data directly, and the results are shown in Table III

	Observed intensity			Expected result		
B(T)	a	b	c	a	b	c
14.5	1.1	3.9	4.1	1	4	4
16.6	1.1	4.1	1.8+2	1	4	2+2
20.5	1.2	5.8	2.1	1	6	2
25	1.8	5.2	1.9	2	5	2

Table III

From the table, we can see that the experimental intensity is in good agreement with the expected results. The increase in relative intensity for Peak a from 20.5T to 25T supports the phase transition from Phase (b) to Phase (c).

As a summary to this section, I list in Fig 58 the phase sequence for B//ab as the field increasing from zero to the saturation field.

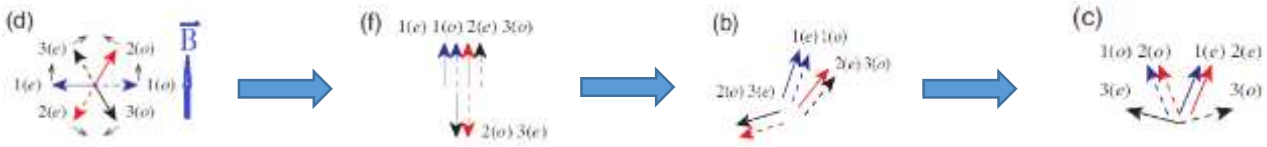

Figure 58 Phases for B//ab. From low field to high field.

4.4 NMR results of the “new phase transition”

In 2013, N. Fortune claimed a new phase transition for B//ab at temperature lower than 700mK, according to the heat capacity measurement. [35] The phase boundary is about 6.5T, which comes from the local maximum of field dependent specific heat data (Fig 59).

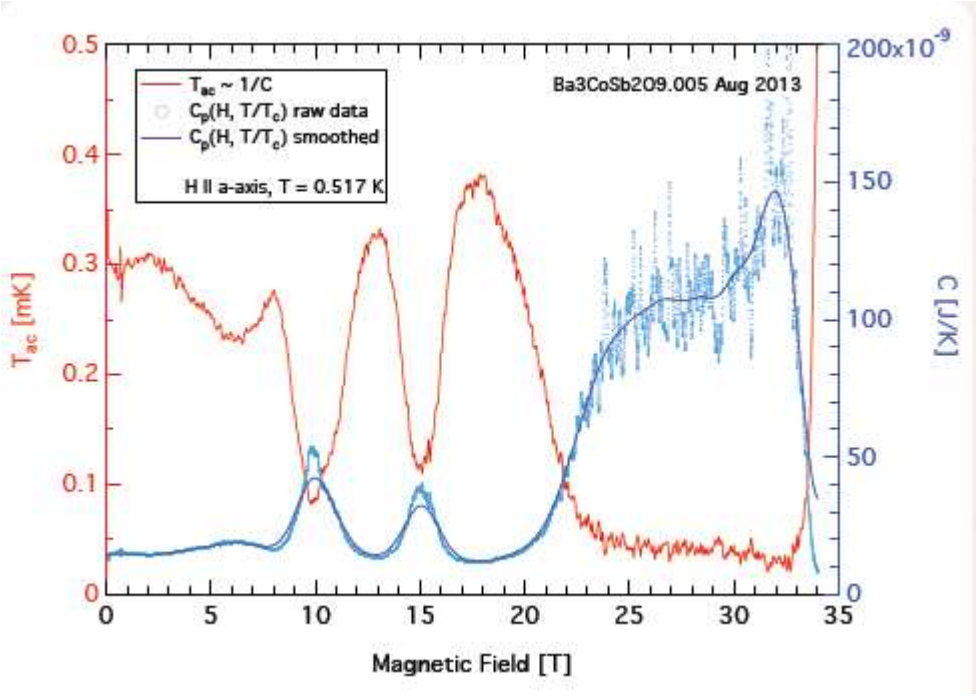

Figure 59 Thermodynamic measurement results by N. Fortune [35]. The phase transitions at about 10T and 15T are well defined by the local maximum of specific heat. However, the new “phase transition” at 6.5T is ambiguous.

The significance of the new “phase transition” is quite weak that we can barely identify it. This transition was not observed when temperature is higher than 700mK. To verify the existence of this phase transition, we measured field dependent NMR spectra for ^{137}Ba(1) central transitions at 100mK, which should

be very sensitive to the change in local magnetization. However, the results show that the sublattice magnetizations reproduce exactly what we obtained at 1.6K, as illustrated in Fig 60. This means across the supposed phase boundary at about 6.5T, there is no change in the local magnetization for Ba(1), and a phase transition is not plausible just by looking at the spectra data. IN a later chapter, we will see that a field dependent spin-lattice relaxation rate result does not confirm the new "phase transition" either.

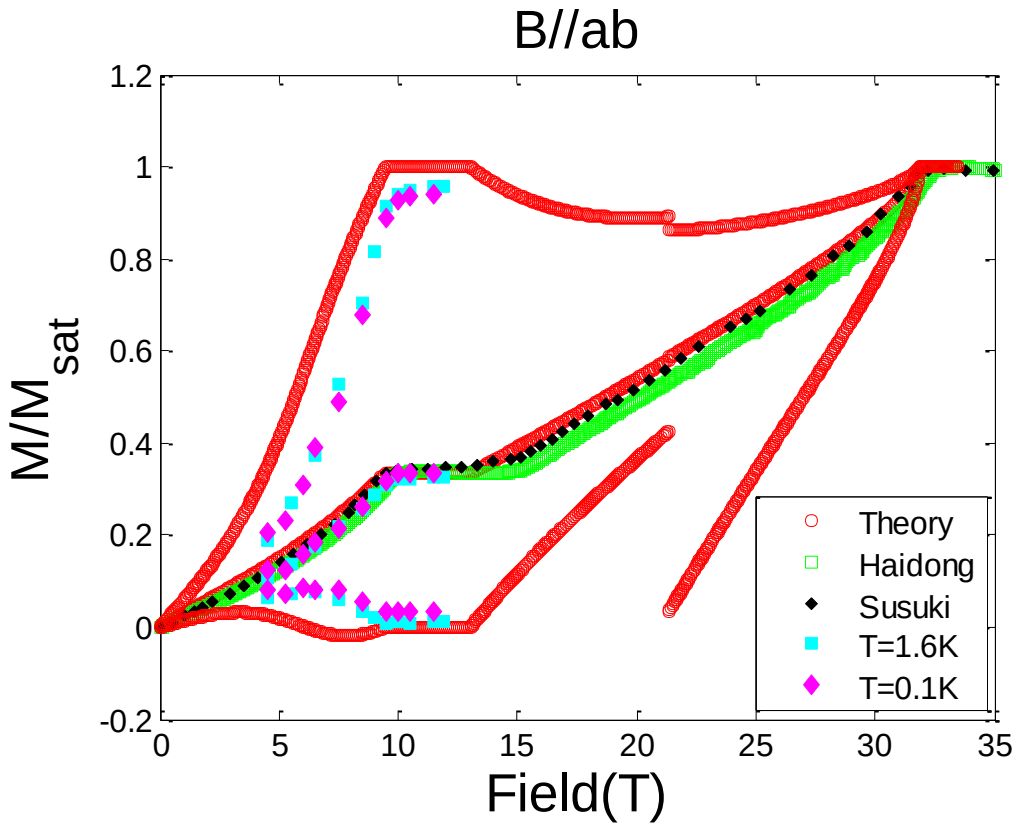

Figure 60 Sublattice magnetizations normalized. The red lines are theoretically calculated magnetizations. The green points (Haidong) and black points (Susuki) are experimental results of magnetization. The light blue points come from NMR measurements at 1.6K, and the magenta points come from NMR measurements at 0.1K.

4.5 Spectra analysis for B//c direction

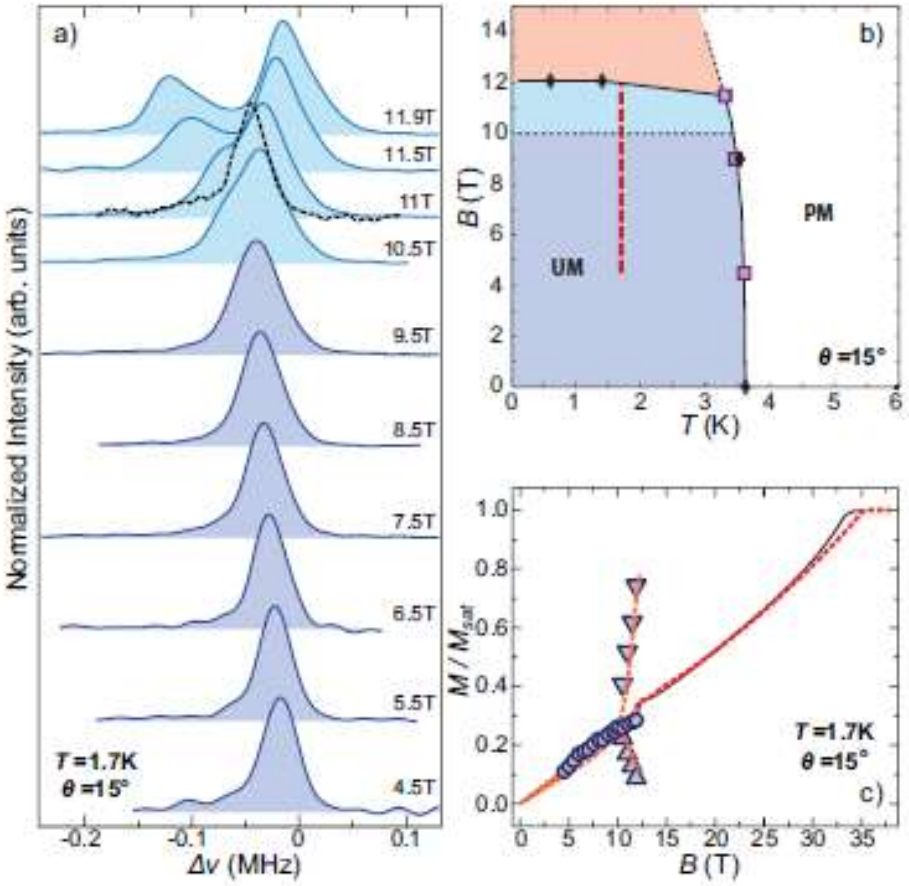

Figure 61 (a) ^{137}Ba(1) central transition spectra with applied field B almost parallel to c-axis (15^{o} misalignment). The dotted black line shows the spectrum at 11T when B//c as a comparison. (b) The experimental phase diagram from the magnetization data, and T_N is decided by NMR T_1 measurements. (c) Comparison of NMR first moments and sublattice magnetizations taken from ^{137}Ba(1) spectra with the magnetization data. Red lines are calculated from theoretical model, and the black line is the actual data taken by H.D. Zhou [17]

In Fig 61(b), the low field phase diagram of $Ba_3CoSb_2O_9$ with B//c is plotted. The phase

below 12T is predicted to be the umbrella phase, where all the sublattice spins make the same angle with c-axis, so the Ba(1) central transition should be just a single NMR line. The initial NMR experiment was done with 15^0 misalignment from c-axis, so we can see from Fig 61(a) that the Ba(1) spectrum starts to show some structure above 10T. This feature can be precisely captured by our theoretical model, as shown in Fig 62.

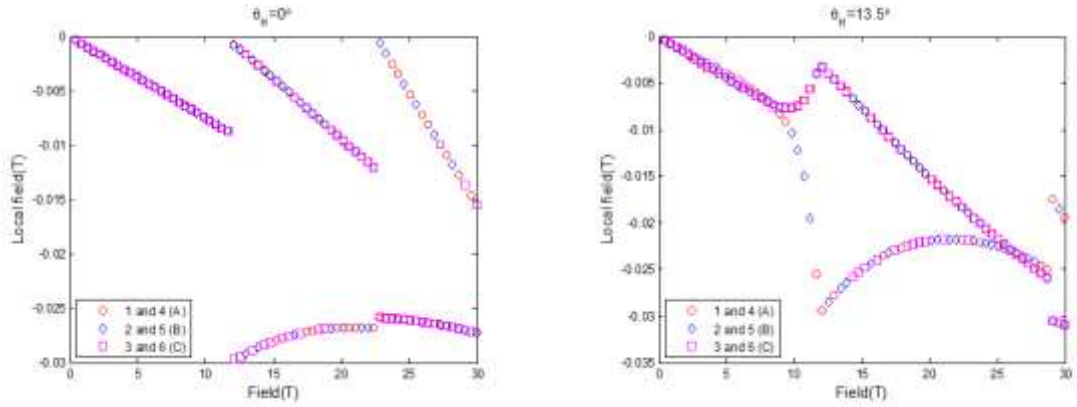

Figure 62 Theoretical prediction of the line splitting for 137Ba(1) central transition. When well aligned with B//c, the line splitting only appear after the 12T phase transition. When there is misalignment, the line splitting starts earlier in field.

According to the theoretical prediction, when the field is exactly parallel to the c-axis of the sample, we should expect a single Ba(1) line starting from zero field till the phase transition field (~12T). However, when there is a misalignment (13.5^o for example), the line splitting appears earlier in field because of the distortion of umbrella phase. We did not expect the 15^o misalignment at the beginning of the experiment, but it turns out to be another validation of the theoretical model we are using. This feature is also verified by a rotation study shown in Fig 63.

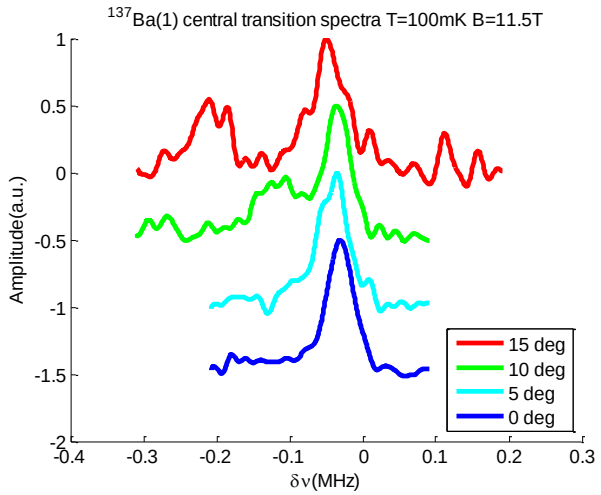

Figure 63 ^{137}Ba(1) central transition spectra with different angles from c-axis, B=11.5T, T=100mK.

In Fig 63, we are at a field (B=11.5T) very close to the transition field (~12T), and the ^{137}Ba(1) spectra obviously have two peaks at 15° and 10°. The line width is getting much narrow and only has a single peak we well aligned. The low field spectra with good alignment (B//c) are shown in Fig 64, and we just see a single line up to 11.9T, which is consistent with the umbrella phase.

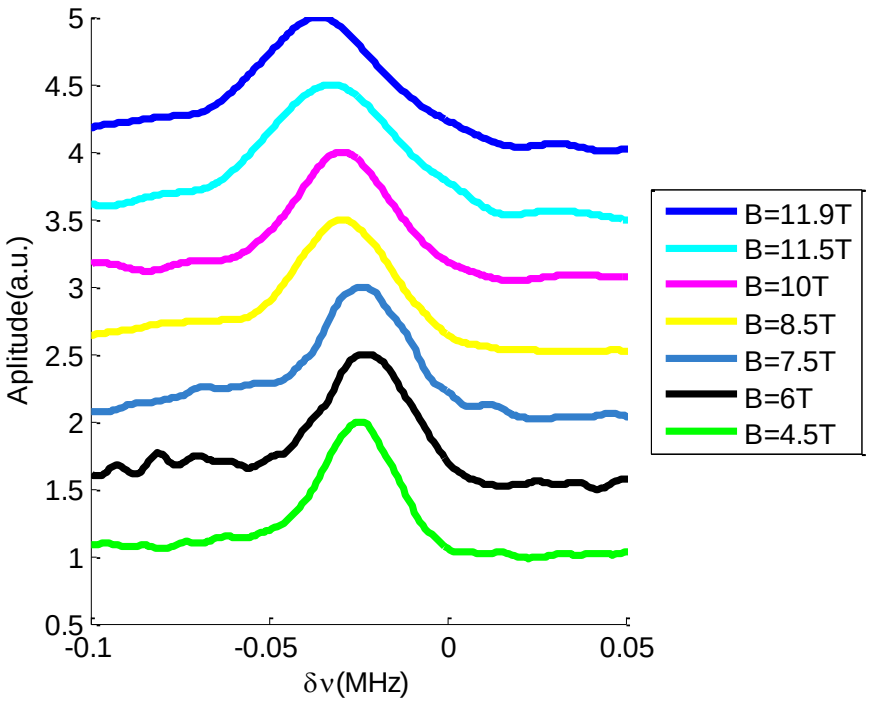

Figure 64 ^{137}Ba(1) central transition spectra, T=100mK, B//c

In the theoretical phase diagram shown in Fig 25, the high fields' phases are assumed to be the canted coplanar phase followed by the (c) phase. For B//c, Ba(1) and Ba(2) signals are well separated, so it is more straightforward to analyze the spectra. In Fig 65, the spectra of Both ^{137}Ba(1) and ^{137}Ba(2) central transitions are plotted.

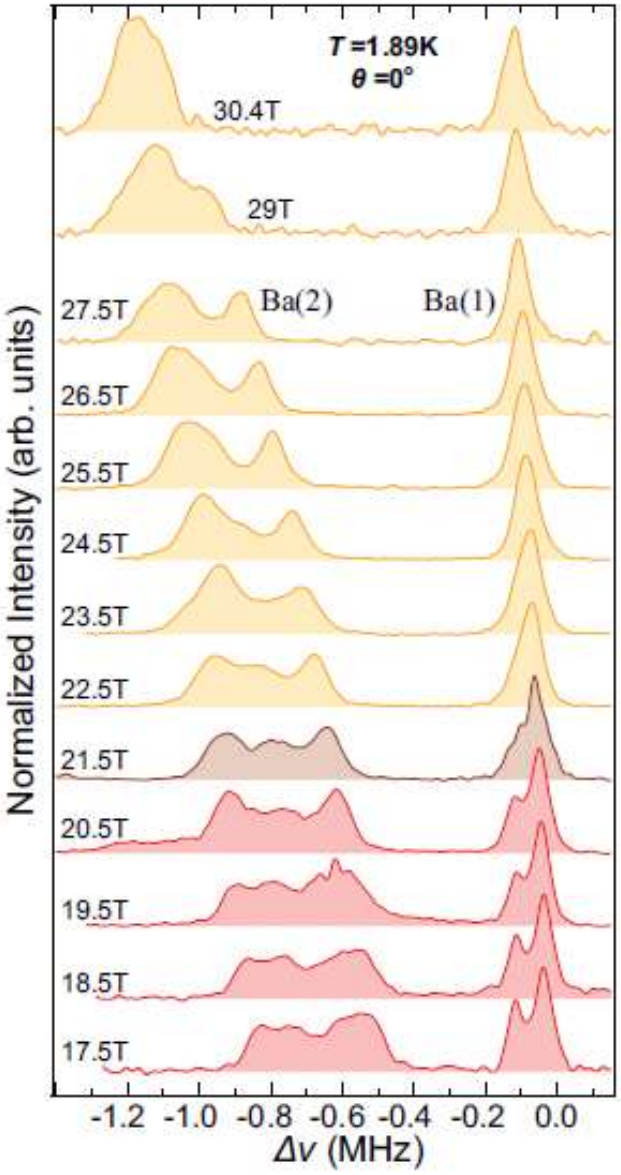

Figure 65 ^{137}Ba central transition spectra at various fields. Different colors label different phases proposed by the theoretical model.

In Fig 65, we can see that the Ba(1) spectra have two separated lines from 17.5T to 21.5T, which is consistent with the canted coplanar phase (b). Above 21.5T, the structure in Ba(1) spectra disappears and we can see only a single line. There are two

possibilities for this change. There could be a phase transition at 21.5T that results in a single Ba(1) for the high field phase, or there is no phase transition and the sensitivity of our experiment is not enough to resolve the two peaks of Ba(1) spectra above 21.5T. If we look at the line splitting of Ba(1) as a function of magnetic fields (Fig 66), we can immediately notice that it already deviates from the theoretical prediction, since we do not observe the "jump" a the transition field. On the contrary, the experimental line splitting decreases at a faster rate above 21.5T, which might indicate a phase transition but different from the prediction in Fig 25.

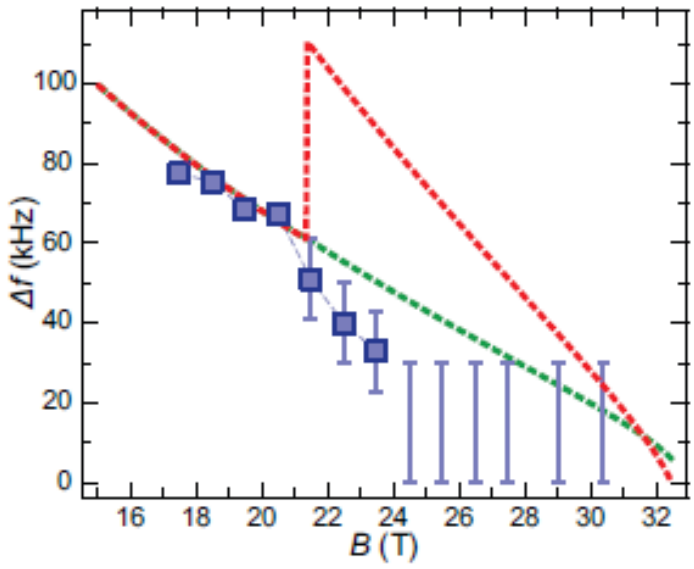

Figure 66 Ba(1) spectral lime splitting vs applied field for B//c, extracted from the data shown in Fig 65. The red dashed line is the theoretical prediction for line splitting, and the green line is an extrapolation of Ba(1) splitting if no phase transition occurs. The blue lines above 24T denote an estimate of the minimum splitting that can be resolved due to the spectral linewidth.

When we look at the Ba(2) spectra in Fig 65, we also notice that below 21.5T, the spectra look complex, with multiple contributions. Above 21.5T, the spectra start to be clean in the sense that we can see only two peaks. This is another indicator for a phase transition at 21.5T. However, for a perfectly aligned B//c direction, we expect the Ba(2) spectra to be symmetric due to the time-reversal symmetry, which is obviously not the case in our data. So right now I have to leave this question unresolved, and more input from both theory and experiment is needed to figure out the problem.

Chapter Five

Spin-lattice Relaxation measurements on $Ba_3CoSb_2O_9$

From the perspective of statistical physics, in equilibrium, the number of nuclear spins residing on a specific energy level E_α is proportional to e^{-E_α/k_BT}. When the nuclear spin system absorbs energy from an outside source, the population of spins on each energy level would deviate from its equilibrium value. Afterwards, the nuclear system would try to go back to equilibrium and spins at higher energy level would try to jump back to low energy level. The jump can be done only by energy exchange with the environment, which is typical the lattice or the nearby electron spins. This process is called the spin-lattice relaxation. The significance of the relaxation process is that it provides a way of observing the dynamic properties of the lattice or electron spins, so it constitutes an essential part for a complete NMR study.

5.1 General theories of spin-lattice relaxation

First we consider a transition from energy level α to energy level β, as shown in Fig 67.

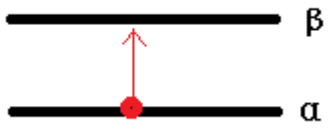

Figure 67 For illustration purpose, a nuclear spin jump from energy level α to energy level β.

The number of the transitions per unit time from level α to level β can be calculated by the product of finding a spin in energy level α times the probability of the transition, and it can be written as $p_\alpha W_{\alpha\beta}$.

To describe the collective behavior of the whole nuclear spin system, we use an alternative way to interpret the different population at different energy levels. Instead of saying how many spins are in a specific energy level, we state that the spin system has an energy E_a with probability p_a. Then the normalization requires

$$\sum_a p_a = 1 \quad (5.1)$$

The average energy of the system is

$$\bar{E} = \sum_a p_a E_a \quad (5.2)$$

The advantage of this interpretation is that the nuclear spin system does not necessarily obey the Maxwell-Boltzmann statistics. It also holds true for systems obeying Fermi-Dirac or Bose-Einstein statistics, and we only need to consider the statistics when expressing the wave function of the system.

The spin-lattice relaxation is essentially the exchange of energy, so we should calculate the rate of energy change for the nuclear spin system. Using Eq (5.2) we obtain:

$$\frac{d\bar{E}}{dt} = \frac{d}{dt}\sum_a p_a E_a = \sum_a E_a \frac{dp_a}{dt} \quad (5.3)$$

As discussed at the beginning of this section, we have

$$\frac{dp_a}{dt} = \sum_b (p_b W_{ba} - p_a W_{ab}) \quad (5.4)$$

In Eq (5.4), $p_b W_{ba}$ represents the probability per unit time that the lattice induces a transition of the nuclear spin system from b to a, and $p_a W_{ab}$ represents the probability per unit time that the lattice induces a transition of the nuclear spin system from a to b. By subtracting the latter from the former, we obtain the probability per unit time for energy level α due to the transition between a to b, and the sum over all the possible b states gives the total probability per unit time. Substituting Eq (5.4) into Eq (5.3) to get

$$\frac{d\bar{E}}{dt} = \sum_{a,b} (p_b W_{ba} - p_a W_{ab}) E_a = \frac{1}{2}\sum_{a,b} (p_b W_{ba} - p_a W_{ab})(E_a - E_b) \quad (5.5)$$

It is useful to define a spin temperature $\beta = \frac{1}{kT}$, where k is the Boltzmann constant. Then we can also write

$$\frac{d\bar{E}}{dt} = \frac{d\bar{E}}{d\beta}\frac{d\beta}{dt} \quad (5.6)$$

We realize the probability per unit time is a function of spin temperature β

$$p_a = \frac{e^{-\beta E_a}}{Z} \quad (5.7)$$

where Z is the partition function of the nuclear spin system. Then we can write

$$\frac{d\bar{E}}{d\beta} = \frac{d}{d\beta}\sum_a p_a(\beta)E_a \quad (5.8)$$

When the spin temperature β is so high that $\beta E_a \ll 1$, we can find a good approximation of the partition function Z by expanding $e^{-\beta E_a}$ in the power series of βE_a, and only keep the leading terms:

$$\mathrm{Z} = \sum_a (1 - \beta E_a + \frac{\beta^2 E_a^2}{2!} + \cdots) \quad (5.9)$$

It is straightforward to see that when the temperature T is infinitely large, the partition function Z just equals the total number of states, and we can denote it as Z_∞. To further simplify the problem, we measure the energy E_a in a reference frame that the trace of the Hamiltonian is zero, which means

$$\mathrm{Tr}\mathcal{H} = \sum_a E_a = 0 \quad (5.10)$$

Then the first order term in Eq (5.9) is zero, and if we further neglect the second and higher order terms, we reach the approximation that

$$\mathrm{Z} = Z_\infty \quad (5.11)$$

Then

$$\frac{d\bar{E}}{d\beta} = \frac{d}{d\beta}\sum_a p_a(\beta)E_a = \frac{1}{Z_\infty}\frac{d}{d\beta}\sum_a e^{-\beta E_a}E_a = -\frac{1}{Z_\infty}\sum_a E_a^2 e^{-\beta E_a}$$

$$= -\frac{1}{Z_\infty}\sum_a E_a^2(1 - \beta E_a + \cdots) \cong -\frac{1}{Z_\infty}\sum_a E_a^2 \quad (5.12)$$

In the last step, we expand $e^{-\beta E_a}$ and make the approximation under high temperature limit. Furthermore,

$$\frac{d\bar{E}}{dt} = \frac{d\bar{E}}{d\beta}\frac{d\beta}{dt} = -\frac{d\beta}{dt}\frac{\sum_a E_a^2}{Z_\infty} \quad (5.13)$$

From Eq (5.7) we immediately have

$$p_a = p_b e^{\beta(E_b - E_a)} \quad (5.14)$$

To continue our calculation, we have to figure out the transition probability W_{ba}. To do this, we assume the spin system is in thermal equilibrium with the lattice, and p_a is re-written as p_a^L, where L stands for "lattice". The detailed balance requires

$$p_b^L W_{ba} = p_a^L W_{ab}$$

which gives the result

$$W_{ba} = W_{ab}\frac{p_a^L}{p_b^L} = W_{ab}e^{\beta_L(E_b - E_a)}$$

Now we are in a position to calculate $\frac{d\bar{E}}{dt}$ from Eq (5.5)

$$\frac{d\bar{E}}{dt} = \sum_{a,b}(p_b W_{ba} - p_a W_{ab})E_a = \frac{1}{2}\sum_{a,b}(p_b W_{ba} - p_a W_{ab})(E_a - E_b)$$

$$= \frac{1}{2}\sum_{a,b} p_b W_{ba}[1 - e^{(\beta - \beta_L)(E_b - E_a)}](E_a - E_b)$$

By expanding the exponential term to the first order, we further obtain

$$\frac{d\bar{E}}{dt} \cong \frac{1}{2}\sum_{a,b} p_b W_{ba}(E_a - E_b)^2(\beta - \beta_L)$$

We can also expand $p_b = \frac{e^{-\beta E_b}}{Z} = \frac{e^{-\beta E_b}}{Z_\infty}$ to the leading term and simply get $p_b \cong \frac{1}{Z_\infty}$, which allows us to further simplify the results

$$\frac{d\bar{E}}{dt} \cong \frac{1}{2Z_\infty}(\beta - \beta_L)\sum_{a,b} W_{ba}(E_a - E_b)^2 = -\frac{d\beta}{dt}\frac{\sum_a E_a^2}{Z_\infty}$$

Finally we can write

$$\frac{d\beta}{dt} = (\beta_L - \beta)\left[\frac{1}{2}\frac{\sum_{a,b} W_{ba}(E_a - E_b)^2}{\sum_a E_a^2}\right] = \frac{\beta_L - \beta}{T_1} \quad (5.15)$$

Here we define T_1 as

$$\frac{1}{T_1} = \frac{1}{2}\frac{\sum_{a,b} W_{ba}(E_a - E_b)^2}{\sum_a E_a^2} \quad (5.16)$$

We should notice that in obtaining the result Eq (5.16), we assume a single spin temperature for the nuclear spin system, so the system relax with a single exponential function. However, the rate equation Eq (5.5) does not exclude the cases for multiple relaxation times.

From Eq (5.16), we notice that the key to solve for the relaxation time if to find the characteristics of the transition rate W_{ba}, and we will show an example in the next section for spin-3/2 system.

5.2 NMR methods for T_1 measurement

A spin-1/2 nucleus in a homogeneous environment relaxes with a single exponential, and the functional form depends on the details of the experiment. The most commonly used techniques are the "Inversion-Recovery" and the "Saturation- Recovery" methods.

The "Inversion- Recovery" method is illustrated in Fig 68 in the classical picture. The measurement starts from equilibrium state, and in the rotating reference frame, the nuclear spin takes +z direction initially (Fig 68(a)). A π pulse is then applied to the system, which inverts the spin to –z direction (Fig 68(b)). After a time t, the

spin recovers by a certain amount (Fig 68(c)). The z-component amplitude of the recovered spin is a function of the waiting time t

$$\mathrm{M(t)} = M_0\left(1 - 2e^{-\frac{t}{T_1}}\right) \quad (5.17)$$

We can intuitively verify the correctness of Eq (5.17) by noticing that $\mathrm{M}(0) = -M_0 \; and \; M(\infty) = M_0$. To measure the amplitude M(t), we can either use the FID detection or an echo detection. From Fig 68(d) to Fig 68(f) describes a commonly used echo pulse sequence. If we repeat the same experiment with different delay time t, we can fit our data with the function form (5.17) and obtain T_1 from the fitting result. The graphic appearance of Eq (5.17) is shown in Fig 69. Experimentally, we select a reasonable number of delay times equally spaced logarithmically ranging from two orders of magnitude smaller than T_1 to 10 times T_1. To make sure the initial condition is the same for each experiment, we always wait long enough ($10T_1$) before every measurement.

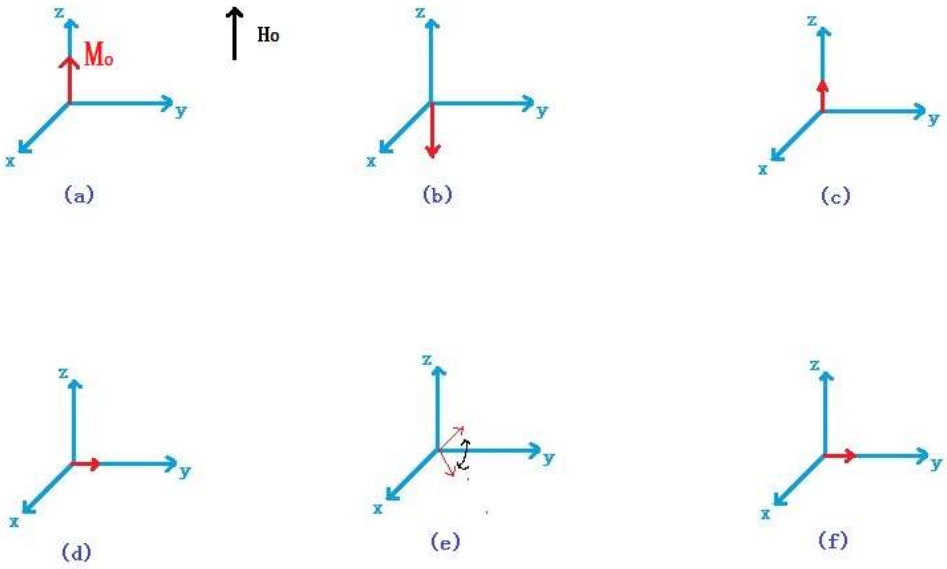

Figure 68 (a) In equilibrium, the nuclear spin take value M_0 in the z-direction in the rotating frame. (b) After a pi-pulse, the spin is inverted to $-M_0$. (c) after some waiting time t, the spin recovers to a certain amplitude, the direction could be either +z or –z. (d) Apply a pi/2 pulse which knocks the spin to the xy plane. (e) Waiting a time τ, the nuclear spins fan out in the xy plane. (f) Apply a pi-pulse and wait the same time τ, and then the spins refocus, forming an echo.

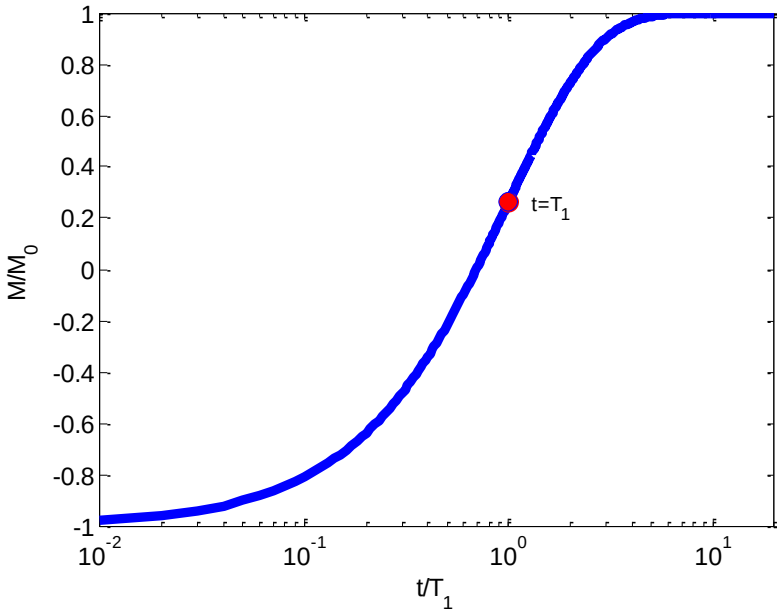

Figure 69 The graph of $M(t) = M_0\left(1 - 2e^{-\frac{t}{T_1}}\right)$. The red point labels where $t=T_1$ point is.

The "Inversion- Recovery" method becomes time-consuming when T_1 is very long, and the typical time cost when using this method is 100 times T_1. Another shortcoming of the "Inversion- Recovery" method is that when the H_1 field is limited by the experimental setup, the pi-pulse would be very long, which limit the bond width of the measurement. In both cases, a so-called "Saturation- Recovery" method is used. The graphic illustration of this method is shown in Fig 70.

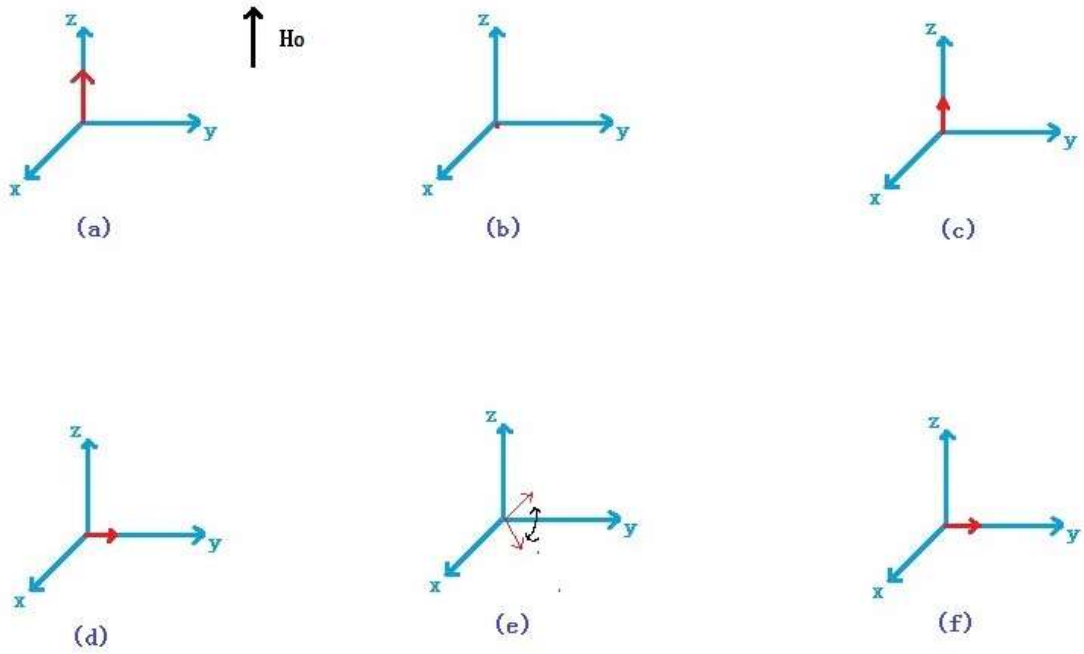

Figure 70 (a). In equilibrium, the nuclear spin take value M_0 in the z-direction in the rotating frame. (b) After several pi/2-pulses, the spin is uniformly distributed in the space and the effective spin is zero (c) after some waiting time t, the spin recovers to a certain amplitude, the direction could be either +z or –z. (d) Apply a pi/2 pulse which knocks the spin to the xy plane. (e) Waiting a time τ, the nuclear spins fan out in the xy plane. (f) Apply a pi-pulse and wait the same time τ, and then the spins refocus, forming an echo.

In the “Saturation- Recovery” method, a “saturation comb” is applied to the nuclear spin system first. The comb constitutes several pi/2 pulses separated by a time interval t_0 much larger than T_2 but much smaller than T_1. The idea is that after each pi/2 pulse, the spin is knocked to the xy plane, and after time t0, the spins totally go out of phase and randomly distributed in the xy plane, while the z-component of the spins do not recover. After several pi/2-pulses, the spins then distributed uniformly all over the space, which we call “saturated”. This saturated state serves as the initial condition for each measurement. The advantage of the “Saturation-Recovery” method is that we do not have to wait a long time between measurements, since the full recover of z-component is not necessary for creating the “saturation”. Moreover, when H_1 field is low and the pi/2 pulse is too long to conduct a reasonable experiment, we can use a shorter pulse for the saturation comb and we can still achieve to start from an almost saturated initial condition.

The functional form for a “Saturation- Recovery” measurement is

$$\mathrm{M(t)} = M_0\left(1 - e^{-\frac{t}{T_1}}\right) \quad (5.18)$$

We can see that when t=0, the amplitude is also zero.

We should note that the “Saturation- Recovery” method is only valid for spin-1/2 system, where we have only two energy levels, and the saturation comb only affect the transition between these two energy levels. For a spin-3/2 or higher spin systems, the electric field gradient changes the splitting between Zeeman energy

levels, and we end up with multiple transitions. While the saturation pulse sequence only affect the central transition, it changes the population on the relevant energy levels, which in turn induces transitions between neighboring energy levels. In this case, if we do not wait enough time for the system returning to equilibrium before each measurement, we end up with doing experiment with different initial conditions, and that distorted the shape of the recovery line and change the result of T_1.

5.3 Spin-lattice relaxation experimental results for B//ab

When approaching the phase boundary of an antiferromagnetic state either by varying temperature or magnetic field, the quantum fluctuation provides extra channels for energy dissipation from the nuclear spin system, and thus enhances the spin-lattice relaxation rate. Usually this enhancement speeds up the relaxation rate by orders of magnitude, so the T1 measurements serve as a very sensitive tool for detecting antiferromagnetic phase transitions. In our experiment, for B//ab, all the phase transitions at 2K in Fig 25 were verified by T1 measurements on the 137Ba(1) central transition, and the results are shown in Fig 71.

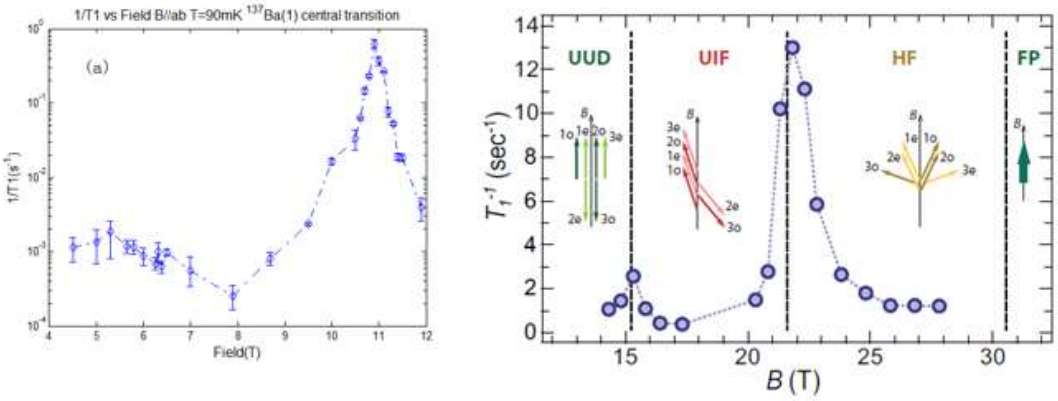

Figure 71 (a) Spin-lattice relaxation rate 1/T1 measured at 90mK, ^{137}Ba(1) central transition, the high frequency peak of the spectra. (b) Spin-latice relaxation rate 1/T1 measured at 2K, ^{137}Ba(1) central transition, the low frequency peak of the spectra.

From Fig 71(b), we can clearly see the two phase transitions signaled by the great enhancement of spin-lattice relaxation rate, and the phase boundaries defined by the maximum relaxation rate are consistent with the fields where the NMR spectra have some change. In Fig 71(a), the phase transition from low field Y phase to the uud phase is well defined by the enhancement peak in relaxation rate, and the transition field 10.8T agrees with the phase diagram plotted from thermodynamics measurement. However, we do not see evidence for the low field phase transition claimed by the heat capacity measurements. Going across the supposed transition field 6.5T, there is no abrupt change like the high field transitions. Considering that the NMR spectra and sublattice magnetization are exactly the same as the 1.6K measurements, we conclude that there might be no phase transition in the low field region, or at least the transition is not sensitive to NMR measurements.

The temperature dependence of spin-lattice relaxation rate is also interesting in the sense that it detects the activation energy of the electron spin system and serves as a tool to decide if the elementary excitation is gapped or not. In the low-temperature limit, the temperature dependence of relaxation rate conforms to the exponential decay:

$$\frac{1}{T_1} \propto e^{-\Delta/kT}$$

where Δ is the energy gap. When extrapolating to zero temperature, we should expect the relaxation rate falls to zero, which means there is no channel for energy exchange. This is easy to understand if we notice that the energy difference between nuclear spin energy levels is orders of magnitude smaller than the energy gap of the electron spin system, so at zero temperature, without the help of thermal fluctuation, energy exchange between the nuclear spin system and the lattice becomes impossible.

Experimentally, we measured T_1 at various fields in the uud phase, and the data are shown in Fig 72.

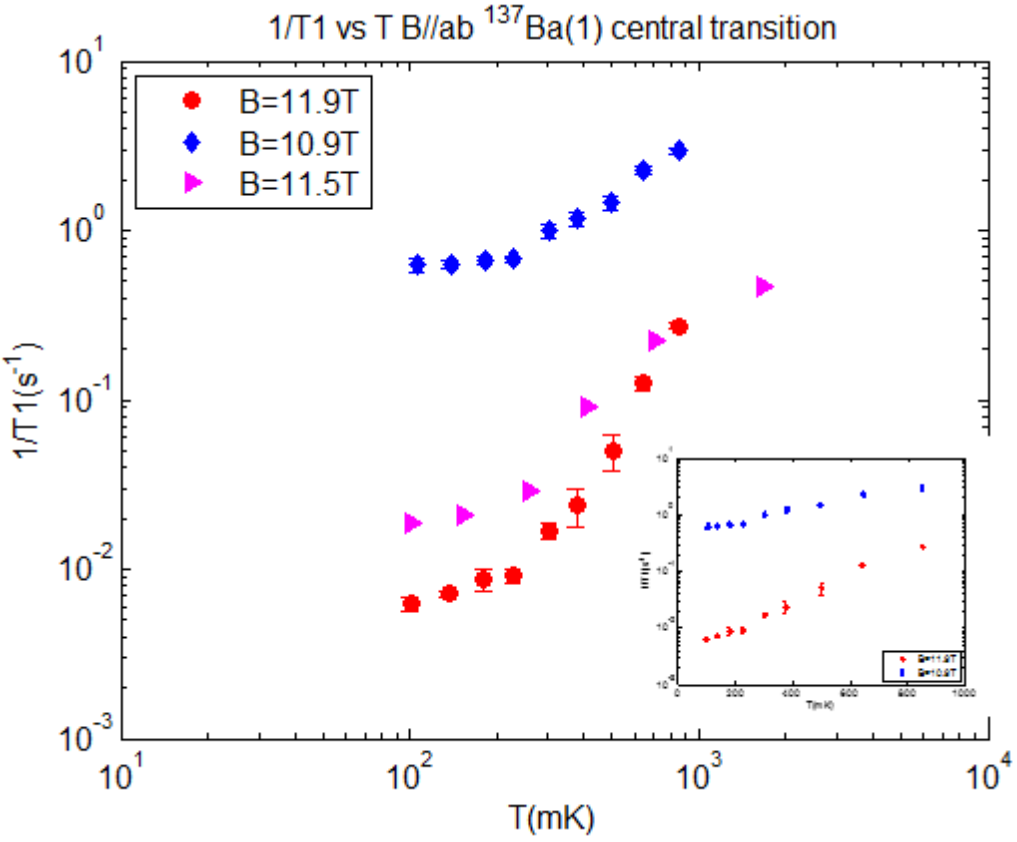

Figure 72 Temperature dependence of spin-lattice relaxation rate at various fields in the uud phase. The inset shows the same data with linear x-axis.

From the data, we actually see that the decreasing trend of the relaxation rate slows down at lower temperature, which is an obvious contradiction to the gapped excitation assumption. From the inset, we notice that the extrapolation of spin-lattice relaxation rate does not go to zero at zero temperature. There are two possibilities. First, the elementary excitation is not gapped, which would be a natural conclusion from the measurements results. However, this feature of relaxation rate may not be intrinsic to the system, and it may be the effect of impurities. The recovery line of T_1 measurement exhibits stretched exponential

feature, which indicates inhomogeneity of the sample, and the X-ray refraction detection shows that the quality of the sample we used is not very good. These facts blur the interpretation of temperature dependent T_1 measurements, so we can only conclude that the T_1 data do not support the gapped excitation, but the true nature of the excitation spectrum needs further research.

Conclusions and Open questions

For decades, the triangular lattice antiferromagnet (TLA) remains a hot topic in condensed matter physics. The theoretical work on the triangular system has results in hundreds of papers, and the most prominent prediction is that an isotropic TLA system may possess an up-up-down state signaled by a plateau in the magnetization. On the other hand, the experimental research is largely limited by the synthesis of high-quality sample, especially high quality single crystals. The successful synthesis of $Ba_3CoSb_2O_9$ single crystal is thus an important breakthrough in the study of TLA. This compound has an almost isotropic spin-1/2 triangular layer, with a relatively much weaker interplanar coupling, which makes it a good quasi-2D triangular lattice. More importantly, the saturation field of this compound is only around 30T, which enables experimentalists to study the whole phase diagram.

The preliminary work on $Ba_3CoSb_2O_9$ focused on the magnetization and thermodynamic properties [16] [17] [22]. The magnetic plateau has been discovered by the magnetization results [16], and the full H-T phase diagram has been plotted according to the heat capacity results. However, these measurements can only reveal the existence of phase transitions. The details of the magnetic ordering cannot be derived from those measurements. As a local probe, the nuclear

magnetic resonance detection is the best candidate to finish the job. In UCLA, we studied the low field phases, and in NHMFL, we explored the high field phase.

For B//ab, NMR spectra and relaxation rate prove the existence of 4 different phases, and the whole phase diagram is reproduced. The spin orientations of each phase are verified to be consistent with theoretical prediction. The phase boundaries set up by both spectra analysis and field dependence relaxation rate analysis agree with the results obtained from magnetization and thermodynamic measurements.

For B//c, the low field part of the phase diagram is reproduced. The high field phase is still an open question and need more input from both theory and experiment.

Another open question is brought up when we compare the ground state of two compounds with similar structures- the $Ba_3CoSb_2O_9$ we have discussed, and the $Ba_3NiSb_2O_9$ with the 6H-B structure. The $Ba_3NiSb_2O_9$ compound can crystalize in various structures, including the 6H-A, 6H-B, and 3C phases [36]. Among these phases, the 6H-A compound exhibits an antiferromagnetic transition from the heat capacity measurements, but the 6H-B and 3C compound show no sign of long-range magnetic ordering. The 6H-B structure of $Ba_3NiSb_2O_9$ is interesting for comparison with the $Ba_3CoSb_2O_9$ compound because they have very similar structure. Both have a highly symmetric hexagonal lattice with a triangular plane.

Two major differences between them are for the Ni compound, the electron spin is 1 on the triangular plane, and adjacent layers are not directly stacked on top of each other. Instead, in $Ba_3NiSb_2O_9$ with the 6H-B structure, adjacent layers are displaced in a way that the Ni ion in one layer projects exactly to the center of the triangle in the next layer (Fig 73).

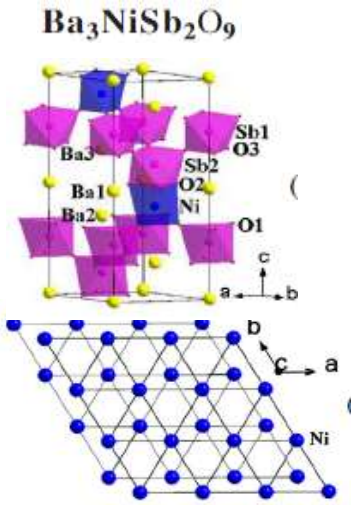

Figure 73 $Ba_3NiSb_2O_9$ with the 6H-B structure, adjacent layers are displaced in a way that the Ni ion in one layer projects exactly to the center of the triangle in the next layer. Ref [36].

The NMR spectra of both $Ba_3NiSb_2O_9$ and $Ba_3CoSb_2O_9$ are shown in Fig 74 for comparison. From the spectra, we can see that the $Ba_3CoSb_2O_9$ compound has narrow and well distinguished Ba NMR lines in the paramagnetic state, and we have shown in this thesis that ordered moments can be well defined at low temperature, signaling the existence of long-range magnetic order. On the other hand, the $Ba_3NiSb_2O_9$ at 2.7K has a very broad NMR spectrum, indicating highly inhomogeneous local environment and no ordered moments in the long range.

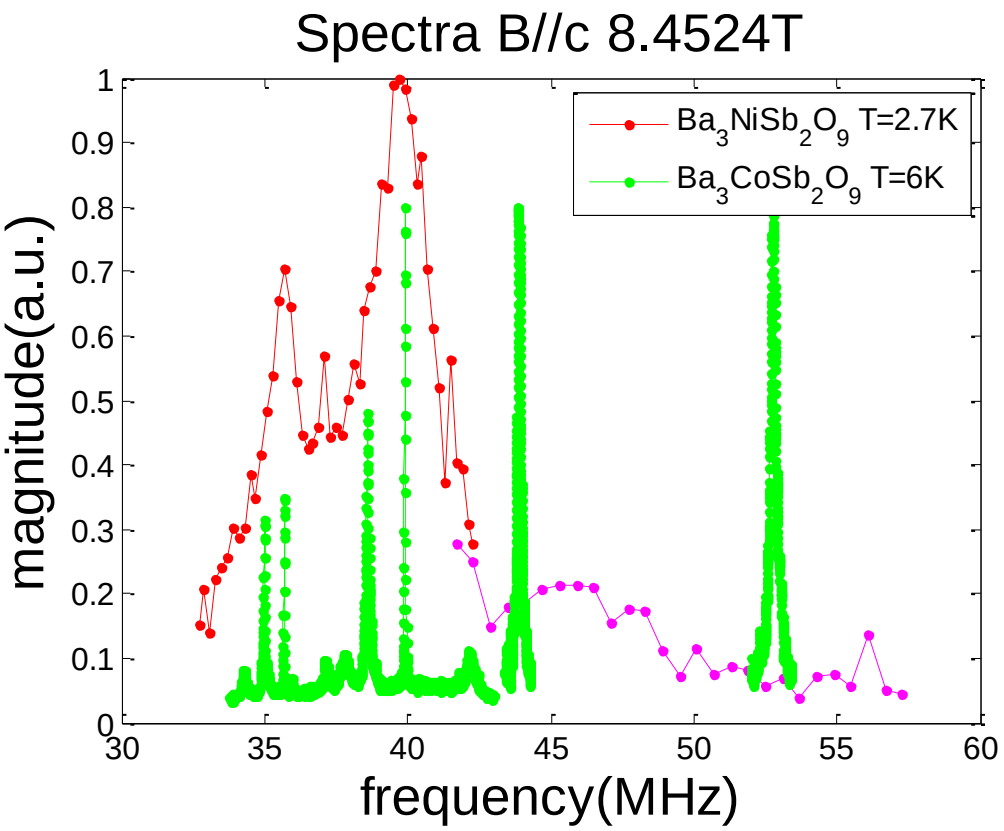

Figure 74 $Ba_3NiSb_2O_9$ spectrum (red) at 2.7K B//c, obtained by summing up the echo signal in the time domain. $Ba_3CoSb_2O_9$ spectrum (green) at 6K B//c for comparison, obtained by summing up the echo signal in the time domain.

As I mentioned in Chapter 3, there are many factors affecting the ground state of a triangular lattice compound, and the theoretical determination of the ground state phase diagram is far from sufficient in making predictions for specific materials. In the spirit of comparison study, compounds with similar crystal structure before different magnetic properties can provide useful information. We would expect more research, both experimentally and theoretically, to contribute to the Heisenberg antiferromagnetic model on triangular lattice.

Bibliography

[1] H. Bethe, Theorie der Metalle. Erster Teil. Eigenwerte und Eigenfunktionen der line ¨arenatomischen Kette, Z. Phys. 71 (1931), 205-226.

[2] L. Néel, Propriétées magnétiques des ferrites; Férrimagnétisme et antiferromagnétisme, Annales de Physique (Paris) 3, 137–198 (1948).

[3] G. Toulouse, Commun. Phys.2, 115 (1977) 115

[4] Vannimenus, J.; Toulouse, G. (1977). "Theory of the frustration effect. II. Ising spins on a square lattice". J. Phys. C 10 (18): L537

[5] G. H. Wannier, Phys. Rev. 79, 357 (1950).

[6] K. Husimi and I. Syˆozi, Prog. Theor. Phys. 5, 177 (1950).

[7] P. W. Anderson Mat. Res. Bull. Vol 8, pp. 153-160, (1973)

[8] D. A. Huse and V. Elser, Phys. Rev. Lett. 60, 2531 (1988).

[9] T. Jolicoeur and J. C. Le Guillou, Phys. Rev. B 40, 2727 (1989).

[10] 5L. Capriotti, A. E. Trumper, and S. Sorella, Phys. Rev. Lett. 82, 3899 (1999).

[11] Seabra, et al., PRB 84, 214418 (2011).

[12] H. Nishimori and S. Miyashita, J. Phys. Soc. Jpn 55, 4448 (1986).

[13] T. Ono, H. Tanaka, H. Aruga Katori, F. Ishikawa, H. Mitamura, and T. Goto, Phys. Rev. B 67, 104431 (2003).

[14] N. A. Fortune, S. T. Hannahs, Y. Yoshida, T. E. Sherline, T. Ono, H. Tanaka, and Y. Takano, Phys. Rev. Lett. 102, 257201 (2009).

[15] R. S. Gekht and I. N. Bondarenko, Zh. E ´ksp. Teor. Fiz. 111, 627–643 February 1997.

[16] Y. Shirata, H. Tanaka, A. Matsuo, and K. Kindo, Phys. Rev. Lett. 108, 057205 (2012).

[17] H. D. Zhou, C. Xu, A. M. Hallas, H. J. Silverstein, C. R. Wiebe, I. Umegaki, J. Q. Yan, T. P. Murphy, J.-H. Park, Y. Qiu, J. R. D. Copley, J. S. Gardner, and Y. Takano, Phys. Rev. Lett. 109, 267206 (2012).

[18] Yoshihiro Doi, Yukio Hinatsu and Kenji Ohoyama, J. Phys.: Condens. Matter 16 (2004) 8923–8935.

[19] M. E. Lines, The Journal of Chemical Physics 55, 2977 (1971).

[20] Hiroyuki SHIBA, Yoshifumi UEDA, Kouichi OKUNISHI, Shojiro KIMUR and Koichi KINDO, Journal of thePhysical Society of Japan, Vol. 72, No. 9, September, 2003, pp. 2326–2333

[21] A. V. Palii, B. S. Tsukerblat, E. Coronado, J. M. Clemente-Juan, and J. J. Borrs-Almenar, Inorganic Chemistry 42, 2455 (2003), http://pubs.acs.org/doi/pdf/10.1021/ic0259686.

[22] T. Susuki, N. Kurita, T. Tanaka, H. Nojiri, A. Matsuo, K. Kindo, and H. Tanaka, Phys. Rev. Lett. 110, 267201 (2013).

[23] J. Takano, H. Tsunetsugu, and M. E. Zhitomirsky, J. Phys.: Conf. Ser. 320, 012011 (2011).

[24] D. J. J. Farnell, R. Zinke, J. Schulenburg, and J. Richter, J. Phys. Condens. Matter 21, 406002 (2009).

[25] A. Honecker, J. Phys. Condens. Matter 11, 4697 (1999).

[26] H. Kawamura and S. Miyashita, J. Phys. Soc. Jpn. 54, 4530 (1985).

[27] Magnetic Phases of the Spin-1/2 Triangular-Lattice Antiferromagnet Ba3CoSb2O9, G. Koutroulakis, T. Zhou, C. D. Batista, Y. Kamiya, J. D. Thompson, S. E. Brown, and H. D. Zhou, arXiv:1308.6331 [cond-mat.str-el]

[28] C. Griset, S. Head, J. Alicea, and O. A. Starykh, Phys. Rev. B 84, 245108 (2011).

[29] A. V. Chubukov and D. I. Golosov, Journal of Physics: Condensed Matter 3, 69 (1991).

[30] T. Yildirim, A. B. Harris, and E. F. Shender, Phys. Rev. B 58, 3144 (1998).

[31] C. P. Slitchter, "Principles of magnetic Resonance", 3rd edition, Page 35, published by Springer.

[32] E. L. Hahn: Phys. Rev. 80, 580 (1950)

[33] I. Dzyaloshinskii, Journal of Physics and Chemistry of Solids 4, 241 (1958)

[34] T. Moriya, Physical Review 120, 91 (1960).

[35] N. Fortune, *et al*. APS 2013 March Meeting, B4.00007

[36] J.G.Cheng, *et al*, PRL **107**, 197204(2011)

[37] T. Ono, H. Tanaka, H. Aruga Katori, F. Ishikawa, H. Mitamura, and T. Goto, Phys. Rev. B 67, 104431 (2003).

[38] N. A. Fortune, S. T. Hannahs, Y. Yoshida, T. E. Sherline, T. Ono, H. Tanaka, and Y. Takano, Phys. Rev. Lett. 102, 257201 (2009).